

## LIGHT, ALPHA, AND FE-PEAK ELEMENT ABUNDANCES IN THE GALACTIC BULGE

CHRISTIAN I. JOHNSON<sup>1,2</sup>, R. MICHAEL RICH<sup>3</sup>, CHIAKI KOBAYASHI<sup>4</sup>, ANDREA KUNDER<sup>5</sup>, AND ANDREAS KOCH<sup>6</sup>

*Accepted for Publication in the Astronomical Journal: July 4, 2014*

### ABSTRACT

We present radial velocities and chemical abundances of O, Na, Mg, Al, Si, Ca, Cr, Fe, Co, Ni, and Cu for a sample of 156 red giant branch stars in two Galactic bulge fields centered near (l,b)=(+5.25,−3.02) and (0,−12). The (+5.25,−3.02) field also includes observations of the bulge globular cluster NGC 6553. The results are based on high resolution ( $R\sim 20,000$ ), high signal-to-noise ( $S/N\gtrsim 70$ ) FLAMES-GIRAFFE spectra obtained through the ESO archive. However, we only selected a subset of the original observations that included spectra with both high S/N and that did not show strong TiO absorption bands. The present work extends previous analyses of this data set beyond Fe and the  $\alpha$ -elements Mg, Si, Ca, and Ti. While we find reasonable agreement with past work, the data presented here indicate that the bulge may exhibit a different chemical composition than the local thick disk, especially at  $[Fe/H]\gtrsim -0.5$ . In particular, the bulge  $[\alpha/Fe]$  ratios may remain enhanced to a slightly higher  $[Fe/H]$  than the thick disk and the Fe-peak elements Co, Ni, and Cu appear enhanced compared to the disk. There is also some evidence that the  $[Na/Fe]$  (but not  $[Al/Fe]$ ) trends between the bulge and local disk may be different at low and high metallicity. We also find that the velocity dispersion decreases as a function of increasing  $[Fe/H]$  for both fields, and do not detect any significant cold, high velocity population. A comparison with chemical enrichment models indicates that a significant fraction of supernovae are required to explain the bulge abundance trends, and that initial mass functions that are steep, top-heavy (and do not include strong outflow), or truncated to avoid including contributions from stars  $>40 M_{\odot}$  are ruled out, in particular because of disagreement with the Fe-peak abundance data. For most elements, the NGC 6553 stars exhibit nearly identical abundance trends to comparable metallicity bulge field stars. However, the star-to-star scatter and mean  $[Na/Fe]$  ratios appear higher in the cluster, perhaps indicating additional self-enrichment.

*Subject headings:* stars: abundances, Galactic bulge: general, bulge: Galaxy: bulge, stars: Population

### II

#### 1. INTRODUCTION

Understanding the formation and subsequent evolution of the Galactic bulge is important both for interpreting observations of extragalactic populations and for constraining Galaxy chemodynamical formation models. Recent large sample spectroscopic surveys, such as the Bulge Radial Velocity Assay (BRAVA; Rich et al. 2007a; Howard et al. 2008; Howard et al. 2009; Kunder et al. 2012), the Abundances and Radial velocity Galactic Origins Survey (ARGOS; Freeman et al. 2013; Ness et al. 2012; 2013b), the Apache Point Observatory Galactic Evolution Experiment (APOGEE; Majewski et al. 2010; Nidever et al. 2012), and the GIRAFFE Inner Bulge Survey (GIBS; Zoccali et al. 2014) provide a coherent view of the bulge as a barred, triaxial system exhibiting cylindrical rotation. Photometric and star count studies have also discovered a double red clump along some

bulge sight lines that traces out an X-shaped structure (McWilliam & Zoccali 2010; Nataf et al. 2010; Saito et al. 2011). This structure appears to be dominated by stars with  $[Fe/H]>-0.5$  on bar-supporting orbits (Soto et al. 2007; Babusiaux et al. 2010; Ness et al. 2012; Uttenthaler et al. 2012; but see also Nataf et al. 2014).

Inclusive with these data are detailed composition analyses of field stars from moderate and high resolution spectroscopy (McWilliam & Rich 1994; Ramírez et al. 2000; Rich & Origlia 2005; Cunha & Smith 2006; Fulbright et al. 2006; Zoccali et al. 2006; Fulbright et al. 2007; Lecureur et al. 2007; Rich et al. 2007b; Cunha et al. 2008; Meléndez et al. 2008; Zoccali et al. 2008; Alves-Brito et al. 2010; Bensby et al. 2010a; Ryde et al. 2010; Bensby et al. 2011; Gonzalez et al. 2011; Hill et al. 2011; Johnson et al. 2011; Johnson et al. 2012; Rich et al. 2012; Uttenthaler et al. 2012; Barbuy et al. 2013; Bensby et al. 2013; García Pérez et al. 2013; Johnson et al. 2013a; Ness et al. 2013a; Jönsson et al. 2014) finding, at least in a general sense, that the bulge is composed of stars spanning more than a factor of 100 in  $[Fe/H]$ <sup>7</sup>, that bulge stars are uniformly enhanced in their  $[\alpha/Fe]$  ratios at low metallicity relative to the thin disk, and that the median  $[Fe/H]$  along bulge sight lines decreases as a function of increasing Galactic latitude (i.e., there is a metallicity gradient). The enhanced  $[\alpha/Fe]$  abundances, coupled with the low  $[La/Eu]$  ratios of bulge

<sup>1</sup> Harvard-Smithsonian Center for Astrophysics, 60 Garden Street, MS-15, Cambridge, MA 02138, USA; cjohnson@cfa.harvard.edu

<sup>2</sup> Clay Fellow

<sup>3</sup> Department of Physics and Astronomy, UCLA, 430 Portola Plaza, Box 951547, Los Angeles, CA 90095-1547, USA; rmr@astro.ucla.edu

<sup>4</sup> Centre for Astrophysics Research, University of Hertfordshire, Hatfield AL10 9AB, UK; c.kobayashi@herts.ac.uk

<sup>5</sup> Leibniz-Institute für Astrophysik Potsdam (AIP), Under Sternwarte 16, D-14482, Potsdam, Germany; akunder@aip.de

<sup>6</sup> Zentrum für Astronomie der Universität Heidelberg, Landessternwarte, Königstuhl 12, Heidelberg, Germany; akoch@lsw.uni-heidelberg.de

<sup>7</sup>  $[A/B]\equiv\log(N_A/N_B)_{\text{star}}-\log(N_A/N_B)_{\odot}$  and  $\log\epsilon(A)\equiv\log(N_A/N_H)+12.0$  for elements A and B.

stars (McWilliam et al. 2010; Johnson et al. 2012), are consistent with the notion that the bulge formed rapidly ( $\lesssim 1\text{--}3$  Gyr). In fact, the bulge appears uniformly old ( $\sim 10$  Gyr) in age studies based on color–magnitude diagram analyses (e.g., Ortolani et al. 1995; Zoccali et al. 2003; Clarkson et al. 2008; Valenti et al. 2013; but see also Ness et al. 2014), and Clarkson et al. (2011) estimate from the blue straggler population in an inner bulge field that a truly young ( $< 5$  Gyr) population should not constitute more than  $\sim 3.4\%$  of the bulge. In contrast, ages derived from microlensed dwarf studies (e.g., Bensby et al. 2013) find that while all metal–poor bulge stars are uniformly old,  $\sim 5\text{--}25\%$  of metal–rich stars, at least near the Galactic plane, may be only  $\sim 2\text{--}8$  Gyr in age.

While the observational data continue to grow, the difficult task of assembling the pieces into a fully self-consistent model of the bulge’s formation remains open. The chemodynamical bulge data are challenging to interpret. The bulge’s predominantly old age, enhanced  $[\alpha/\text{Fe}]$  ratios, vertical metallicity gradient, and the existence of possible “primordial building blocks” such as Terzan 5 (e.g., Ferraro et al. 2009; Origlia et al. 2011; 2013) are more consistent with the classical, merger built formation scenario. However, the bulge’s boxy X–shape, similar composition characteristics to at least the thick disk, and cylindrical rotation profile suggest that the bulge formed via secular evolution from a buckling disk instability and may be a “pseudobulge” (e.g., Kormendy & Kennicutt 2004; but see also Zoccali et al. 2014). While Shen et al. (2010) rule out a classical bulge component that exceeds  $\sim 8\%$  of the disk mass, it may still be possible for a bar to form within a pre-existing classical bulge (e.g., Saha et al. 2012). Additionally, evidence such as the metallicity gradient may not be unique to the classical bulge scenario, and may be consistent with a secular evolution model in which a radial metallicity gradient in the buckling disk is transformed into a vertical gradient in the resultant bar (Martinez–Valpuesta & Gerhard 2013). The bulge may also be composed of at least two stellar populations with different composition and kinematics (Babusiaux et al. 2010; Hill et al. 2011; Bensby et al. 2011; Bensby et al. 2013; Ness et al. 2013a). However, at the moment the exact nature of these potentially distinct stellar populations is far from certain.

Although most of the chemical abundance work mentioned previously has focused on the  $[\text{Fe}/\text{H}]$  and  $[\alpha/\text{Fe}]$  ratios in comparison with the thin and thick disks, the light odd–Z and Fe–peak (and also neutron–capture) elements also provide discriminatory power between models and other stellar populations (e.g., see Kobayashi et al. 2011; their Figure 14). The Fe–peak elements in particular are useful as they may be sensitive to formation environment and metallicity. For example, the metallicity dependent yields and increased contributions of massive stars are predicted to produce enhanced  $[\text{Cu}/\text{Fe}]$  and  $[\text{Zn}/\text{Fe}]$  ratios in the bulge compared to the local disk. Similarly, if the bulge formed with a significantly flatter initial mass function (IMF) than the disk then bulge stars should exhibit very large  $[\text{Co}/\text{Fe}]$  and  $[\text{Zn}/\text{Fe}]$  ratios (Nomoto et al. 2013). Therefore, here we measure abundances of the Fe–peak elements Cr, Fe, Co, Ni, and Cu, in addition to the light odd–Z and  $\alpha$ –elements O, Na, Mg, Al, Si, and Ca, in 156 red giant branch (RGB) stars

in two Galactic bulge fields at (l,b)=(+5.25,−3.02) and (0,−12), and compare the abundance ratios with other bulge fields, the Galactic disk, and chemical enrichment models.

## 2. OBSERVATIONS, TARGET SELECTION, AND DATA REDUCTION

The FLAMES–GIRAFFE spectra for this project are based on data obtained from the ESO Science Archive Facility under request number 51251, which are based on observations collected at the European Southern Observatory, Paranal, Chile (ESO Program 073.B–0074). Details regarding the selection of targets and input parameters (e.g., photometry and astrometry) are given in Zoccali et al. (2008). To briefly summarize, fibers were placed on K giants approximately 1–2 magnitudes brighter than the bulge red clump, and the spectra were obtained in high resolution mode ( $R \equiv \lambda/\Delta\lambda \sim 20,000$ ). The original program by Zoccali et al. (2008) included four fields centered at (l,b)=(+1.14,−4.18), (+0.21,−6.02), (0,−12), and (+5.25,−3.02). While the (+1.14,−4.18) and (+0.21,−6.02) fields were observed in the HR 13, HR 14, and HR 15 setups (spanning  $\sim 6100\text{--}6950$  Å), the (+5.25,−3.02) and (0,−12) fields were observed in the HR 11, HR 13, and HR 15 setups (5590–5835 Å; 6100–6400 Å; 6600–6950 Å). Since the HR 11 setup is the only one containing measurable copper lines, we have only analyzed GIRAFFE spectra from the (+5.25,−3.02) and (0,−12) fields. We note that the (+5.25,−3.02) field also includes the bulge globular cluster NGC 6553.

Figure 1 shows a 2MASS (Skrutskie et al. 2006) color–magnitude diagram of our final target selection from the archival data. The raw data set obtained from the ESO archive included observations of 205 RGB stars in the (+5.25,−3.02) field and 109 RGB stars in the (0,−12) field. However, we only analyzed spectra for which the co-added signal–to–noise (S/N) ratio exceeded  $\sim 70$ . We also discarded spectra that exhibited strong TiO absorption bands, for which a “standard” equivalent width (EW) analysis would be inappropriate. The final sample utilized here includes 75/205 stars (37%) in the (+5.25,−3.02) field and 81/109 stars (74%) in the (0,−12) field. In Figure 1 we also identify stars that are likely members of NGC 6553 (see Section 3.5). In particular, note the broad dispersion in the color–magnitude diagram of cluster members, as well as with stars within  $5'$  of the cluster center. This highlights the combined effects of differential reddening and population mixing along the line–of–sight toward the (+5.25,−3.02) field. The star names and coordinates from the raw image headers and Zoccali et al. (2008), as well as available 2MASS photometry and star identifiers, are provided in Table 1.

The raw science and calibration data were downloaded and re–reduced using the GIRAFFE Base–Line Data Reduction Software (girBLDRS)<sup>8</sup>. In particular, the pipeline software was used to carry–out bias subtraction and overscan trimming, dark correction, fiber identification, flat–fielding, wavelength calibration, scattered light correction, and spectrum extraction. Sky subtraction was carried out using the IRAF<sup>9</sup> *skysub* routine.

<sup>8</sup> The girBLDRS software can be downloaded at: <http://girbldrs.sourceforge.net/>.

<sup>9</sup> IRAF is distributed by the National Optical Astronomy Ob-

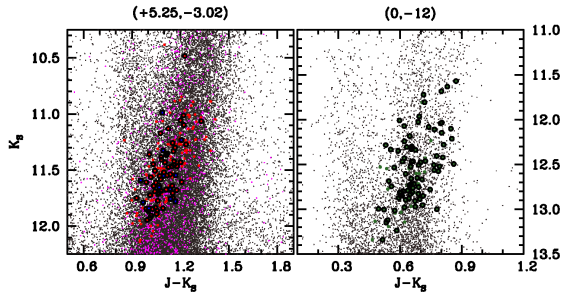


FIG. 1.— *left panel*: Color–magnitude diagram for the field centered near  $(l,b)=(+5.25,-3.02)$ . The filled red circles are all stars observed with the FLAMES instrument. The black outlined circles are those presented in this paper. The filled blue boxes indicate stars with radial velocities and metallicities consistent with belonging to the globular cluster NGC 6553. The small filled gray circles indicate all stars in the 2MASS catalog within  $30'$  of the central coordinates. Similarly, the small filled magenta circles indicate all stars in the 2MASS catalog within  $5'$  of NGC 6553. *right panel*: A similar plot but with the observed stars for the  $(l,b)=(0,-12)$  field shown in green.

Individual exposures were continuum normalized using a low order polynomial via the IRAF *continuum* routine, and the telluric band in the HR 13 spectra was removed using the IRAF task *telluric* and a set of FLAMES templates obtained during a different observing program with the same spectrograph setup. The individual spectra were shifted to a common velocity scale (i.e., the heliocentric velocity was removed) and co-added using IRAF’s *scombine* task.

### 3. DATA ANALYSIS

#### 3.1. Model Stellar Atmospheres

The four primary model atmosphere input parameters of effective temperature ( $T_{\text{eff}}$ ), surface gravity ( $\log(g)$ ), metallicity ( $[\text{Fe}/\text{H}]$ ), and microturbulence ( $vt$ ) were determined via spectroscopic analyses. For stars in the  $(0,-12)$  field, we used the model parameters given in Zoccali et al. (2008) as a starting point before converging to a solution. However, the adopted model atmosphere parameters for stars in the  $(+5.25,-3.02)$  field are not provided in Zoccali et al. (2008) nor Gonzalez et al. (2011). Therefore, we adopted the generic values  $T_{\text{eff}}=4500$  K,  $\log(g)=+2.0$  cgs,  $[\text{Fe}/\text{H}]=-0.20$  dex, and  $vt=1.5$  km s $^{-1}$  before converging to a solution. The final parameters given in Table 1 were derived by enforcing Fe I excitation equilibrium for  $T_{\text{eff}}$ , ionization equilibrium between Fe I/II<sup>10</sup> for  $\log(g)$ , and removing trends in Fe I abundance versus line strength for  $vt$ . The final models were interpolated within the available grid of AODFNEW ( $\alpha$ -enhanced) and ODFNEW (scaled-solar) ATLAS9 model atmospheres<sup>11</sup> (Castelli & Kurucz 2004). Stars with  $[\alpha/\text{Fe}]>+0.15$  were measured using the  $\alpha$ -enhanced models, and we used the scaled-solar models for stars with  $[\alpha/\text{Fe}]<+0.15$ . However, the issue of an  $\alpha$ -enhanced versus scaled-solar model should not introduce an error in the abundance ratios that exceeds the  $\sim 0.05$ -

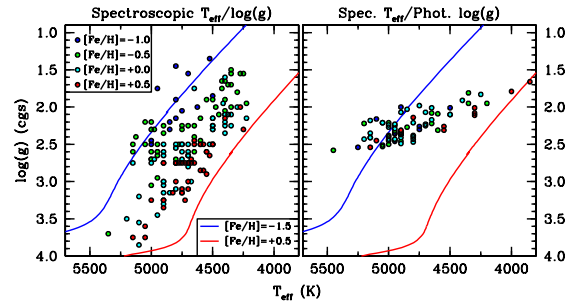


FIG. 2.— *left panel*: A plot of surface gravity versus effective temperature for all stars analyzed in this paper. The symbols are color-coded into rough metallicity bins. Metal-poor,  $\alpha$ -enhanced (blue) and metal-rich,  $\alpha$ -normal (red) 10 Gyr isochrone sequences (Dotter et al. 2008) are shown for guidance. *right panel*: The effective temperature (excitation equilibrium) and surface gravity (photometric) values employed by Zoccali et al. (2008) for the same stars presented here in the  $(0,-12)$  field. The literature model atmosphere parameters for stars in the  $(+5.25,-3.02)$  field are not available for comparison.

0.10 dex level (e.g., Fulbright et al. 2006; Alves-Brito et al. 2010; Johnson et al. 2013a).

Figure 2 shows our spectroscopically determined temperature and surface gravity values in comparison with the spectroscopic  $T_{\text{eff}}$  and photometric  $\log(g)$  values given in Zoccali et al. (2008). As is evident in Figure 2, the spectroscopic determination of both parameters leads to a more extended distribution of surface gravities. This is likely due to the unavoidable problem that one must assume a distance (and mass) when deriving a photometric surface gravity. However, this is only a major issue when determining abundances of elements from transitions that are strongly sensitive to  $\log(g)$ . The model atmosphere parameters determined here are well-bounded by and follow the expected trends of the 10 Gyr isochrones with  $[\text{Fe}/\text{H}]=-1.5$  ( $\alpha$ -enhanced) and  $[\text{Fe}/\text{H}]=+0.5$  ( $[\alpha/\text{Fe}]=0$ ) shown in Figure 2.

We do note that 25/156 (16%) stars in our sample converged to a solution in which  $\log(g)>3-3.5$ . The derived higher gravity values suggest some of these stars may be foreground lower RGB and subgiants rather than more evolved bulge RGB stars. A better measurement of surface gravity, either from the addition of more than 2–3 Fe II lines or the inclusion of more sensitive atmospheric pressure indicators, would better constrain the true nature of these stars. We do not find any strong systematic differences in the derived  $[\text{X}/\text{Fe}]$  ratios between stars of “low” and “high” gravity<sup>12</sup>, but it is unclear if the similar abundances should have any bearing when interpreting bulge versus thin/thick disk composition differences (see Section 4). However, the high gravity stars are also relatively metal-rich  $\langle[\text{Fe}/\text{H}]\rangle=+0.09$  ( $\sigma=0.25$ ), located preferentially on the blue half of the color–magnitude diagrams, and have a relatively small velocity dispersion ( $\sigma=55$  km s $^{-1}$  for  $\log(g)>3$ ). These data provide additional circumstantial evidence that the high gravity stars may be foreground, though possibly inner disk, contaminants (see also Zoccali et al. 2008; their Section 7).

In Figure 3 we compare the derived model atmosphere parameters between this study, Zoccali et al. (2008), and Gonzalez et al. (2011). We find good agreement

servatory, which is operated by the Association of Universities for Research in Astronomy, Inc., under cooperative agreement with the National Science Foundation.

<sup>10</sup> For stars in which Fe II lines were not measurable, we adopted the average  $T_{\text{eff}}/\log(g)$  combination for other stars of comparable  $T_{\text{eff}}$  and  $[\text{Fe}/\text{H}]$ .

<sup>11</sup> The model atmosphere grid can be accessed at: <http://wwwuser.oat.ts.astro.it/castelli/grids.html>.

<sup>12</sup> The  $[\text{Na}/\text{Fe}]$  ratios may be an exception as the high gravity stars tend to have lower  $[\text{Na}/\text{Fe}]$ , on average.

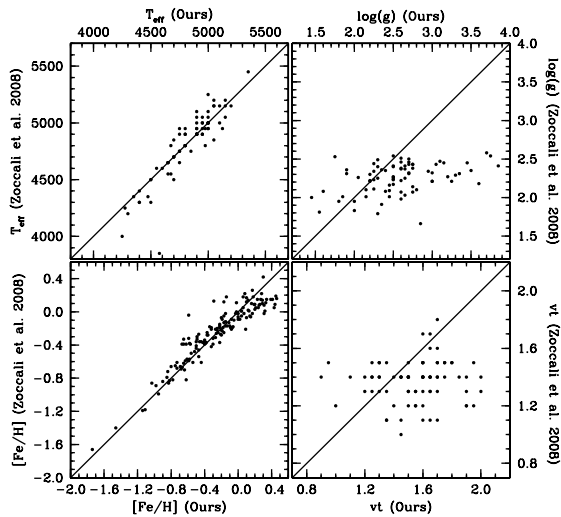


FIG. 3.— Derived model atmosphere parameters are compared between this work and Zoccali et al. (2008). Similar to Figure 2, the temperature, gravity, and microturbulence values are only available for the (0,–12) field in Zoccali et al. (2008). However, the metallicity panel compares our results to those in both the (0,–12) (Zoccali et al. 2008) and (+5.25,–3.02) (Gonzalez et al. 2011) fields. In all panels the solid black line indicates perfect agreement.

in the derived  $T_{\text{eff}}$  values with an average difference of only 2 K ( $\sigma=98$  K). The dispersion of  $\sim 100$  K is reasonable given the different line lists and model atmospheres (but similar technique of excitation equilibrium) used. As mentioned previously, there is some discrepancy in  $\log(g)$ , especially for the highest gravity stars, between the present work and Zoccali et al. (2008). For stars with  $\log(g) < +2.5$ , the average difference in  $\log(g)$  is 0.01 dex ( $\sigma=0.29$  dex), but for stars with  $\log(g) > +2.5$  the magnitude of the average gravity difference is 0.64 dex ( $\sigma=0.37$  dex). Comparing the microturbulence values, which may be particularly sensitive to line choice and can vary as a function of gravity, we find an average difference of 0.18  $\text{km s}^{-1}$  ( $\sigma=0.27$   $\text{km s}^{-1}$ ).

When comparing derived  $[\text{Fe}/\text{H}]$  values, we find good agreement for  $[\text{Fe}/\text{H}] < +0.2$  with an average difference of 0.03 dex ( $\sigma=0.13$  dex). However, as is evident in Figure 3 our derived  $[\text{Fe}/\text{H}]$  values are systematically higher on average by 0.18 dex ( $\sigma=0.13$  dex), for stars with  $[\text{Fe}/\text{H}] > +0.2$ . The source of this discrepancy may be related to the large  $1\sigma$   $[\text{Fe}/\text{H}]$  uncertainties given in Zoccali et al. (2008) for stars with  $[\text{Fe}/\text{H}] \gtrsim 0$ . This is illustrated in Figure 4 where we plot the  $1\sigma$   $[\text{Fe}/\text{H}]$  uncertainties between our work and Zoccali et al. (2008) as a function of  $[\text{Fe}/\text{H}]$ . Ideally one expects to have measurement errors that are not correlated with metallicity, as is the case here. For the Zoccali et al. (2008) subsample in common with the present analysis, the line-to-line dispersions are comparable only for stars with  $[\text{Fe}/\text{H}] \lesssim +0.2$ .

### 3.2. Equivalent Width Abundance Determinations

The abundances of Fe I, Fe II, Si I, Ca I, Cr I, and Ni I were determined by measuring EWs via an interactive, semi-automatic code developed for this project. The measurement process followed the “standard” procedure of fitting single or multiple Gaussian profiles to the spectra for isolated and weakly blended lines, respectively. However, the measurement time frame was significantly reduced by implementing a simple machine

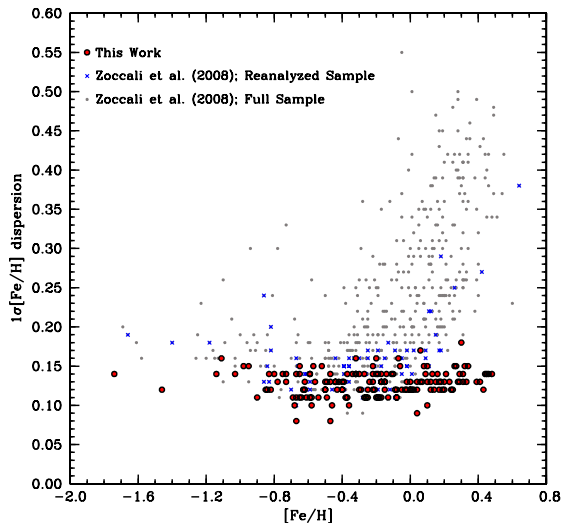


FIG. 4.— The  $1\sigma$  line-to-line dispersion values for  $[\text{Fe}/\text{H}]$  measurements in this work (filled red circles), the original Zoccali et al. (2008) stars selected for reanalysis (blue crosses), and the full Zoccali et al. (2008) sample that includes all four fields (filled gray circles).

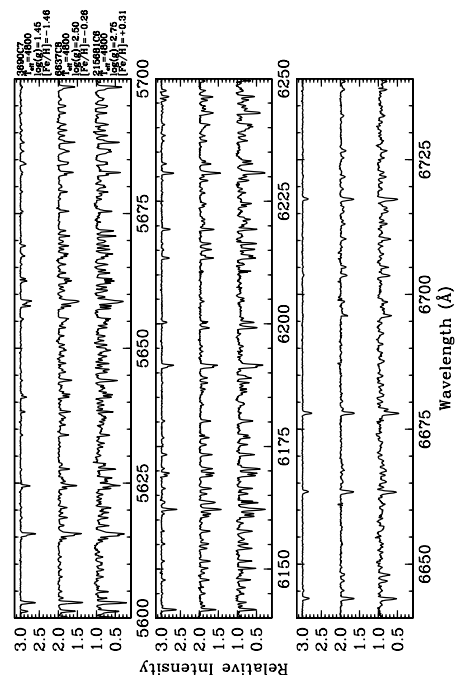


FIG. 5.— Sample spectra are shown to illustrate both data quality and the change in line strengths and continuum availability for stars of similar temperature but varying metallicity.

learning algorithm that kept track of user input on a per-line basis to make an educated first guess for subsequent measurements in other stars of: the number of profiles to fit, profile fitting edges, and the central wavelength, width, and central depth of all associated nearby features. While all EW measurements were manually inspected, as was mentioned in Section 2 we selected stars from the archival data based primarily on S/N considerations in an effort to reduce measurement uncertainties. Sample spectra for stars of similar temperature but different metallicity are shown in Figure 5 to illustrate typical data quality in the three spectrograph setups.

The line lists for this project were created by visually examining the high S/N spectra of cool metal-poor and metal-rich giants in the sample, finding all isolated and/or weakly blended features for elements of interest, and merging the two line list sets. This was done to ensure that a roughly equivalent number of lines could be used in metal-rich and metal-poor stars, and the manual inspection of each fit enabled us to discard prohibitively strong and weak lines. On average, the Fe I, Fe II, Si I, Ca I, Cr I, and Ni I abundances were based on the measurement of 70, 2, 8, 6, 6, and 16 lines, respectively. The  $\log(gf)$  values were set via an inverse abundance analysis relative to Arcturus. We adopted the Arcturus model atmosphere parameters from Fulbright et al. (2006). Similarly, for Fe, Si, and Ca we adopted the Arcturus abundances from Fulbright et al. (2006), and for Cr and Ni we adopted the Arcturus abundances from Ramírez & Allende Prieto (2011). The final line list, including the adopted Arcturus and derived solar abundances (based on measurements of the Hinkle et al. 2000 Arcturus and solar atlases), are provided in Table 2. The derived solar abundances for Fe, Si, Ca, and Cr agree within  $\sim 0.05$  dex of the values given in Asplund et al. (2009).

The final abundances of Fe I, Fe II, Si I, Ca I, Cr I, and Ni I, determined using the *abfind* driver of the LTE line analysis code MOOG (Snedden 1973; 2010 version), are given in Table 3. Note also that the  $[\text{Fe}/\text{H}]$  values given in Table 1 are the average of the  $[\text{Fe I}/\text{H}]$  and  $[\text{Fe II}/\text{H}]$  abundances given in Table 3. However, the average difference in the sense  $[\text{Fe I}/\text{H}] - [\text{Fe II}/\text{H}]$  is  $+0.00$  dex with a small dispersion ( $\sigma=0.02$  dex).

### 3.3. Spectrum Synthesis Abundance Determinations

For the element abundances derived from transitions involving a small number of lines that are affected by significant blends from prevalent spectral features, such as molecules and Ca I autoionization, and/or broadened due to isotopes and/or hyperfine structure, we used spectrum synthesis rather than EW analyses. For the present work this list includes  $[\text{O I}]$ , Na I, Mg I, Al I, Co I, and Cu I. The abundances were determined using the parallelized version of the *synth* driver for MOOG (Johnson et al. 2012). For O, Na, Mg, and Al, we adopted as a reference point the Arcturus abundances given in Fulbright et al. (2006). However, as described below the reference Arcturus abundances for Co and Cu are based on measurements using the Kurucz (1994) and Cunha et al. (2002) hyperfine structure line lists.

The specific reasons for using synthesis are slightly different for each element given above. The  $6300.30 \text{ \AA}$   $[\text{O I}]$  line is blended with both a Sc II feature at  $6300.69 \text{ \AA}$  and a Ni I feature at  $6300.33 \text{ \AA}$ . Additionally, for most stars in this sample the oxygen abundance is sensitive to the molecular equilibrium calculations set by the carbon and nitrogen abundances as well. Using the CN line list from the Kurucz (1994) database, we iteratively solved for the O and C+N abundances in each star. For sodium, the  $6154.23 \text{ \AA}$  Na I line is relatively clean, but the  $6160.75 \text{ \AA}$  Na I line is partially blended with two relatively strong Ca I lines. The three Mg I lines at  $6319 \text{ \AA}$  are strongly affected by a broad Ca I autoionization feature, which we set by fitting the slope of the pseudo-continuum from  $\sim 6316$ – $6318 \text{ \AA}$ . The  $6696.02$  and  $6698.67 \text{ \AA}$  Al I lines are both

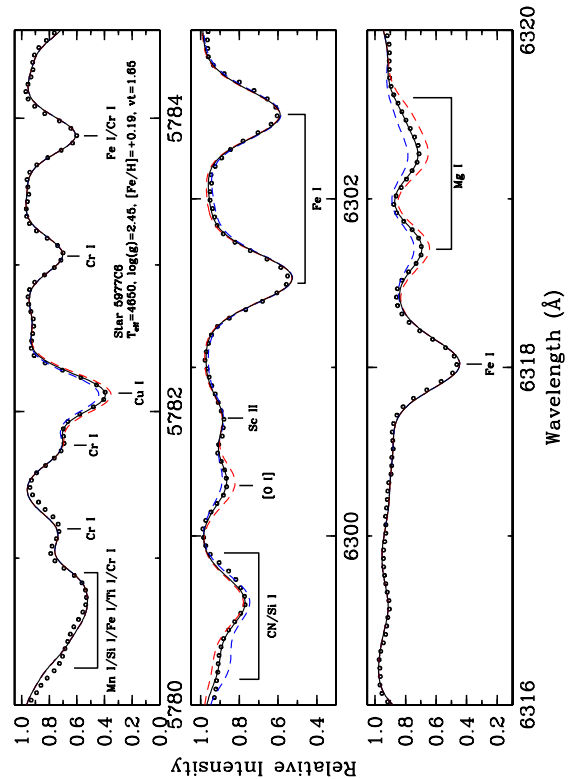


FIG. 6.— Sample spectrum synthesis fits are shown for the Cu I,  $[\text{O I}]$ , and Mg I features. In all panels the solid black line indicates the best-fit value. The dashed red and blue lines indicate changes to the best-fit abundance by  $\pm 0.3$  dex, respectively.

affected by CN, particularly in cooler and more metal-rich stars. Therefore, as with  $[\text{O I}]$  we simultaneously fit the Al I doublet and nearby CN features. The odd- $Z$  isotope  $^{59}\text{Co}$  constitutes almost 100% of the cobalt abundance. While the  $5647.23$  and  $6117.00 \text{ \AA}$  Co I lines are relatively weak ( $\text{EW} \lesssim 50 \text{ m\AA}$ ), we included the hyperfine structure components from the Kurucz (1994) line list in our syntheses. For copper, which is dominated by the two odd- $Z$  isotopes  $^{63}\text{Cu}$  and  $^{65}\text{Cu}$ , we assumed a solar system mixture of 69.17% and 30.83%, respectively. We adopted the hyperfine line list of Cunha et al. (2002) and derive a similar solar abundance of  $\log \epsilon(\text{Cu})=+4.04$  but a slightly lower Arcturus abundance than McWilliam et al. (2013). Although the  $5782.11 \text{ \AA}$  Cu I line is strong in most of our stars, the hyperfine broadening helps desaturate the line profile to some extent.

In Figure 6 we show sample syntheses of the O, Mg, and Cu features for a typical metal-rich spectrum. We note that the  $5782 \text{ \AA}$  Cu I line is also sometimes affected by a nearby diffuse interstellar band (DIB). The width and depth of the DIB feature was found to be highly variable. The level of contamination depends on the relative velocity between the interstellar cloud and the individual star and also the reddening value. Therefore, stars in the  $(+5.25, -3.02)$  field, which have an average  $E(B-V)=0.7$ , were more strongly affected than those in the  $(0, -12)$  field, which have an average  $E(B-V)=0.2$  (Zoccali et al. 2008). Most of the stars listed in Table 3 that do not have a  $[\text{Cu}/\text{Fe}]$  abundance listed were omitted because of obvious contamination by the DIB feature.

### 3.4. Radial Velocities

Radial velocities were measured using the XCSAO code (Kurtz & Mink 1998) for each individual exposure of every star and in all three filters. For reference templates we generated synthetic spectra ranging in temperature from 4250 to 5000 K (250 K steps),  $\log(g)$  from +0.5 to +3.5 cgs (0.5 dex steps),  $[\text{Fe}/\text{H}]$  from  $-1.5$  to  $+0.5$  dex (0.5 dex steps), and  $v_t$  from 1 to 2  $\text{km s}^{-1}$  (0.25  $\text{km s}^{-1}$  steps). Radial velocities were determined relative to the nearest template. We found the average agreement between exposures to be  $0.15 \text{ km s}^{-1}$  ( $\sigma=0.13 \text{ km s}^{-1}$ ). The heliocentric corrections were taken from the headers of the pipeline reduced files, and the heliocentric radial velocities ( $RV_{\text{helio.}}$ ) listed in Table 1 represent the average value of all exposures and filters for each star.

The kinematic properties of the bulge have been extensively discussed in dedicated survey papers (e.g., Rich et al. 2007a; Howard et al. 2009; Rangwala et al. 2009a; Babusiaux et al. 2010; Kunder et al. 2012; Ness et al. 2013b; Nidever et al. 2012; Babusiaux et al. 2014; Zoccali et al. 2014). Therefore, here we seek only to place our results in context with those surveys. Figure 7 shows velocity histograms for both fields, the velocity distribution as a function of  $[\text{Fe}/\text{H}]$ , and the velocity dispersion as a function of  $[\text{Fe}/\text{H}]$ . While a detailed comparison between our measured velocities and those in Babusiaux et al. (2010) is not possible because their individual velocities were not published, for both fields we can compare our average results with those given in Figure 13 of Zoccali et al. (2008) and Table 3 of Babusiaux et al. (2010). For the  $(+5.25, -3.02)$  field, ignoring NGC 6553 stars, we find average velocity and dispersion values of  $+4.55 \text{ km s}^{-1}$  and  $95.51 \text{ km s}^{-1}$ , respectively. This compares well with the Zoccali et al. (2008) average velocity of  $+11 \text{ km s}^{-1}$  and velocity dispersion of  $107 \text{ km s}^{-1}$ . Similarly, in the  $(0, -12)$  field we measured an average heliocentric radial velocity of  $-8.61 \text{ km s}^{-1}$  ( $\sigma=85.56 \text{ km s}^{-1}$ ) compared to the Babusiaux et al. (2010) values of  $-14 \text{ km s}^{-1}$  ( $\sigma=80 \text{ km s}^{-1}$ ). Additionally, as can be seen in Figure 8 our galactocentric radial velocity ( $V_{\text{GC}}$ ) distributions are similar to those of nearby fields from the BRAVA, GIBS, and APOGEE surveys.

With the exception of the stars obviously related to NGC 6553, we find in agreement with previous bulge studies that, at least away from the Galactic plane, the velocity distributions are normal with no evidence for significant cold populations (but see also Rangwala et al. 2009b). This contrasts with Nidever et al. (2012) and Babusiaux et al. (2014), which find kinematically cold populations with  $V_{\text{GC}} \sim +200 \text{ km s}^{-1}$ . However, their fields are significantly closer to the Galactic plane than those analyzed here. We do note however that these high velocity populations are also not found in the BRAVA, ARGOS, nor GIBS analyses, nor is there yet a satisfactory theoretical explanation for their origin (e.g., Li et al. 2014).

For the  $(0, -12)$  field we observe the same trend of a decrease in velocity dispersion with increasing  $[\text{Fe}/\text{H}]$  found by Babusiaux et al. (2010). However, while Babusiaux et al. (2010) find an increase in velocity dispersion with increasing  $[\text{Fe}/\text{H}]$  in the  $(+1.1, -4)$  field of Baade’s window, our off-axis but similar Galactic latitude field at  $(+5.25, -3.02)$  still exhibits a trend of decreasing velocity dispersion with increasing  $[\text{Fe}/\text{H}]$ . This further contrasts

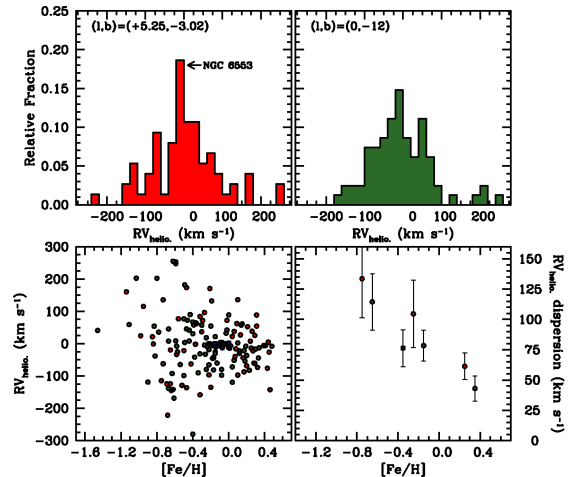


FIG. 7.— *top left*: The red histogram ( $20 \text{ km s}^{-1}$  bins) illustrates the heliocentric radial velocity distribution function for the  $(+5.25, -3.02)$  field. The bulge globular cluster NGC 6553 is labeled. *top right*: The green histogram ( $20 \text{ km s}^{-1}$  bins) illustrates the heliocentric radial velocity distribution function for the  $(0, -12)$  field. *bottom left*: Heliocentric radial velocity is plotted as a function of  $[\text{Fe}/\text{H}]$  for the  $(+5.25, -3.02)$  and  $(0, -12)$  stars, which are shown as filled red and filled green circles, respectively. The NGC 6553 stars (filled blue boxes) are particularly evident in this panel. *bottom right*: The heliocentric radial velocity dispersion is plotted as a function of (binned)  $[\text{Fe}/\text{H}]$ , using the same color scheme as the other panels. For the middle  $[\text{Fe}/\text{H}]$  bin the blue box and red circle indicate the velocity dispersion with (blue) and without (red) the NGC 6553 stars included.

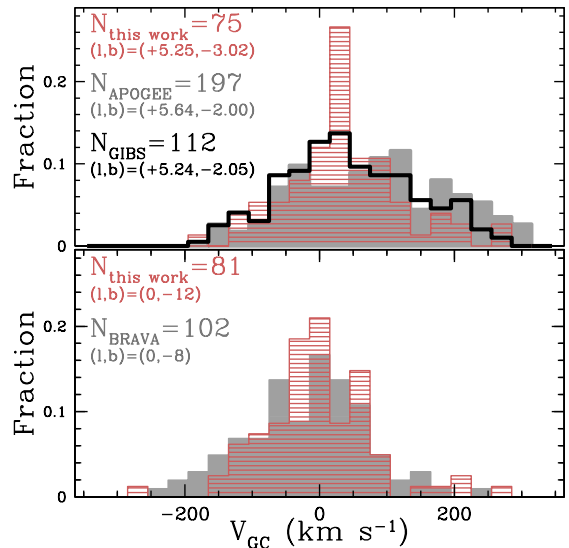


FIG. 8.— *top*: The striped red, solid gray, and black lined histograms compare the galactocentric radial velocity distributions between the  $(+5.25, -3.02)$  field analyzed here and nearby fields observed as part of APOGEE and GIBS, respectively. The narrow peak near the center of the distribution is due to NGC 6553. *bottom*: The striped red and gray histograms compare the galactocentric radial velocity distributions between the  $(0, -12)$  field analyzed here and the relatively nearby  $(0, -8)$  field from the BRAVA survey.

with recent fields observed close to the plane by Babusiaux et al. (2014; see their Figure 16) that also show a possible increase in velocity dispersion with increasing  $[\text{Fe}/\text{H}]$ .<sup>13</sup> Our result is more similar to studies of outer bulge fields that find a consistent decrease in velocity dis-

<sup>13</sup> However, when taking into account the error bars in velocity dispersion for the points in Figure 16 of Babusiaux et al. 2014,

person with increasing  $[\text{Fe}/\text{H}]$  (e.g., Johnson et al. 2011; Uttenthaler et al. 2012; Johnson et al. 2013; Ness et al. 2013b). There is weak evidence in Figure 7 that the trend in velocity dispersion and  $[\text{Fe}/\text{H}]$  may be more shallow for the (+5.25,−3.02) field compared to the (0,−12) field. Note that the inclusion (or not) of NGC 6553 stars significantly affects the velocity dispersion of the  $[\text{Fe}/\text{H}]$  bin in which the cluster resides.

### 3.5. Identifying NGC 6553 Members

Members of the globular cluster NGC 6553 in the (+5.25,−3.02) field are best identified in the velocity–metallicity diagram in Figure 7. The likely members (12 stars total) are clustered near  $[\text{Fe}/\text{H}]\approx-0.10$  and  $RV_{\text{helio.}}\approx 0$  km s<sup>−1</sup>. Literature measurements of the cluster’s average  $[\text{Fe}/\text{H}]$  value vary considerably, with estimates that include: −0.55 (Barbuy et al. 1999), −0.16 (Cohen et al. 1999), −0.7 (Coelho et al. 2001), −0.3 (Origlia et al. 2002), −0.2 (Meléndez et al. 2003), and −0.2 (Alves–Brito et al. 2006). However, we find in agreement with the most recent estimates that  $\langle[\text{Fe}/\text{H}]\rangle=-0.11$  ( $\sigma=0.07$ ). While the cluster is slightly iron–deficient relative to the Sun, the moderate enhancements of the cluster’s  $[\alpha/\text{Fe}]$  ratio (see Section 4.1) gives it an overall metallicity that is roughly solar. NGC 6553 is therefore one of the most metal–rich globular clusters in the Galaxy.

We find similar agreement with literature values for the cluster’s radial velocity, with  $\langle RV_{\text{helio.}}\rangle=-2.03$  km s<sup>−1</sup> ( $\sigma=4.85$  km s<sup>−1</sup>). This is compared with recent values of: −1 km s<sup>−1</sup> (Coelho et al. 2001), +1.6 km s<sup>−1</sup> (Meléndez et al. 2003), and −1.86 km s<sup>−1</sup> (Alves–Brito et al. 2006). Finally, we note that the stars identified in Table 1 as possible cluster members have an average, projected radial distance from the cluster center of about 6′ ( $\sigma=5'$ ). We have adopted a more lenient radial distance discriminator than the 2′ limit used by Zoccali et al. (2008) and Gonzalez et al. (2011), and instead rely more on the  $[\text{Fe}/\text{H}]$  and velocity measurements to identify possible cluster members.

### 3.6. Abundance Ratio Comparisons with Previous Work

As noted previously, Zoccali et al. (2008) and Gonzalez et al. (2011) presented  $[\text{Fe}/\text{H}]$ ,  $[\text{Si}/\text{Fe}]$ ,  $[\text{Ca}/\text{Fe}]$ , and  $[\text{Ti}/\text{Fe}]$  abundances based on the same GIRAFFE data utilized here. Therefore, in Figures 9–10 we compare our results with theirs for stars and elements in common. While a quantitative comparison of the individual  $[\text{Fe}/\text{H}]$  values is given in Section 3.1 (see also Figure 3), in Figure 9 we compare the general shapes and bulk properties of the metallicity distribution functions. For the (+5.25,−3.02) field the average and median  $[\text{Fe}/\text{H}]$  ratios are similar, but the distribution from the present work is somewhat broader and extends to higher  $[\text{Fe}/\text{H}]$ . In contrast, there are no significant differences in the  $[\text{Fe}/\text{H}]$  distribution functions between the present work and the same stars from Zoccali et al. (2008), for the (0,−12) field. We also reconfirm one of the primary conclusions of Zoccali et al. (2008) that interior bulge fields have a higher average metallicity than outer bulge fields. Finally, we note that the distribution functions shown in

their trend is mostly flat.

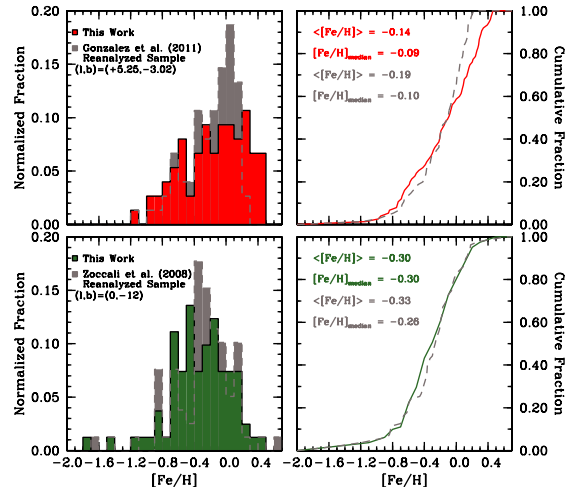


FIG. 9.— *top left*: The red and gray histograms (0.1 dex bins) illustrate the derived metallicity distribution functions for the (+5.25,−3.02) field in this work and Gonzalez et al. (2011), respectively. *top right*: The solid red and dashed gray lines illustrate the cumulative distribution functions for this work and Gonzalez et al. (2011), respectively. *bottom left*: The green and gray histograms (0.1 dex bins) illustrate the derived metallicity distribution functions for the (0,−12) field in this work and Zoccali et al. (2008), respectively. *bottom right*: The solid green and dashed gray lines illustrate the cumulative distribution functions for this work and Zoccali et al. (2008), respectively.

Figure 9 do not provide strong evidence supporting the existence of multiple, discreet populations, as has been suggested in some studies (Bensby et al. 2011; Hill et al. 2011; Bensby et al. 2013; Ness et al. 2013a). However, the number of stars per field presented here is  $<100$ .

In Figure 10 we compare our derived  $[\text{Mg}/\text{Fe}]$ ,  $[\text{Si}/\text{Fe}]$ , and  $[\text{Ca}/\text{Fe}]$  ratios to those given in Gonzalez et al. (2011). The average differences between the present work and that of Gonzalez et al. (2011) are  $\Delta[\text{Mg}/\text{Fe}]=+0.00$  ( $\sigma=0.14$ ),  $\Delta[\text{Si}/\text{Fe}]=+0.00$  ( $\sigma=0.13$ ), and  $\Delta[\text{Ca}/\text{Fe}]=-0.06$  ( $\sigma=0.14$ ). The relatively consistent star–to–star scatter of  $\sim 0.14$  dex is a reasonable estimate of the attainable precision between the two studies, which derive  $\alpha$ –element abundances from different techniques (synthesis in Gonzalez et al. 2011 and EW measurements here). We note that the  $\alpha$ –elements oxygen (measured here) and titanium (measured in Gonzalez et al. 2011) were not both measured in each study.<sup>14</sup>

### 3.7. Abundance Uncertainty Estimates

We investigated the sensitivity of derived abundances for each element in every star by taking the abundances given in Table 3, determining theoretical EWs using the line list in Table 2, and then varying the model atmosphere parameters  $T_{\text{eff}}$ ,  $\log(g)$ ,  $[\text{Fe}/\text{H}]$ , and  $v_t$  individually while holding the other parameters fixed. We selected parameter changes of 100 K in  $T_{\text{eff}}$ , 0.30 dex in  $\log(g)$ , 0.15 dex in  $[\text{M}/\text{H}]$ , and 0.30 km s<sup>−1</sup> in  $v_t$ , which are reasonable when comparing our derived parameters with those of the independent analysis by Zoccali et al. (2008; see also Section 3.1). The total uncertainty for

<sup>14</sup> Gonzalez et al. (2011) did not derive an oxygen abundance from the 6300 Å [O I] feature because of concerns regarding measurement accuracy. We chose not to include Ti abundances because of discrepant nucleosynthesis predictions for this element in comparison to observations (e.g., see Kobayashi et al. 2011; their Figure 14).

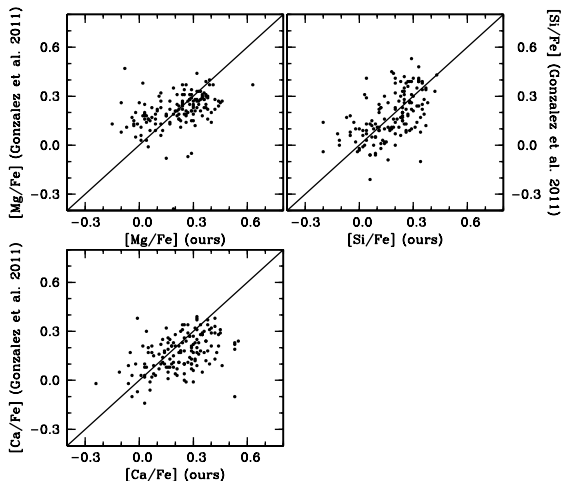


FIG. 10.— A comparison between the  $[\text{Mg}/\text{Fe}]$ ,  $[\text{Si}/\text{Fe}]$ , and  $[\text{Ca}/\text{Fe}]$  abundances derived here and in Gonzalez et al. (2011). The solid black line in each panel indicates perfect agreement.

each element ratio in each star resulting from this exercise is provided in Table 4.

In general, most elements are not affected by changes in  $T_{\text{eff}}$  of 100 K at more than the 0.1 dex level. However, the two species presented here that reside in their dominant ionization states ( $[\text{O I}]$  and  $[\text{Fe II}]$ ) are strongly affected by changes in surface gravity. For a change in  $\log(g)$  of 0.3 dex, the  $\log \epsilon(\text{O})$  and  $\log \epsilon(\text{Fe II})$  abundances can change by  $\sim 0.1$ – $0.3$  dex, but these effects are mitigated when the  $[\text{O I}/\text{H}]$  abundance is normalized with  $[\text{Fe II}/\text{H}]$ . These two species are also more strongly affected by changes in the model metallicity, and the larger  $[\text{Fe II}/\text{H}]$  measurement and sensitivity uncertainties are a contributing factor to the increased dispersion in the  $[\text{O}/\text{Fe}]$  ratios compared to other  $\alpha$ -elements (e.g.,  $[\text{Mg}/\text{Fe}]$ ). As expected, microturbulence sensitivity is correlated with a star’s overall metallicity (i.e., line strength). Among the transitions under consideration here, in metal-rich stars those of Na, Ca, and Cu typically have the strongest lines and are thus more strongly affected by the microturbulence uncertainty.

In Table 5 we also provide the  $1\sigma$  line-to-line dispersion values for all species measured here. These values should be mostly representative of the combined measurement error that includes effects such as: continuum placement, line deblending, synthesis fits via visual inspection,  $\log(gf)$  uncertainties, and model atmosphere deficiencies. Typical line-to-line dispersion values are  $\sim 0.08$  dex. The measurement error of Cu may be underestimated because of the line’s large EW, non-negligible blending (see Figure 6), and possible contamination with a nearby DIBS feature. A more reasonable measurement uncertainty for Cu is, in most cases,  $\sim 0.15$ – $0.20$  dex.

#### 4. RESULTS AND DISCUSSION

##### 4.1. The $\alpha$ Elements Oxygen, Magnesium, Silicon, and Calcium

The  $\alpha$ -elements have been the primary focus of detailed composition work in the Galactic bulge. To first order there is agreement among the various studies that: (1) the  $[\alpha/\text{Fe}]$  ratios are enhanced by  $\sim +0.3$  dex at  $[\text{Fe}/\text{H}] \lesssim -0.3$ , (2) for stars with  $[\text{Fe}/\text{H}] \gtrsim +0.3$  there is a mostly monotonic decline in  $[\alpha/\text{Fe}]$  with increasing

$[\text{Fe}/\text{H}]$ , (3) the bulge and thick disk may share similar chemistry over a wide range in metallicity, and (4) there are no significant variations in the  $[\alpha/\text{Fe}]$  trends between different bulge sight lines (McWilliam & Rich 1994; Cunha & Smith 2006; Zoccali et al. 2006; Fulbright et al. 2007; Lecureur et al. 2007; Meléndez et al. 2008; Alves-Brito et al. 2010; Bensby et al. 2010a; Ryde et al. 2010; Bensby et al. 2011; Gonzalez et al. 2011; Hill et al. 2011; Johnson et al. 2011; Uttenthaler et al. 2012; Bensby et al. 2013; García Pérez et al. et al. 2013; Johnson et al. 2013; Ness et al. 2013a; Jönsson et al. 2014). Additionally, there is evidence that the  $[\text{O}/\text{Mg}]$  ratio declines with increasing metallicity (Fulbright et al. 2007; Lecureur et al. 2007; McWilliam et al. 2008; Alves-Brito et al. 2010).

The new data presented here, and summarized in Figure 11, reinforce many observations from the previous studies mentioned above. In particular, we find that for  $[\text{Fe}/\text{H}] < -0.3$  all of the  $[\alpha/\text{Fe}]$  ratios are enhanced and exhibit minimal star-to-star scatter with  $\langle [\text{O}/\text{Fe}] \rangle = +0.54$  ( $\sigma = 0.10$ ),  $\langle [\text{Mg}/\text{Fe}] \rangle = +0.33$  ( $\sigma = 0.08$ ),  $\langle [\text{Si}/\text{Fe}] \rangle = +0.28$  ( $\sigma = 0.07$ ), and  $\langle [\text{Ca}/\text{Fe}] \rangle = +0.34$  ( $\sigma = 0.09$ ). For stars with  $[\text{Fe}/\text{H}] > -0.3$ , we find that the  $[\alpha/\text{Fe}]$  ratios decrease with increasing  $[\text{Fe}/\text{H}]$ . However, Figure 11 illustrates the disparate trends for individual elements and highlights the information loss that can occur when averaging abundance ratios for multiple  $\alpha$ -elements. The  $[\text{O}/\text{Fe}]$  ratios are higher by  $\sim 0.2$  dex in metal-poor stars than those of other  $\alpha$ -elements, but this trend reverses for stars with  $[\text{Fe}/\text{H}] \gtrsim 0$  where  $[\text{O}/\text{Fe}]$  is, on average, lower by  $\sim 0.2$  dex. While both O and Mg are significant products of hydrostatic burning in massive stars (e.g., Woosley & Weaver 1995), the  $[\text{Mg}/\text{Fe}]$  trend exhibits a more shallow decline with increasing  $[\text{Fe}/\text{H}]$  than  $[\text{O}/\text{Fe}]$ . This is most clearly seen in Figure 12, which shows a sharply declining  $[\text{O}/\text{Mg}]$  ratio at  $[\text{Fe}/\text{H}] \gtrsim -0.1$ . Although massive star production of Si and Ca involves both hydrostatic and explosive burning (e.g., Woosley & Weaver 1995), the  $[\text{Si}/\text{Fe}]$  and  $[\text{Ca}/\text{Fe}]$  trends are more similar to  $[\text{Mg}/\text{Fe}]$  than  $[\text{O}/\text{Fe}]$ . Given the disparate trend of  $[\text{O}/\text{Fe}]$  compared to other  $\alpha$ -elements, and the low production of most  $\alpha$ -elements relative to Fe in Type Ia supernovae (SNe; e.g., Nomoto et al. 1997), we conclude in agreement with past work (e.g., McWilliam et al. 2008) that the strong decline in  $[\text{O}/\text{Fe}]$  at  $[\text{Fe}/\text{H}] \gtrsim -0.3$  is likely a result of metallicity dependent yields in massive stars<sup>15</sup>. The influence of metallicity dependent yields on the bulge composition profile, especially from Wolf-Rayet stars, is further supported by fluorine measurements (Cunha et al. 2008; Jönsson et al. 2014), but it remains to be seen if this scenario can be reconciled with the observed carbon and nitrogen trends (Ryde et al. 2010; but see also Cescutti et al. 2009).

When comparing the individual  $[\alpha/\text{Fe}]$  trends between the two fields analyzed here, Figure 11 shows no significant variations. Similarly, in Figure 13 we combine our two fields and compare with literature giant and dwarf  $[\alpha/\text{Fe}]$  data. A comparison between the present work

<sup>15</sup> We note that for standard stellar evolution models it is often difficult to produce a strong change in the  $[\text{O}/\text{Mg}]$  yield (e.g., Kobayashi et al. 2006; their Figure 9). Producing models with a declining  $[\text{O}/\text{Mg}]$  yield likely requires the inclusion of additional physics, such as mass loss from stellar winds or a process to cause a change in the  $[\text{C}/\text{O}]$  ratio.



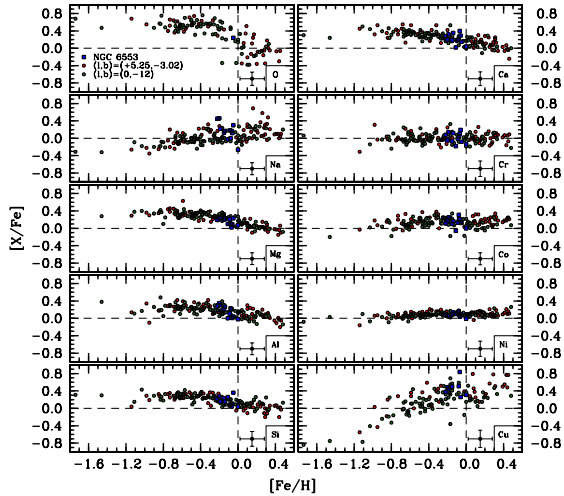


FIG. 11.—  $[X/Fe]$  abundance patterns plotted as a function of  $[Fe/H]$  for all elements analyzed. The filled red circles, filled green circles, and filled blue boxes differentiate stars belonging to the  $(+5.25, -3.02)$ ,  $(0, -12)$ , and NGC 6553 populations. Note that the scale of the ordinate is identical in all panels.

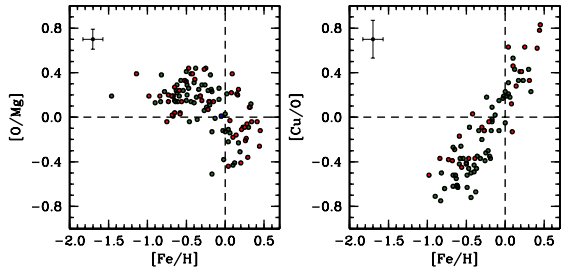


FIG. 12.— The  $[O/Mg]$  and  $[Cu/O]$  ratios are plotted as a function of  $[Fe/H]$ . The filled red circles, filled green circles, and filled blue boxes differentiate stars belonging to the  $(+5.25, -3.02)$ ,  $(0, -12)$ , and NGC 6553 populations.

and literature giant trends, which span a variety of bulge sight lines, leads us to find in agreement with Johnson et al. (2011; 2013) and Gonzalez et al. (2011) that no significant field-to-field  $[\alpha/Fe]$  variations exist over a broad region of the bulge. The microlensed dwarf data exhibit the same qualitative and quantitative distributions for  $[O/Fe]$  and  $[Mg/Fe]$ , at least for  $[Fe/H] \lesssim 0$ , as the giant data, but there may be small systematic offsets with  $[Si/Fe]$  and  $[Ca/Fe]$ . In particular, the dwarf abundances are  $\sim 0.1$  dex lower for a given  $[Fe/H]$ , when considering  $[Fe/H] \lesssim 0$ . At super-solar  $[Fe/H]$  values, the dwarf and giant data are in excellent agreement for  $[O/Fe]$ , but the leveling-off or slight increase in  $[Mg/Fe]$ ,  $[Si/Fe]$ , and  $[Ca/Fe]$  seems to be unique to the dwarf measurements. Unfortunately, the source of this discrepancy is not clear and may be related to analysis differences between dwarfs and giants.

In Figure 14 we compare the  $[O/Fe]$ ,  $[Mg/Fe]$ ,  $[Si/Fe]$ , and  $[Ca/Fe]$  abundances between the bulge, thick disk, and thin disk. For stars with  $[Fe/H] \lesssim -0.5$ , the bulge and thick disk stars exhibit similar abundance patterns for all four element ratios. However, we note that on average the bulge stars have  $[O/Fe]$  and  $[Mg/Fe]$  ratios that are slightly enhanced by  $\sim 0.03$  dex and  $[Si/Fe]$  and  $[Ca/Fe]$  ratios that are enhanced by  $\sim 0.05$  dex compared to similar metallicity thick disk stars. In contrast, the most metal-poor thin disk stars exhibit significantly

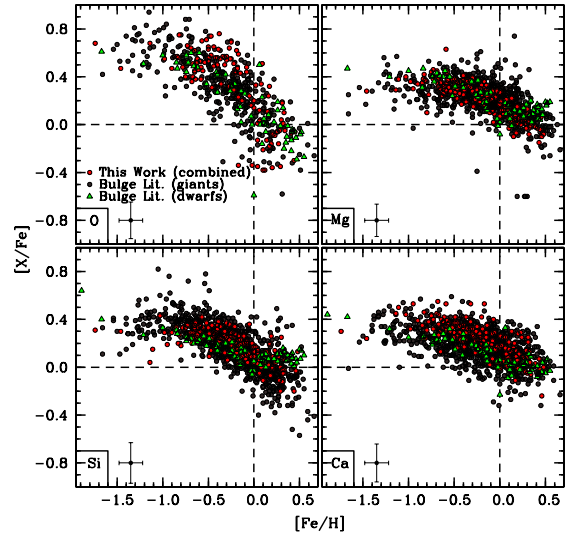


FIG. 13.—  $[X/Fe]$  ratios for the  $\alpha$ -elements O, Mg, Si, and Ca are plotted as a function of  $[Fe/H]$ . The filled red circles indicate abundances measured for this work (combining both fields and NGC 6553), the filled dark gray circles are abundances in bulge RGB and red clump stars from the literature, and the filled green triangles are abundances from bulge microlensed dwarfs (Bensby et al. 2013). The RGB and clump data are from: McWilliam & Rich (1994), Rich et al. (2005), Fulbright et al. (2007), Lecureur et al. (2007), Rich et al. (2007b), Meléndez et al. (2008), Alves-Brito et al. (2010), Ryde et al. (2010), Gonzalez et al. (2011), Hill et al. (2011), Johnson et al. (2011), Rich et al. (2012), García Pérez et al. (2013), and Johnson et al. (2013a,b).

lower  $[X/Fe]$  ratios for all of the  $\alpha$ -elements measured here. The bulge and thin disk stars with  $[Fe/H] \gtrsim 0$  are not strikingly different, but the star-to-star scatter, especially for  $[O/Fe]$ , is significantly larger for the bulge giants. For the intermediate range of  $[Fe/H] \sim -0.5$  to 0, the bulge stars still exhibit significantly larger  $[\alpha/Fe]$  ratios than the thin disk and may remain enhanced to a higher  $[Fe/H]$  value than the thick disk.

The chemical similarities between especially the metal-poor bulge and thick disk found here have been documented in previous work (Meléndez et al. 2008; Alves-Brito et al. 2010; Bensby et al. 2010a; Ryde et al. 2010; Bensby et al. 2011; Gonzalez et al. 2011; Hill et al. 2011; Johnson et al. 2011, 2013). The apparent homogeneity between the most metal-poor bulge and thick disk stars lends credibility to the idea that the Galactic bulge formed *in situ* with the disk. However, there is not universal agreement in the literature that the metal-poor bulge and disk trends are identical. In particular, earlier work by Zoccali et al. (2006), Fulbright et al. (2007), and Lecureur et al. (2007) found that the bulge stars exhibited both larger  $[\alpha/Fe]$  ratios and remained enhanced to higher  $[Fe/H]$  values than the local thick disk<sup>16</sup>, which implies a more rapid formation timescale for the bulge. In contrast, purely differential analyses between thick disk and bulge giants (Meléndez et al. 2008; Alves-Brito et al. 2010; Gonzalez et al. 2011) find nearly identical  $[\alpha/Fe]$  versus  $[Fe/H]$  trends, at least for  $[Fe/H] \lesssim -0.3$ . However, Bensby et al. (2013) noted in a similarly differential comparison of local thick disk dwarfs and bulge microlensed dwarfs that the inflection

<sup>16</sup> A comparison with the inner disk would be more appropriate; however, we note that Bensby et al. (2010b) do not find any significant chemical differences between local and inner disk stars.

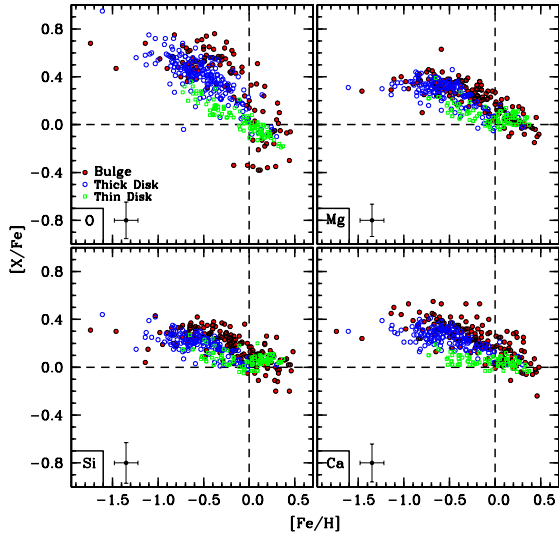


FIG. 14.— A comparison of the O, Mg, Si, and Ca abundances for the bulge stars measured here (filled red circles) with those of the thick disk (open blue circles) and thin disk (open green boxes). The disk data are from: Bensby et al. (2003; 2005) and Reddy et al. (2006).

point at which  $[\alpha/\text{Fe}]$  declines may be 0.1–0.2 dex higher ( $[\text{Fe}/\text{H}] \approx -0.3$  to  $-0.2$ ) in the bulge. While we compare bulge giants and thick disk dwarfs in Figure 14, our results are in agreement with Bensby et al. (2013). In particular, we find that the  $[\text{Mg}/\text{Fe}]$ ,  $[\text{Si}/\text{Fe}]$ , and perhaps  $[\text{O}/\text{Fe}]$  ratios remain enhanced to a higher  $[\text{Fe}/\text{H}]$  value than those of the local thick disk<sup>17</sup>.

Finally, we note that combining the present data set with those available in the literature (e.g., see Figure 13) totals  $\sim 10^3$  bulge stars that have had  $[\alpha/\text{Fe}]$  measurements made from high resolution spectroscopy. Despite the large sample size, there is a paucity of stars with  $[\alpha/\text{Fe}]$  ratios that deviate significantly from the bulk trend. In agreement with work suggesting the Galactic bulge did not form predominantly from a build-up of merger events (e.g., Shen et al. 2010), we can effectively rule out significant contributions from the infall of objects with chemistry similar to those of many present-day dwarf galaxies (i.e., low  $[\alpha/\text{Fe}]$ ; e.g., see Venn et al. 2004 and references therein). Additionally, as can be seen in Figure 11 (see also Gonzalez et al. 2011) the  $[\text{X}/\text{Fe}]$  abundance ratios of individual  $\alpha$ -elements for NGC 6553 stars are nearly identical to those of bulge field stars with similar  $[\text{Fe}/\text{H}]$ . Specifically, the average  $[\text{X}/\text{Fe}]$  values for NGC 6553 are:  $\langle [\text{O}/\text{Fe}] \rangle = +0.24$  (one star),  $\langle [\text{Mg}/\text{Fe}] \rangle = +0.16$  ( $\sigma = 0.08$ ),  $\langle [\text{Si}/\text{Fe}] \rangle = +0.17$  ( $\sigma = 0.10$ ), and  $\langle [\text{Ca}/\text{Fe}] \rangle = +0.22$  ( $\sigma = 0.12$ ), which compare well with the average abundances for nearby bulge field stars in the range  $[\text{Fe}/\text{H}] = -0.20$  to  $+0.00$ :  $\langle [\text{O}/\text{Fe}] \rangle = +0.24$  ( $\sigma = 0.29$ ),  $\langle [\text{Mg}/\text{Fe}] \rangle = +0.25$  ( $\sigma = 0.09$ ),  $\langle [\text{Si}/\text{Fe}] \rangle = +0.15$  ( $\sigma = 0.08$ ), and  $\langle [\text{Ca}/\text{Fe}] \rangle = +0.19$  ( $\sigma = 0.13$ ). These values are in good agreement with past work that finds the cluster to be moderately  $\alpha$ -enhanced (Barbuy et al. 1999; Cohen et al. 1999; Coelho et al. 2001; Origlia et al. 2002; Meléndez et al. 2003; Alves-Brito et al. 2006). The

<sup>17</sup> If we instead compare the  $[\alpha/\text{Fe}]$  ratios between bulge giants here and thick disk giants from Alves-Brito et al. (2010), we reach a similar conclusion. Both data sets exhibit similar abundance trends for  $[\text{O}/\text{Fe}]$  and  $[\text{Mg}/\text{Fe}]$ , but  $[\text{Si}/\text{Fe}]$  and  $[\text{Ca}/\text{Fe}]$  remain enhanced at higher  $[\text{Fe}/\text{H}]$  in the bulge giants.

similar  $[\alpha/\text{Fe}]$  abundances between the cluster and field stars suggests that NGC 6553 likely formed *in situ* with the bulge field population and is not a captured cluster.

#### 4.2. The Light, Odd-Z Elements Sodium and Aluminum

In a similar fashion to the  $\alpha$ -elements, the light, odd-Z elements Na and Al provide clues of the processes that dominated the chemical enrichment of a stellar population. Furthermore, these elements are useful for “chemical tagging” analyses, and both the  $[\text{Na}/\text{Fe}]$  and  $[\text{Al}/\text{Fe}]$  ratios can vary significantly between stellar populations that have otherwise identical  $[\alpha/\text{Fe}]$  and  $[\text{Fe}/\text{H}]$  values. The large ( $\gtrsim 0.5$  dex) star-to-star  $[\text{Na}/\text{Fe}]$  and  $[\text{Al}/\text{Fe}]$  abundance variations present in metal-poor globular cluster but not halo/disk stars of the same metallicity are perhaps the most well-known example of this phenomenon (e.g., see reviews by Gratton et al. 2004; 2012 and references therein). While the production of Na and Al is dominated by hydrostatic helium, carbon, and neon burning in massive stars, the final yields are expected to grow significantly with increasing progenitor mass and metallicity (e.g., Woosley & Weaver 1995; Kobayashi et al. 2006; 2011). Intermediate mass ( $\sim 4\text{--}8 M_{\odot}$ ) asymptotic giant branch (AGB) stars and the hydrogen-rich envelopes of massive stars can also produce significant amounts of Na and Al via the NeNa and MgAl proton-capture cycles (e.g., Decressin et al. 2007; de Mink et al. 2009; Ventura & D’Antona 2009; Karakas 2010). Since Na and Al are thought to result from similar production mechanisms, we expect their abundance patterns to reflect a comparable morphology.

While the bulge abundance patterns of  $[\text{Na}/\text{Fe}]$  and  $[\text{Al}/\text{Fe}]$  have not been investigated to the extent of the  $\alpha$ -elements, the combined literature sample now totals of order a few hundred stars. Interestingly, the agreement between studies regarding the  $[\text{Na}/\text{Fe}]$  and  $[\text{Al}/\text{Fe}]$  trends is worse than for the  $\alpha$ -elements. While all high-resolution analyses (McWilliam & Rich 1994; Fulbright et al. 2007; Lecureur et al. 2007; Alves-Brito et al. 2010; Bensby et al. 2010a, 2011; Johnson et al. 2012; Bensby et al. 2013) tend to agree that the average  $[\text{Na}/\text{Fe}]$  ratio rises with increasing metallicity, significant scatter is present at  $[\text{Fe}/\text{H}] \lesssim -1$  and  $[\text{Fe}/\text{H}] \gtrsim 0$ . Similarly, there is general agreement that  $[\text{Al}/\text{Fe}]$  is enhanced in bulge stars at  $[\text{Fe}/\text{H}] \lesssim -0.3$ . However, some studies find that  $[\text{Al}/\text{Fe}]$  remains enhanced at super-solar metallicities (McWilliam & Rich 1994; Fulbright et al. 2007; Lecureur et al. 2007; Alves-Brito et al. 2010) while others find a decline in  $[\text{Al}/\text{Fe}]$ , similar to  $[\alpha/\text{Fe}]$  (Bensby et al. 2011, 2011; Johnson et al. 2012; Bensby et al. 2013). Additionally, there is general agreement that the  $[\text{Na}/\text{Fe}]$  and  $[\text{Al}/\text{Fe}]$  trends as a function of  $[\text{Fe}/\text{H}]$  are similar between the bulge and disk over a broad metallicity range, but differences could be present at the metal-poor and metal-rich ends of the bulge distribution. It is also not yet clear if any significant  $[\text{Na}/\text{Fe}]$  and  $[\text{Al}/\text{Fe}]$  abundance differences exist between different bulge sight lines.

Figure 11 shows our derived  $[\text{Na}/\text{Fe}]$  and  $[\text{Al}/\text{Fe}]$  abundances as a function of  $[\text{Fe}/\text{H}]$  for both fields and the possible NGC 6553 stars, and in Figure 15 we compare our results with those from previous work. For Na we find general agreement with literature values such that the average  $[\text{Na}/\text{Fe}]$  ratio rises with increasing  $[\text{Fe}/\text{H}]$ . However, we find only a small number of metal-rich stars

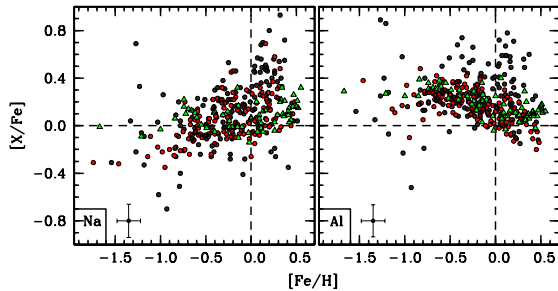


FIG. 15.— A comparison plot of  $[\text{Na}/\text{Fe}]$  and  $[\text{Al}/\text{Fe}]$  ratios between the bulge RGB stars measured here (filled red circles), RGB and clump stars available in the literature (filled dark gray circles), and bulge microlensed dwarfs (filled green triangles). Additional dwarf and giant literature data are from: Johnson et al. (2007; 2008), Cohen et al. (2008; 2009), Epstein et al. (2010), and Johnson et al. (2012), in addition to those referenced in Figure 13.

with  $[\text{Na}/\text{Fe}] > +0.4$  and do not reproduce the very large  $[\text{Na}/\text{Fe}]$  ratios of *Lecureur et al. (2007)*. Additionally, we do not find significant evidence supporting large  $[\text{Na}/\text{Fe}]$  variations between the two bulge sight lines probed here. At  $[\text{Fe}/\text{H}] \gtrsim -0.5$ , the mean  $[\text{Na}/\text{Fe}]$  trend and star-to-star dispersion for our measured RGB stars is in good agreement with those of the microlensed bulge dwarfs (e.g., *Bensby et al. 2013*).

The primary discrepancy between our work and some of the literature values occurs for stars with  $[\text{Fe}/\text{H}] \lesssim -0.7$ , with the present work and *Johnson et al. (2012)* finding that the average Na trend decreases from  $[\text{Na}/\text{Fe}] \sim 0$  at  $[\text{Fe}/\text{H}] = -0.5$  to  $[\text{Na}/\text{Fe}] = -0.3$  at  $[\text{Fe}/\text{H}] = -1.7$ . It is not immediately clear if the discrepancy, especially between the bulge RGB and dwarf data, is real or caused by analysis differences (e.g., NLTE, 3D, or spherical/plane-parallel effects between dwarfs and giants). The inclusion of NLTE corrections would minimize the differences at low metallicity between bulge RGB and dwarf stars, and also between bulge RGB and metal-poor thick disk dwarfs (see Figure 16), if the largely positive Na corrections for RGB stars from *Gratton et al. (1999)* were applied. However, more recent NLTE calculations (e.g., *Lind et al. 2011*) instead find that the sign of the Na correction is negative for the lines and atmospheric parameters used here. Similarly, the NLTE corrections for  $\log \epsilon(\text{Fe I})$  appear to be positive (e.g., *Lind et al. 2012; Bergemann et al. 2012*) for most stars in our sample<sup>18</sup>, which would decrease the  $[\text{Na}/\text{Fe}]$  ratios. Further insights into this problem may be gained as more extensive NLTE calculations and 3D model atmosphere grids and codes become available.

When comparing the  $[\text{Na}/\text{Fe}]$  and  $[\text{Al}/\text{Fe}]$  trends in Figure 11, it is immediately clear that the two elements exhibit discrepant trends. While  $[\text{Na}/\text{Fe}]$  gradually rises with increasing  $[\text{Fe}/\text{H}]$ , the  $[\text{Al}/\text{Fe}]$  trend is nearly indistinguishable from that of most  $\alpha$ -elements. In particular, we find in agreement with *Bensby et al. (2010a; 2011; 2013)* and *Johnson et al. (2012)* that  $[\text{Al}/\text{Fe}] \sim +0.3$  in bulge stars until  $[\text{Fe}/\text{H}] \sim -0.3$  and then steadily declines at higher  $[\text{Fe}/\text{H}]$ . As mentioned previously, the decline in  $[\text{Al}/\text{Fe}]$  with increasing metallicity contrasts with other literature results that find  $[\text{Al}/\text{Fe}]$  remains enhanced even

<sup>18</sup> The NLTE corrections for a subset of “typical” stars and lines were calculated using the INSPECT website: <http://www.inspect-stars.net>.

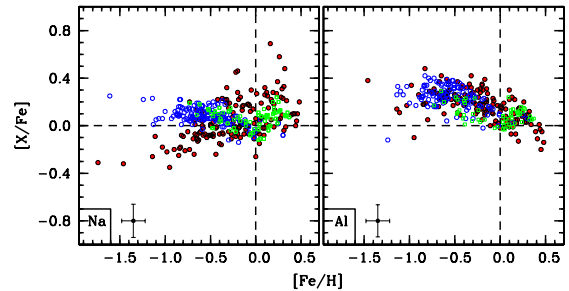


FIG. 16.— A plot of  $[\text{Na}/\text{Fe}]$  and  $[\text{Al}/\text{Fe}]$  ratios as a function of  $[\text{Fe}/\text{H}]$  for the bulge stars measured here (filled red circles), thick disk stars (open blue circles), and thin disk stars (open green boxes). The literature data are from the sources referenced in Figure 14.

at  $[\text{Fe}/\text{H}] = +0.5$  (*Fulbright et al. 2007; Lecureur et al. 2007; Alves-Brito et al. 2010*). The data quality among the various studies is comparable, and it is not clear why the derived  $[\text{Al}/\text{Fe}]$  trends are in disagreement at high metallicity. We do note however that for cool, high metallicity stars the 6696 and especially 6698 Å Al I lines, as well as the continuum placement, can be affected by CN blending.

The discrepant  $[\text{Na}/\text{Fe}]$  and  $[\text{Al}/\text{Fe}]$  trends as a function of  $[\text{Fe}/\text{H}]$  are not limited to the bulge and may also be present in the disk, as can be seen in Figure 16. Despite nucleosynthesis models predicting similar production of Na and Al in massive stars (e.g., *Woosley & Weaver 1995*), Figure 16 shows that, at least in the metallicity range probed here, Al is over-produced relative to Na in both bulge and disk stars for  $[\text{Fe}/\text{H}] \lesssim -0.3$ . The increased production of Na relative to Al in metal-rich stars, and especially in the bulge, suggests that metallicity dependent yields from massive stars vary more strongly for Na than Al. Contributions from intermediate mass AGB stars may also help explain the Na and Al trends since the AGB  $[\text{Na}/\text{Fe}]$  yields tend to increase at higher  $[\text{Fe}/\text{H}]$  while those of  $[\text{Al}/\text{Fe}]$  decline (e.g., *Ventra & D’Antona 2009*). Interestingly, we find that, unlike the case for  $[\text{Na}/\text{Fe}]$ , the  $[\text{Al}/\text{Fe}]$  ratios are nearly indistinguishable between the bulge and thick disk at  $[\text{Fe}/\text{H}] < 0$ . Similarly, the  $[\text{Al}/\text{Fe}]$  ratios for bulge stars are identical to those in the thin disk at  $[\text{Fe}/\text{H}] > 0$ .

Given the similar behavior of  $[\text{Al}/\text{Fe}]$  to many of the  $\alpha$ -elements, in Figure 17 we provide a detailed comparison between  $[\text{Al}/\text{Fe}]$ ,  $[\text{O}/\text{Fe}]$ ,  $[\text{Mg}/\text{Fe}]$ ,  $[\text{Si}/\text{Fe}]$ , and  $[\text{Ca}/\text{Fe}]$  for the bulge stars analyzed here. While the  $[\text{O}/\text{Fe}]$  trend is clearly different than that of  $[\text{Al}/\text{Fe}]$ , there are no similarly strong discrepancies between  $[\text{Al}/\text{Fe}]$  and the other  $\alpha$ -elements. At  $[\text{Fe}/\text{H}] < -0.8$  both  $[\text{Mg}/\text{Fe}]$  and  $[\text{Ca}/\text{Fe}]$  are  $\sim 0.10$ – $0.15$  dex enhanced compared to  $[\text{Al}/\text{Fe}]$ , but those differences disappear at higher  $[\text{Fe}/\text{H}]$ . On the other hand, the  $[\text{Si}/\text{Fe}]$  and  $[\text{Al}/\text{Fe}]$  trends are essentially identical at all  $[\text{Fe}/\text{H}]$  with an average difference of 0.01 dex ( $\sigma = 0.13$  dex).

Examining the NGC 6553 stars in Figure 11 shows that Na, and to a lesser extent Al, exhibit larger star-to-star  $[\text{Na}/\text{Fe}]$  and  $[\text{Al}/\text{Fe}]$  variations than similar metallicity field stars. In particular, the average Na and Al abundances for the cluster stars are  $\langle [\text{Na}/\text{Fe}] \rangle = +0.16$  ( $\sigma = 0.20$ ) and  $\langle [\text{Al}/\text{Fe}] \rangle = +0.17$  ( $\sigma = 0.13$ ), which can be compared to the similar metallicity field stars having  $\langle [\text{Na}/\text{Fe}] \rangle = +0.03$  ( $\sigma = 0.11$ ) and  $\langle [\text{Al}/\text{Fe}] \rangle = +0.16$

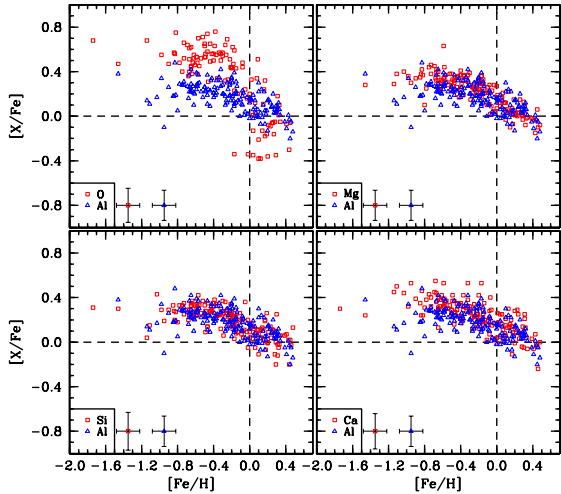


FIG. 17.—  $[\text{Al}/\text{Fe}]$  ratios (open blue triangles) for all bulge and NGC 6553 RGB stars analyzed here are compared to the abundance trends of the  $\alpha$ -elements O, Mg, Si, and Ca (open red boxes).

( $\sigma=0.10$ ), respectively. The larger  $[\text{Na}/\text{Fe}]$  abundance and dispersion values for the cluster stars suggests NGC 6553 experienced some degree of self-enrichment. However, unlike low metallicity globular clusters, NGC 6553 does not exhibit a strong Na–Al correlation. This is in agreement with the observed trend that the Na–Al correlation is more mild and  $[\text{Al}/\text{Fe}]$  dispersions smaller in metal-rich as opposed to metal-poor globular clusters (e.g., Carretta et al. 2009; O’Connell et al. 2011; Cordero et al. 2014). Unfortunately, the 6300 Å telluric oxygen emission feature combined with NGC 6553’s relatively low radial velocity prohibited us from obtaining an  $[\text{O}/\text{Fe}]$  abundance for more than one star in NGC 6553. Therefore, we cannot comment further on the existence or extension of the likely O–Na correlation. Finally, we note that our mean  $[\text{Na}/\text{Fe}]$  and  $[\text{Al}/\text{Fe}]$  values and abundance dispersions are in excellent agreement with those found by Alves-Brito et al. (2006), but are considerably lower than the values (based on two stars) of Barbuy et al. (1999).

#### 4.3. The Fe-Peak Elements: Chromium, Cobalt, Nickel, and Copper

Unlike the lighter elements, the abundance patterns of Fe-peak elements in the Galactic bulge are not well-explored. The production of Fe-peak elements occurs through a variety of processes in the late stages of massive star evolution, the resulting core collapse SNe, and also in Type Ia SNe. The Fe-peak abundance patterns can also be useful indicators of a stellar population’s IMF, with odd- $Z$  elements in particular providing some diagnostic power (e.g., Nomoto et al. 2013). Some initial work on the bulge Fe-peak abundance distribution was included in McWilliam & Rich (1994), which found  $[\text{V}/\text{Fe}]$ ,  $[\text{Cr}/\text{Fe}]$ , and  $[\text{Ni}/\text{Fe}]$  ratios near solar and a possible enhancement in  $[\text{Co}/\text{Fe}]$  and  $[\text{Sc}/\text{Fe}]$ . More recent work analyzing the Fe-peak abundance trends in the bulge has come from microlensed dwarf studies (Cohen et al. 2008; Johnson et al. 2008; Cohen et al. 2009; Bensby et al. 2010a; Epstein et al. 2010; Bensby et al. 2011; Bensby et al. 2013). The bulge  $[\text{Mn}/\text{Fe}]$  trend in RGB stars has also been investigated recently by Barbuy et al. (2013). The results of these analyses indicate that

the bulge Fe-peak trends are similar to that of the local disk, except that the bulge may have different  $[\text{Mn}/\text{O}]$  ratios than the thick disk for a given  $[\text{O}/\text{H}]$  value.

The general  $[\text{X}/\text{Fe}]$  versus  $[\text{Fe}/\text{H}]$  abundance trends derived here are shown in Figure 11. From these data we find that: (1) Cr is the element that most closely tracks Fe with  $\langle[\text{Cr}/\text{Fe}]\rangle=0.00$  ( $\sigma=0.11$ ), (2)  $[\text{Co}/\text{Fe}]$  exhibits low level variations as a function of  $[\text{Fe}/\text{H}]$  but is generally enhanced with  $\langle[\text{Co}/\text{Fe}]\rangle=+0.14$  ( $\sigma=0.11$ ), (3)  $[\text{Ni}/\text{Fe}]$  shows similar variations to  $[\text{Co}/\text{Fe}]$  but at a much smaller amplitude and is slightly enhanced with  $\langle[\text{Ni}/\text{Fe}]\rangle=+0.09$  ( $\sigma=0.06$ ), (4) the Cu abundance increases monotonically from  $[\text{Cu}/\text{Fe}]=-0.84$  in the most metal-poor star to  $[\text{Cu}/\text{Fe}]\sim+0.40$  in the most metal-rich stars, and (5) there are no significant Fe-peak abundance variations between NGC 6553 stars and the field stars.

Although the exact nature of Cu nucleosynthesis is complex (e.g., see Mishenina et al. 2002 and references therein), the significant secondary (i.e., metallicity-dependent) production of Cu (and also Na) is evident in Figure 11. Additionally, Figure 12 shows that despite the larger measurement errors in both O and Cu abundances, the  $[\text{Cu}/\text{O}]$  ratio is strongly correlated with  $[\text{Fe}/\text{H}]$ . This trend has been noted previously and is prevalent in stellar populations with different star formation histories, such as the local disk and Sagittarius Dwarf Galaxy (e.g., McWilliam et al. 2013). The  $[\text{Cu}/\text{O}]$  trend is taken as evidence that a significant portion of Cu is synthesized in massive stars, perhaps via the weak s-process (e.g., Sneden et al. 1991). However, some component of Cu may also be produced by Type Ia SNe (Matteucci et al. 1993).

In Figure 18 we compare our derived Fe-peak abundance trends with those in the literature. For Cr there is general agreement between the bulge RGB stars analyzed here and the literature microlensed dwarf data. However, the small number of bulge literature data points for Co and Cu makes a direct comparison difficult. The  $[\text{Ni}/\text{Fe}]$  comparison also shows excellent agreement overall, but the RGB stars appear systematically enhanced by  $\lesssim 0.1$  dex in the range  $[\text{Fe}/\text{H}]=-0.3$  to  $+0.1$ . Note also the similarly small star-to-star dispersion in especially  $[\text{Ni}/\text{Fe}]$  between the RGB and dwarf data.

A comparison between the bulge Fe-peak abundance trends and those of the thin/thick disk is shown in Figure 19. Interestingly, at least for  $[\text{Fe}/\text{H}]\gtrsim-1.5$ , the  $[\text{Cr}/\text{Fe}]$  distribution is seemingly independent of formation environment with the bulge, thick disk, and thin disk stars all having  $[\text{Cr}/\text{Fe}]\sim 0$ . For  $[\text{Co}/\text{Fe}]$ ,  $[\text{Ni}/\text{Fe}]$ , and  $[\text{Cu}/\text{Fe}]$ , there is significant overlap between the bulge and thick disk trends at  $[\text{Fe}/\text{H}]\lesssim-0.5$ . At higher  $[\text{Fe}/\text{H}]$ , the bulge may be enhanced in all three elements relative to both the thick and thin disks. This is especially evident in the Figure 19 panel showing  $[\text{Ni}/\text{Fe}]$  versus  $[\text{Fe}/\text{H}]$ ; the low star-to-star scatter in  $[\text{Ni}/\text{Fe}]$  for all three populations highlights the possible composition difference between the local disk and bulge from  $[\text{Fe}/\text{H}]\sim-0.4$  to  $+0.2$ . While the strong rise in  $[\text{Cu}/\text{Fe}]$  with metallicity is, as mentioned previously, a common feature in many different stellar populations, the bulge stars at  $[\text{Fe}/\text{H}]\gtrsim-0.3$  appear to extend to higher abundances than the local disk. However, the increased measurement uncertainty of Cu and paucity of disk  $[\text{Cu}/\text{Fe}]$  ratios at  $[\text{Fe}/\text{H}]>0$  prevents

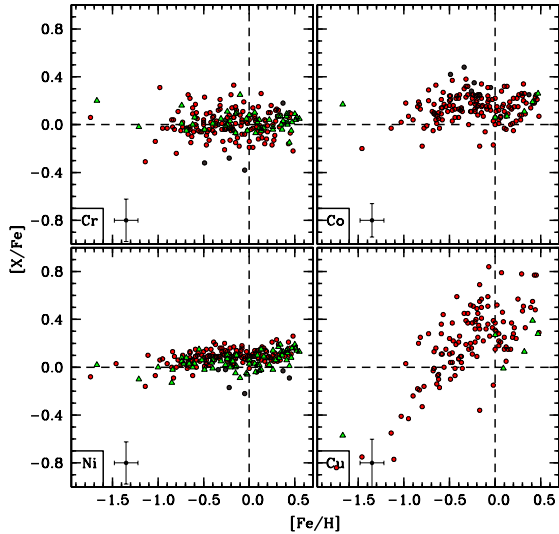


FIG. 18.— Plots comparing the  $[\text{Cr}/\text{Fe}]$ ,  $[\text{Co}/\text{Fe}]$ ,  $[\text{Ni}/\text{Fe}]$ , and  $[\text{Cu}/\text{Fe}]$  abundances of the bulge stars measured here (filled red circles) with literature measurements of bulge microlensed dwarfs (filled green triangles) and field RGB/red clump stars (filled dark gray circles). The literature data are from the sources referenced in Figures 13 and 15.

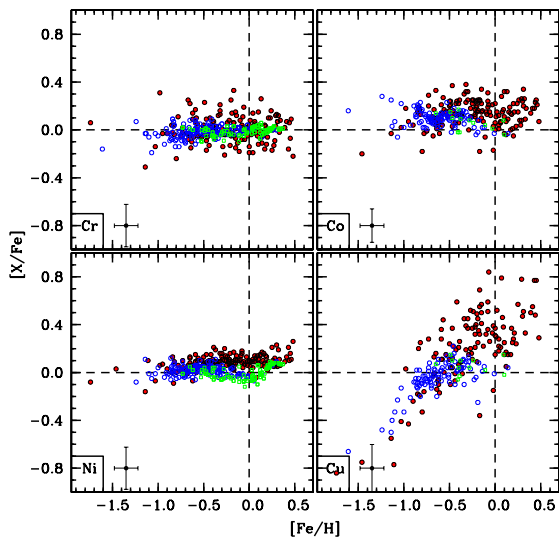


FIG. 19.— Plots comparing the  $[\text{Cr}/\text{Fe}]$ ,  $[\text{Co}/\text{Fe}]$ ,  $[\text{Ni}/\text{Fe}]$ , and  $[\text{Cu}/\text{Fe}]$  abundances of the bulge stars measured here (filled red circles) with literature data for the thick disk (open blue circles) and thin disk (open green boxes). The literature data are from the sources referenced in Figure 14.

us from undertaking a more comprehensive analysis.

#### 4.4. Comparing Composition Data to Bulge Chemical Enrichment Models

Accurately modeling the chemical enrichment history of a stellar system requires solving for a variety of free parameters that may include the IMF, star formation rate, star formation efficiency, supernova/hypernova ratio<sup>19</sup>, inflow/outflow rate, binary fraction, stellar evolution time scales, mass loss rates, and stellar yields. While not all of the required input parameters are yet

<sup>19</sup> Note that the model hypernova fractions only affect stars with  $M > 20 M_{\odot}$

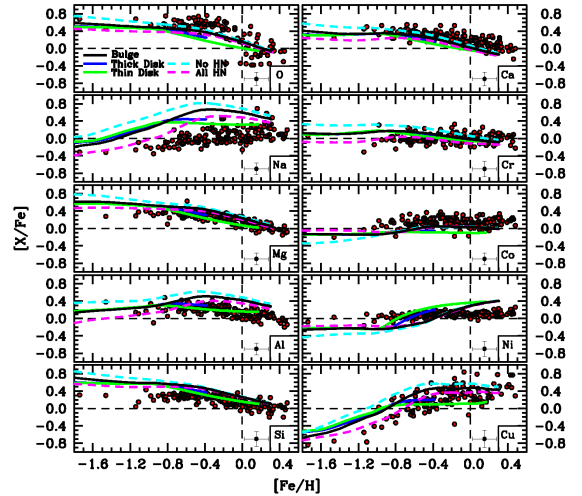


FIG. 20.— Chemical abundance trends are plotted as a function of  $[\text{Fe}/\text{H}]$  and compared to various chemical enrichment models. The solid black, blue, and green lines represent the baseline models from Kobayashi et al. (2006; 2011) for the Galactic bulge, thick disk, and thin disk, respectively. The dashed cyan and magenta lines illustrate how the bulge model changes if the hypernova fraction is 0 and 1, respectively, for masses  $> 20 M_{\odot}$ . Note that  $[\text{Ni}/\text{Fe}]$  in particular suffers from over-production from Type Ia SNe at  $[\text{Fe}/\text{H}] > -1$ . Some other elements (e.g., Si) may also be better fit if systematic offsets were applied.

well-defined based on observed data, chemical enrichment models are effective tools for examining and interpreting chemical composition data. Therefore, in Figures 20–21 we compare our derived abundance trends with those predicted by chemical enrichment models in which parameters such as the IMF, binary fraction, supernova/hypernova ratio, and outflow rate are varied.

The baseline Galactic bulge model shown in Figures 20–21 is from Kobayashi et al. (2006; 2011) and is designed to reproduce the metallicity distribution in Baade’s Window from Zoccali et al. (2008), assumes a Kroupa (2008) IMF, and assumes a star formation time scale of 3 Gyr (see Kobayashi et al. 2011; their Table 1 and Section 2.4 for more detail regarding model input parameters). In general, the baseline model does a reasonable job of reproducing the observed abundance trends of all abundance ratios, except  $[\text{Na}/\text{Fe}]$  and  $[\text{Al}/\text{Fe}]$ . All of the models shown in Figures 20–21 predict large over-abundances of both  $[\text{Na}/\text{Fe}]$  and  $[\text{Al}/\text{Fe}]$  that are not observed, suggesting the massive star yields of both elements may be too high<sup>20</sup>. However, as can be seen in Figure 20, the enhanced Fe production from hypernovae (HNe) decreases the  $[\text{Na}/\text{Fe}]$  and  $[\text{Al}/\text{Fe}]$  yields and brings the baseline bulge model into better agreement with the light element data. The addition of HNe also provides better agreement between the models and observations for the Fe-peak elements, with a trade off of  $[\alpha/\text{Fe}]$  ratios that may be slightly too low. In contrast, Figure 20 also shows that a paucity of HNe generally leads to  $[\text{X}/\text{Fe}]$  ratios that are too high. It seems that a significant fraction of HNe are required to accurately reproduce the observed bulge abundance trends. Unfortunately, the HN fraction is best constrained at  $[\text{Fe}/\text{H}] \lesssim -1$ , where data are scarce.

<sup>20</sup> Noting again the possible effects of additional physics in the stellar models, adding rotation would likely increase the Na and Al yields.

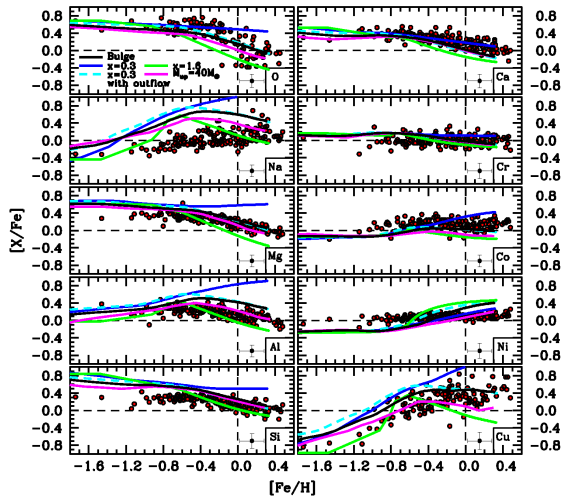


FIG. 21.— Similar to Figure 20, the solid black line is our adopted baseline bulge model from Kobayashi et al. (2006; 2011). The solid blue line is the baseline bulge model with a top-heavy (flatter) IMF, and the dashed cyan line is the same model but with outflow and an increased Type Ia SN rate ( $10\times$ ). The solid green line is the baseline bulge model with a steep IMF. The solid magenta line is the baseline bulge model with the IMF truncated at an upper mass limit of  $40 M_{\odot}$ .

In Figure 21 we examine how changes in the IMF could affect the expected abundance trends. Compared to the Kroupa (2008) IMF adopted in our baseline bulge model, a steep IMF ( $x=1.6$ ) is completely ruled out by the data. Additionally, adopting a Kroupa (2008) IMF that truncates at  $40 M_{\odot}$ , and thus ignores contributions from the most massive stars, is inconsistent with the  $[\text{Cu}/\text{Fe}]$  abundances, and to a lesser extent those of  $[\text{Co}/\text{Fe}]$ . While a flatter, top-heavy IMF ( $x=0.3$ ) alone leads to  $[\text{X}/\text{Fe}]$  ratios that are too high for nearly every element, a reduction in the yields from outflow and/or slow star-formation combined with a high Type Ia SN rate, artificially enhanced with a ten times larger binary fraction, could bring such a model into agreement with the data. However, bulge formation models with slow star-formation are likely unrealistic, and the observed  $[\text{Co}/\text{Fe}]$  and  $[\text{Cu}/\text{Fe}]$  data appear to rule out these models. Based on the present data it does not appear that the bulge required a uniquely “non-standard” IMF to reach its present-day composition (but see also Ballero et al. 2007, for example).

Finally, in Figure 20 we also compare the measured bulge abundance trends with our adopted baseline model and similar models representing the composition distributions of the local thick disk and thin disk. Comparing the three predicted trends indicates that in the range  $-0.8 \lesssim [\text{Fe}/\text{H}] \lesssim -0.3$  the bulge  $[\alpha/\text{Fe}]$  ratios should be similar or modestly enhanced and remain enhanced to higher  $[\text{Fe}/\text{H}]$  than the thick disk. Similarly, at  $[\text{Fe}/\text{H}] \gtrsim 0$  the bulge and thin disk should exhibit similar, if not identical,  $[\alpha/\text{Fe}]$  ratios. Both of these predictions match our observations (see Section 4.1). The predicted enhancements in the bulge for  $[\text{Na}/\text{Fe}]$  and  $[\text{Al}/\text{Fe}]$  compared to the local disk are not supported by observations, but this could be related to the previously mentioned possible over-production issues of the adopted stellar yields. However, in addition to Na and Al, Figure 20 shows that Co and Cu may also exhibit some discriminating power between the bulge and local disk populations. In par-

ticular, the data support bulge stars with  $[\text{Fe}/\text{H}] \gtrsim -0.5$  having  $[\text{Co}/\text{Fe}]$  and  $[\text{Cu}/\text{Fe}]$  ratios that are higher than the local disk. Therefore, the data and models presented here provide some supporting evidence that the bulge experienced a different chemical enrichment path than the thick disk.

## 5. SUMMARY

We have measured radial velocities and chemical abundances of O, Na, Mg, Al, Si, Ca, Cr, Fe, Co, Ni, and Cu in a sample of 156 RGB stars located in Galactic bulge fields centered near  $(l,b)=(+5.25,-3.02)$  and  $(0,-12)$ . The  $(+5.25,-3.02)$  also includes 12 stars identified as likely members of the bulge globular cluster NGC 6553, based on their radial velocity and  $[\text{Fe}/\text{H}]$  values. The results are based on high resolution archival spectra obtained with the FLAMES-GIRAFFE instrument, and originally used to derive  $[\text{Fe}/\text{H}]$  and  $[\alpha/\text{Fe}]$  abundances in Zoccali et al. (2008) and Gonzalez et al. (2011). We culled the original target list and selected only those stars with co-added  $\text{S/N} \gtrsim 70$  that also lack strong TiO bands. The abundance analysis was carried-out using standard EW and spectrum synthesis techniques.

Our derived heliocentric radial velocity distributions for both fields are in good agreement with past surveys (BRAVA, GIBS, and APOGEE) covering nearby fields. We do not confirm the existence of a significant population of high velocity stars noted by Nidever et al. (2012) and Babusiaux et al. (2014). However, our targeted fields are farther away from the plane than most of those in which Nidever et al. (2012) and Babusiaux et al. (2014) observe the cold, high velocity stars. For both fields analyzed here we also find that the velocity dispersion monotonically decreases with increasing  $[\text{Fe}/\text{H}]$ . This is not unexpected for the outer bulge field at  $(0,-12)$ , but the similar trend in the  $(+5.25,-3.02)$  field appears to contradict the findings of Babusiaux et al. (2010; 2014) that the velocity dispersion of bulge stars with  $[\text{Fe}/\text{H}] \gtrsim 0$  increases at lower Galactic latitude. The reason for this discrepancy is not clear, but we note that previous analyses finding increased velocity dispersion at low Galactic latitude for metal-rich stars have all focused on minor-axis fields. The inner bulge field included here is several degrees off-axis.

The composition data reconfirm the already well-documented metallicity gradient in the bulge. Similarly, we find good agreement between our derived  $[\text{Mg}/\text{Fe}]$ ,  $[\text{Si}/\text{Fe}]$ , and  $[\text{Ca}/\text{Fe}]$  abundances and those of Gonzalez et al. (2011). Additionally, we confirm that there are no significant field-to-field  $[\alpha/\text{Fe}]$  abundance variations among various bulge sight lines. Our new  $\alpha$ -element measurements also reinforce the previously held notion (e.g., McWilliam et al. 2008) that the decline in  $[\text{O}/\text{Mg}]$  with increasing metallicity is likely the result of metallicity dependent yields from massive stars. While we find that the bulge and thick disk exhibit nearly identical  $[\alpha/\text{Fe}]$  ratios at  $[\text{Fe}/\text{H}] \lesssim -0.5$ , the bulge stars appear to remain enhanced in  $[\alpha/\text{Fe}]$  by up to 0.1–0.2 dex higher in  $[\text{Fe}/\text{H}]$  than the local thick disk. The bulge  $[\alpha/\text{Fe}]$  ratios at  $[\text{Fe}/\text{H}] \gtrsim 0$  are well-matched to the local thin disk trends. These results are in agreement with recent differential abundance analyses of microlensed bulge dwarfs (Bensby et al. 2013), and suggest the bulge experienced faster enrichment than the local thick disk. However,

similar differential analyses comparing bulge and thick disk giants find no significant differences between the two populations (Meléndez et al. 2008; Alves-Brito et al. 2010; Gonzalez et al. 2011).

Combining the new data set of  $[\alpha/\text{Fe}]$  abundances with those available in the literature now totals several hundred stars. However, the combined data set does not reveal any significant population with “anomalous” chemistry, such as the low  $[\alpha/\text{Fe}]$  ratios reminiscent of many present-day dwarf galaxy stars. Therefore, we can effectively rule out these types of objects as major contributors to any portion of the present-day Galactic bulge field population. This further supports the idea that the Galactic bulge is not a merger-built system. Similarly, the  $[\alpha/\text{Fe}]$  ratios of the NGC 6553 stars are identical to those of similar metallicity field stars. This suggests NGC 6553 formed *in situ* with the bulge and is not a captured system.

With regard to the light, odd-Z elements, we find that Na and Al exhibit discrepant trends as a function of metallicity. In particular, bulge stars exhibit a steady increase in  $[\text{Na}/\text{Fe}]$  with increasing  $[\text{Fe}/\text{H}]$ , but the  $[\text{Al}/\text{Fe}]$  trend almost exactly matches that of the  $\alpha$ -elements (except oxygen). While we do not find any significant field-to-field variations in either  $[\text{Na}/\text{Fe}]$  or  $[\text{Al}/\text{Fe}]$ , our results indicate that the bulge and thick disk have different  $[\text{Na}/\text{Fe}]$  abundances at  $[\text{Fe}/\text{H}] \lesssim -0.5$  but similar  $[\text{Al}/\text{Fe}]$ . Interestingly, the “ $\alpha$ -like” behavior of  $[\text{Al}/\text{Fe}]$  contrasts with several previous bulge studies that found  $[\text{Al}/\text{Fe}]$  was enhanced up to  $[\text{Fe}/\text{H}] = +0.5$ . Instead, our results are in agreement with the abundance patterns of microlensed bulge dwarfs (e.g., Bensby et al. 2013). The discrepant behavior of Na and Al suggests metallicity dependent yields from massive stars, and perhaps intermediate mass stars, leads to significantly more production of Na than Al at high metallicity. We also find that the NGC 6553 stars have nearly identical  $[\text{Al}/\text{Fe}]$  ratios as similar metallicity field stars, but both the average  $[\text{Na}/\text{Fe}]$  abundance and star-to-star dispersion of cluster stars are higher. This suggests NGC 6553 experienced some light element self-enrichment, which is typical for globular clusters.

The abundance trends of the Fe-peak elements are distinctly different: (1) the average  $[\text{Cr}/\text{Fe}]$  ratio is essentially solar over the full range in  $[\text{Fe}/\text{H}]$  and shows no variations over the metallicity range probed here, (2) both  $[\text{Co}/\text{Fe}]$  and  $[\text{Ni}/\text{Fe}]$  are enhanced by  $\sim +0.1$  dex at nearly all  $[\text{Fe}/\text{H}]$  and exhibit some low amplitude, metallicity-dependent variations, and (3)  $[\text{Cu}/\text{Fe}]$  exhibits a large increase from the metal-poor to metal-rich end of the distribution. In a similar fashion to  $[\text{Na}/\text{Fe}]$ , the strong secondary (metallicity-dependent) production

of Cu is evident in bulge stars, and the correlation between  $[\text{Cu}/\text{O}]$  and  $[\text{Fe}/\text{H}]$  suggests massive stars produce significant portions of Cu. However, Cu production from another source (e.g., Type Ia SNe) seems required to explain the high  $[\text{Cu}/\text{Fe}]$  abundances at super-solar metallicities. Interestingly, at  $[\text{Fe}/\text{H}] \gtrsim -2$  the  $[\text{Cr}/\text{Fe}]$  trend is identical between the bulge, thick disk, and thin disk, but the heavier Fe-peak  $[\text{X}/\text{Fe}]$  ratios appear to all be enhanced in the bulge relative to the local disk. Additionally, the NGC 6553 Fe-peak abundance trends are in agreement with similar metallicity field stars.

Despite predicting  $[\text{Na}/\text{Fe}]$ ,  $[\text{Al}/\text{Fe}]$ , and  $[\text{Ni}/\text{Fe}]$  ratios that are too high, our adopted baseline bulge chemical enrichment model from Kobayashi et al. (2006; 2011) does a reasonable job fitting the abundance trends of the  $\alpha$  and other Fe-peak elements. However, better agreement between the data and model is found when a significant fraction of HNe, which produce more Fe, are included. Unfortunately, setting the HN fraction is best constrained using abundance patterns at  $[\text{Fe}/\text{H}] \lesssim -1$ , where the bulge data are sparse. While a Kroupa (2008) IMF provides a reasonable fit to the observed abundance trends, a top-heavy IMF including strong outflow cannot be ruled out. In contrast, the Fe-peak abundance data strongly rule out IMFs that are truncated to exclude the contributions of stars  $>40 M_{\odot}$ , steep IMFs (e.g.,  $x=1.6$ ), and top-heavy IMFs that do not include outflow. We conclude that the bulge likely does not require a particularly unusual IMF to explain its present-day abundance patterns, and that its enhanced abundances for several  $\alpha$  and Fe-peak elements match model predictions in which the bulge experienced a different enrichment history than the local disk.

We thank the anonymous referee for a careful reading of the manuscript and helpful comments that lead to improvement of the manuscript. This research has made use of NASA’s Astrophysics Data System Bibliographic Services. This publication makes use of data products from the Two Micron All Sky Survey, which is a joint project of the University of Massachusetts and the Infrared Processing and Analysis Center/California Institute of Technology, funded by the National Aeronautics and Space Administration and the National Science Foundation. CIJ gratefully acknowledges support from the Clay Fellowship, administered by the Smithsonian Astrophysical Observatory. RMR acknowledges support from NSF-AST-1212095. AK acknowledges the Deutsche Forschungsgemeinschaft for funding from Emmy-Noether grant Ko 4161/1.

#### REFERENCES

- Alves-Brito, A., Barbuy, B., Zoccali, M., et al. 2006, *A&A*, 460, 269
- Alves-Brito, A., Meléndez, J., Asplund, M., Ramírez, I., & Yong, D. 2010, *A&A*, 513, A35
- Asplund, M., Grevesse, N., Sauval, A. J., & Scott, P. 2009, *ARA&A*, 47, 481
- Babusiaux, C., Gómez, A., Hill, V., et al. 2010, *A&A*, 519, A77
- Babusiaux, C., Katz, D., Hill, V., et al. 2014, *A&A*, 563, A15
- Ballero, S. K., Matteucci, F., Origlia, L., & Rich, R. M. 2007, *A&A*, 467, 123
- Barbuy, B., Renzini, A., Ortolani, S., Bica, E., & Guarnieri, M. D. 1999, *A&A*, 341, 539
- Barbuy, B., Hill, V., Zoccali, M., et al. 2013, *A&A*, 559, A5
- Bensby, T., Feltzing, S., & Lundström, I. 2003, *A&A*, 410, 527
- Bensby, T., Feltzing, S., Lundström, I., & Ilyin, I. 2005, *A&A*, 433, 185
- Bensby, T., Feltzing, S., Johnson, J. A., et al. 2010a, *A&A*, 512, A41
- Bensby, T., Alves-Brito, A., Oey, M. S., Yong, D., & Meléndez, J. 2010b, *A&A*, 516, L13
- Bensby, T., Adén, D., Meléndez, J., et al. 2011, *A&A*, 533, A134

- Bensby, T., Yee, J. C., Feltzing, S., et al. 2013, *A&A*, 549, A147
- Bergemann, M., Lind, K., Collet, R., Magic, Z., & Asplund, M. 2012, *MNRAS*, 427, 27
- Carretta, E., Bragaglia, A., Gratton, R., & Lucatello, S. 2009, *A&A*, 505, 139
- Castelli, F., & Kurucz, R. L. 2004, arXiv:astro-ph/0405087
- Cescutti, G., Matteucci, F., McWilliam, A., & Chiappini, C. 2009, *A&A*, 505, 605
- Clarkson, W., Sahu, K., Anderson, J., et al. 2008, *ApJ*, 684, 1110
- Clarkson, W. I., Sahu, K. C., Anderson, J., et al. 2011, *ApJ*, 735, 37
- Coelho, P., Barbuy, B., Perrin, M.-N., et al. 2001, *A&A*, 376, 136
- Cohen, J. G., Gratton, R. G., Behr, B. B., & Carretta, E. 1999, *ApJ*, 523, 739
- Cohen, J. G., Huang, W., Udalski, A., Gould, A., & Johnson, J. A. 2008, *ApJ*, 682, 1029
- Cohen, J. G., Thompson, I. B., Sumi, T., et al. 2009, *ApJ*, 699, 66
- Cordero, M. J., Pilachowski, C. A., Johnson, C. I., et al. 2014, *ApJ*, 780, 94
- Cunha, K., Smith, V. V., Suntzeff, N. B., et al. 2002, *AJ*, 124, 379
- Cunha, K., & Smith, V. V. 2006, *ApJ*, 651, 491
- Cunha, K., Smith, V. V., & Gibson, B. K. 2008, *ApJ*, 679, L17
- Decressin, T., Meynet, G., Charbonnel, C., Prantzos, N., & Ekström, S. 2007, *A&A*, 464, 1029
- de Mink, S. E., Pols, O. R., Langer, N., & Izzard, R. G. 2009, *A&A*, 507, L1
- Dotter, A., Chaboyer, B., Jevremović, D., et al. 2008, *ApJS*, 178, 89
- Epstein, C. R., Johnson, J. A., Dong, S., et al. 2010, *ApJ*, 709, 447
- Ferraro, F. R., Dalessandro, E., Mucciarelli, A., et al. 2009, *Nature*, 462, 483
- Freeman, K., Ness, M., Wylie-de-Boer, E., et al. 2013, *MNRAS*, 428, 3660
- Fulbright, J. P., McWilliam, A., & Rich, R. M. 2006, *ApJ*, 636, 821
- Fulbright, J. P., McWilliam, A., & Rich, R. M. 2007, *ApJ*, 661, 1152
- García Pérez, A. E., Cunha, K., Shetrone, M., et al. 2013, *ApJ*, 767, L9
- Gonzalez, O. A., Rejkuba, M., Zoccali, M., et al. 2011, *A&A*, 530, A54
- Gratton, R. G., Carretta, E., Eriksson, K., & Gustafsson, B. 1999, *A&A*, 350, 955
- Gratton, R., Sneden, C., & Carretta, E. 2004, *ARA&A*, 42, 385
- Gratton, R. G., Carretta, E., & Bragaglia, A. 2012, *A&A Rev.*, 20, 50
- Hill, V., Lecureur, A., Gómez, A., et al. 2011, *A&A*, 534, A80
- Hinkle, K., Wallace, L., Valenti, J., & Harmer, D. 2000, *Visible and Near Infrared Atlas of the Arcturus Spectrum 3727-9300 Å* ed. Kenneth Hinkle, Lloyd Wallace, Jeff Valenti, and Dianne Harmer. (San Francisco: ASP) ISBN: 1-58381-037-4, 2000
- Howard, C. D., Rich, R. M., Reitzel, D. B., et al. 2008, *ApJ*, 688, 1060
- Howard, C. D., Rich, R. M., Clarkson, W., et al. 2009, *ApJ*, 702, L153
- Jönsson, H., Ryde, N., Harper, G. M., et al. 2014, arXiv:1403.2594
- Johnson, J. A., Gal-Yam, A., Leonard, D. C., et al. 2007, *ApJ*, 655, L33
- Johnson, J. A., Gaudi, B. S., Sumi, T., Bond, I. A., & Gould, A. 2008, *ApJ*, 685, 508
- Johnson, C. I., Rich, R. M., Fulbright, J. P., Valenti, E., & McWilliam, A. 2011, *ApJ*, 732, 108
- Johnson, C. I., Rich, R. M., Kobayashi, C., & Fulbright, J. P. 2012, *ApJ*, 749, 175
- Johnson, C. I., Rich, R. M., Kobayashi, C., et al. 2013a, *ApJ*, 765, 157
- Johnson, C. I., McWilliam, A., & Rich, R. M. 2013b, *ApJ*, 775, L27
- Karakas, A. I. 2010, *MNRAS*, 403, 1413
- Kobayashi, C., Umeda, H., Nomoto, K., Tominaga, N., & Ohkubo, T. 2006, *ApJ*, 653, 1145
- Kobayashi, C., Karakas, A. I., & Umeda, H. 2011, *MNRAS*, 414, 3231
- Kormendy, J., & Kennicutt, R. C., Jr. 2004, *ARA&A*, 42, 603
- Kroupa, P. 2008, *Pathways Through an Eclectic Universe*, 390, 3
- Kunder, A., Koch, A., Rich, R. M., et al. 2012, *AJ*, 143, 57
- Kurtz, M. J., & Mink, D. J. 1998, *PASP*, 110, 934
- Kurucz, R. L. 1994, *Atomic Data for Opacity Calculations*, Kurucz CD-ROM No. 1
- Lecureur, A., Hill, V., Zoccali, M., et al. 2007, *A&A*, 465, 799
- Li, Z.-Y., Shen, J., Rich, R. M., Kunder, A., & Mao, S. 2014, arXiv:1401.2996
- Lind, K., Asplund, M., Barklem, P. S., & Belyaev, A. K. 2011, *A&A*, 528, A103
- Lind, K., Bergemann, M., & Asplund, M. 2012, *MNRAS*, 427, 50
- Majewski, S. R., Wilson, J. C., Hearty, F., Schiavon, R. R., & Skrutskie, M. F. 2010, *IAU Symposium*, 265, 480
- Martinez-Valpuesta, I., & Gerhard, O. 2013, *ApJ*, 766, L3
- Matteucci, F., Raiteri, C. M., Busson, M., Gallino, R., & Gratton, R. 1993, *A&A*, 272, 421
- McWilliam, A., & Rich, R. M. 1994, *ApJS*, 91, 749
- McWilliam, A., Matteucci, F., Ballero, S., et al. 2008, *AJ*, 136, 367
- McWilliam, A., & Zoccali, M. 2010, *ApJ*, 724, 1491
- McWilliam, A., Fulbright, J., & Rich, R. M. 2010, *IAU Symposium*, 265, 279
- McWilliam, A., Wallerstein, G., & Mottini, M. 2013, *ApJ*, 778, 149
- Meléndez, J., Barbuy, B., Bica, E., et al. 2003, *A&A*, 411, 417
- Meléndez, J., Asplund, M., Alves-Brito, A., et al. 2008, *A&A*, 484, L21
- Mishenina, T. V., Kovtyukh, V. V., Soubiran, C., Travaglio, C., & Busso, M. 2002, *A&A*, 396, 189
- Nataf, D. M., Udalski, A., Gould, A., Fouqué, P., & Stanek, K. Z. 2010, *ApJ*, 721, L28
- Nataf, D. M., Cassisi, S., & Athanassoula, E. 2014, *MNRAS*, 442, 2075
- Ness, M., Freeman, K., Athanassoula, E., et al. 2012, *ApJ*, 756, 22
- Ness, M., Freeman, K., Athanassoula, E., et al. 2013a, *MNRAS*, 430, 836
- Ness, M., Freeman, K., Athanassoula, E., et al. 2013b, *MNRAS*, 432, 2092
- Ness, M., Debattista, V. P., Bensby, T., et al. 2014, *ApJ*, 787, L19
- Nidever, D. L., Zasowski, G., Majewski, S. R., et al. 2012, *ApJ*, 755, L25
- Nomoto, K., Iwamoto, K., Nakasato, N., et al. 1997, *Nuclear Physics A*, 621, 467
- Nomoto, K., Kobayashi, C., & Tominaga, N. 2013, *ARA&A*, 51, 457
- O'Connell, J. E., Johnson, C. I., Pilachowski, C. A., & Burks, G. 2011, *PASP*, 123, 1139
- Origlia, L., Rich, R. M., & Castro, S. 2002, *AJ*, 123, 1559
- Origlia, L., Rich, R. M., Ferraro, F. R., et al. 2011, *ApJ*, 726, L20
- Origlia, L., Massari, D., Rich, R. M., et al. 2013, *ApJ*, 779, L5
- Ortolani, S., Renzini, A., Gilmozzi, R., et al. 1995, *Nature*, 377, 701
- Ramírez, S. V., Stephens, A. W., Frogel, J. A., & DePoy, D. L. 2000, *AJ*, 120, 833
- Ramírez, I., & Allende Prieto, C. 2011, *ApJ*, 743, 135
- Rangwala, N., Williams, T. B., & Stanek, K. Z. 2009a, *ApJ*, 691, 1387
- Rangwala, N., & Williams, T. B. 2009b, *ApJ*, 702, 414
- Reddy, B. E., Lambert, D. L., & Allende Prieto, C. 2006, *MNRAS*, 367, 1329
- Rich, R. M., & Origlia, L. 2005, *ApJ*, 634, 1293
- Rich, R. M., Reitzel, D. B., Howard, C. D., & Zhao, H. 2007a, *ApJ*, 658, L29
- Rich, R. M., Origlia, L., & Valenti, E. 2007b, *ApJ*, 665, L119
- Rich, R. M., Origlia, L., & Valenti, E. 2012, *ApJ*, 746, 59
- Ryde, N., Gustafsson, B., Edvardsson, B., et al. 2010, *A&A*, 509, A20
- Saito, R. K., Zoccali, M., McWilliam, A., et al. 2011, *AJ*, 142, 76
- Saha, K., Martinez-Valpuesta, I., & Gerhard, O. 2012, *MNRAS*, 421, 333
- Shen, J., Rich, R. M., Kormendy, J., et al. 2010, *ApJ*, 720, L72
- Skrutskie, M. F., Cutri, R. M., Stiening, R., et al. 2006, *AJ*, 131, 1163
- Sneden, C. 1973, *ApJ*, 184, 839
- Sneden, C., Gratton, R. G., & Crocker, D. A. 1991, *A&A*, 246, 354
- Soto, M., Rich, R. M., & Kuijken, K. 2007, *ApJ*, 665, L31
- Uttenhaler, S., Schultheis, M., Nataf, D. M., et al. 2012, *A&A*, 546, A57



- Valenti, E., Zoccali, M., Renzini, A., et al. 2013, *A&A*, 559, A98  
Venn, K. A., Irwin, M., Shetrone, M. D., et al. 2004, *AJ*, 128, 1177  
Ventura, P., & D'Antona, F. 2009, *A&A*, 499, 835  
Woosley, S. E., & Weaver, T. A. 1995, *ApJS*, 101, 181  
Zoccali, M., Renzini, A., Ortolani, S., et al. 2003, *A&A*, 399, 931  
Zoccali, M., Lecureur, A., Barbuy, B., et al. 2006, *A&A*, 457, L1  
Zoccali, M., Hill, V., Lecureur, A., et al. 2008, *A&A*, 486, 177  
Zoccali, M., Gonzalez, O. A., Vasquez, S., et al. 2014, *A&A*, 562, A66

TABLE 1  
 STAR IDENTIFICATIONS, COORDINATES, MODEL ATMOSPHERE PARAMETERS,  
 AND RADIAL VELOCITIES

ID <sup>a</sup>	2MASS	RA (J2000) (degrees)	DEC (J2000) (degrees)	V (mag.)	V-I (mag.)	J (mag.)	H (mag.)	K <sub>S</sub> (mag.)	T <sub>eff</sub> (K)	log(g) (cgs)	[Fe/H]	vt (km s <sup>-1</sup> )	RV <sub>helio.</sub> (km s <sup>-1</sup> )	RV <sub>error</sub> <sup>b</sup> (km s <sup>-1</sup> )
(l,b)=(+5.25,-3.02)														
119799C4	18081026-2547354	272.042708	-25.793167	...	...	12.856	11.986	11.704	4400	2.05	-0.39	1.90	+57.96	0.11
129499C4	18081617-2543192	272.067375	-25.721972	...	...	12.596	11.836	11.608	4900	2.75	+0.13	2.10	+27.10	0.04
176772C5	18080936-2556168	272.039417	-25.938028	...	...	11.710	10.794	10.483	4225	2.15	+0.06	1.90	+37.82	0.08
181349C5	18080465-2554356	272.019292	-25.909917	...	...	12.924	12.253	11.906	4775	2.75	+0.26	2.10	+38.51	0.04
183783C5	18080912-2553420	272.037958	-25.895028	...	...	12.876	12.119	11.848	4700	2.75	+0.10	1.75	-97.45	0.01
184088C5	18080726-2553356	272.030250	-25.893222	...	...	12.789	11.869	11.640	4500	2.50	-0.47	1.80	+173.45	0.22
184618C5	18080414-2553236	272.017208	-25.889917	...	...	12.732	11.946	11.690	4600	2.15	-0.59	1.55	+247.54	0.34
185169C5	18080523-2553111	272.021708	-25.886389	...	...	12.367	11.587	11.360	4775	2.50	-0.32	1.85	+84.03	0.25
185357C5	18081778-2553068	272.074083	-25.885250	...	...	12.933	12.152	11.841	4550	2.60	+0.28	1.90	-60.42	0.16
185541C5	18080978-2553024	272.040708	-25.884000	...	...	12.865	12.106	11.865	4750	3.10	+0.34	1.80	-12.63	0.02
187067C5	...	272.056958	-25.874083	...	...	...	...	...	4850	2.30	-0.95	1.35	+115.30	0.31
193190C5	18081265-2550046	272.052625	-25.834556	...	...	12.248	11.461	11.172	4675	2.75	+0.24	1.85	+7.60	0.34
197366C5	18081403-2548290	272.058417	-25.808028	...	...	12.767	11.959	11.700	4550	2.90	+0.32	1.75	-73.59	0.03
215681C6	18084446-2557568	272.185292	-25.965778	...	...	12.938	12.160	11.944	4800	2.75	+0.31	1.95	+54.15	0.20
216922C6	18084514-2557293	272.188083	-25.958139	...	...	12.598	11.652	11.472	4400	2.10	-0.20	2.20	-135.08	0.16
218198C6	18082120-2557000	272.088333	-25.950028	...	...	12.506	11.579	11.271	4225	1.95	-0.32	2.10	-158.44	0.02
219909C6	18083262-2556215	272.135917	-25.939306	...	...	12.618	11.745	11.520	4650	2.25	-0.73	1.75	-62.33	0.02
221537C6	18085002-2555460	272.208375	-25.929417	...	...	12.881	12.057	11.835	4750	2.75	+0.29	1.60	-60.86	0.04
223113C6	18084072-2555101	272.169667	-25.919472	...	...	12.833	12.074	11.845	4800	2.55	-0.15	1.75	-25.52	0.32
223343C6	18082127-2555048	272.088625	-25.918028	...	...	12.834	12.008	11.774	4525	2.65	+0.15	1.45	+61.02	0.44
223621C6	18085263-2554587	272.219208	-25.916306	...	...	12.677	11.938	11.749	5150	3.75	+0.31	1.35	+88.54	0.18
223722C6	...	272.183958	-25.915722	...	...	...	...	...	4525	1.35	-0.75	1.75	-114.88	0.18
224206C6	18084690-2554462	272.195417	-25.912833	...	...	12.857	12.069	11.853	4800	3.00	+0.46	1.65	-142.44	0.13
224866C6	18083392-2554311	272.141417	-25.908667	...	...	12.489	11.604	11.333	4350	2.10	-0.22	1.75	-96.89	0.01
224951C6	18085128-2554294	272.213667	-25.908167	...	...	12.660	11.877	11.583	4650	2.75	+0.17	1.80	-87.33	0.32
225531C6	18082878-2554167	272.119958	-25.904639	...	...	12.613	11.670	11.452	4425	1.75	-0.73	1.80	+135.60	0.20
226450C6	18083464-2553563	272.144333	-25.898972	...	...	12.918	12.061	11.862	4500	2.50	+0.27	1.80	-22.47	0.13
226850C6	18082340-2553475	272.097542	-25.896500	...	...	12.548	11.753	11.506	4800	2.15	-0.85	1.85	+21.21	0.03
227867C6	18084160-2553245	272.173333	-25.890167	...	...	12.699	11.894	11.634	4850	3.15	+0.09	1.60	+62.08	0.14
228466C6	18082917-2553116	272.121542	-25.886583	...	...	12.665	11.762	11.548	4700	1.55	-0.98	2.15	+24.42	0.12
229507C6	18085530-2552488	272.230375	-25.880222	...	...	12.490	11.622	11.408	4650	1.75	-0.29	1.60	+71.66	0.13
230424C6	18085024-2552281	272.209292	-25.874500	...	...	12.319	11.344	11.098	4400	2.10	-0.84	1.75	-0.90	0.06
230483C6	18082585-2552269	272.107708	-25.874139	...	...	12.643	11.725	11.465	4450	2.10	-0.65	1.60	-19.64	0.09
231379C6	18082290-2552064	272.095417	-25.868444	...	...	12.787	11.906	11.675	4500	2.30	-0.30	1.80	+36.71	0.36
231618C6	18084424-2552014	272.184250	-25.867028	...	...	12.540	11.776	12.711	4550	2.60	+0.04	1.65	+22.46	0.10
232493C6	...	272.090500	-25.861694	...	...	...	...	...	4625	2.00	-1.14	1.20	+160.24	0.05
233121C6	18083049-2551279	272.127000	-25.857722	...	...	12.614	11.684	11.468	4500	1.90	-0.50	1.90	-21.69	0.12
233560C6	18082099-2551174	272.087417	-25.854833	...	...	12.900	11.970	11.747	4375	2.10	-0.21	1.85	+170.65	0.27
233708C6	18084123-2551146	272.171750	-25.853972	...	...	12.393	11.437	11.064	4500	2.50	+0.14	1.70	+57.52	0.07
240059C6	18083133-2548449	272.130542	-25.812472	...	...	12.410	11.452	11.258	4400	1.65	-0.69	1.60	-124.52	0.52
240083C6	18082459-2548444	272.102500	-25.812306	...	...	12.255	11.395	11.130	4425	1.65	-0.58	1.70	-33.61	0.10
259050C7	18091376-2557523	272.307250	-25.964528	...	...	12.231	11.277	11.012	4275	1.55	-0.65	1.65	-124.20	0.16
259377C7	18085927-2557448	272.246958	-25.962472	...	...	12.735	11.939	11.723	5000	3.25	+0.29	1.85	+25.50	0.18
260308C7	18090858-2557243	272.285792	-25.956750	...	...	12.659	11.825	11.611	4600	2.50	+0.16	1.90	-43.66	0.10
262018C7	18091405-2556473	272.308583	-25.946472	...	...	12.937	12.109	11.925	4700	2.75	+0.08	2.00	-16.13	0.31
266442C7	18090118-2555154	272.254917	-25.920917	...	...	12.855	11.908	11.678	4350	2.00	-0.42	1.60	-62.73	0.02
270316C7	18091628-2553550	272.317917	-25.898667	...	...	12.675	11.766	11.538	4400	1.90	-0.37	1.65	-1.74	0.47
275181C7	18091022-2552134	272.292583	-25.870389	...	...	12.478	11.578	11.366	4375	1.70	-0.59	1.75	+253.05	0.05
277490C7	18090629-2551235	272.276208	-25.856500	...	...	12.814	11.861	11.606	4250	1.55	-0.56	1.65	+76.93	0.38
278419C7	18085959-2551037	272.248292	-25.850972	...	...	12.777	12.019	11.714	4725	2.75	+0.20	1.55	-68.67	0.05
282804C7	18091653-2549261	272.318917	-25.823889	...	...	12.468	11.614	11.351	4575	2.50	+0.10	1.70	+135.83	0.04
286252C7	18090052-2548070	272.252167	-25.801861	...	...	12.579	11.777	11.563	4700	3.10	+0.43	1.40	-76.01	0.06
45512C2	18090473-2545129	272.269792	-25.753556	...	...	12.623	11.821	11.552	4500	2.15	-0.27	1.75	+96.20	0.03

TABLE 1 — *Continued*

ID <sup>a</sup>	2MASS	RA (J2000) (degrees)	DEC (J2000) (degrees)	V (mag.)	V-I (mag.)	J (mag.)	H (mag.)	K <sub>S</sub> (mag.)	T <sub>eff</sub> (K)	log(g) (cgs)	[Fe/H]	vt (km s <sup>-1</sup> )	RV <sub>helio.</sub> (km s <sup>-1</sup> )	RV <sub>error</sub> <sup>b</sup> (km s <sup>-1</sup> )	
47188C2	18090688-2544307	272.278667	-25.741833	...	...	12.258	11.324	11.057	4350	1.70	-0.52	1.85	-128.90	0.34	
77186C3	18082835-2547382	272.118125	-25.793889	...	...	12.942	12.153	11.890	4750	3.15	+0.41	1.85	-5.75	0.10	
77707C3	18083637-2547256	272.151542	-25.790306	...	...	12.479	11.623	11.448	4825	3.15	+0.44	1.65	+4.81	0.14	
80582C3	18085189-2546213	272.216208	-25.772556	...	...	12.765	11.945	11.686	5100	3.55	+0.07	1.60	-39.87	0.37	
81644C3	18085454-2545569	272.227208	-25.765806	...	...	12.631	11.753	11.430	4600	2.85	+0.21	1.70	+52.17	0.11	
82227C3	18084141-2545439	272.172500	-25.762139	...	...	12.676	11.828	11.642	4900	3.25	+0.25	1.65	-14.02	0.18	
83531C3	18084381-2545145	272.182500	-25.754000	...	...	12.535	11.692	11.431	4725	3.25	+0.45	1.80	-26.11	0.22	
84255C3	18082150-2544574	272.089583	-25.749278	...	...	12.583	11.668	11.423	4350	1.50	-0.68	1.45	-221.43	0.03	
86757C3	18083011-2544007	272.125458	-25.733500	...	...	12.467	11.541	11.300	4400	2.20	-0.02	1.90	+72.12	0.01	
88522C3	18083582-2543214	272.149250	-25.722611	...	...	12.463	11.613	11.383	4700	3.00	+0.39	1.90	-5.87	0.23	
NGC 6553															
225847C6	18085574-2554094	272.232292	-25.902583	...	...	12.895	12.000	11.757	4500	2.25	-0.11	1.45	-3.26	0.24	
227379C6	18082809-2553354	272.117083	-25.893167	...	...	12.947	12.011	11.779	4350	2.25	-0.05	1.55	-2.50	0.13	
228407C6	18085354-2553128	272.223042	-25.886889	...	...	12.718	11.781	11.547	4415	1.95	-0.22	1.75	+0.21	0.16	
230208C6	18085430-2552332	272.226208	-25.875917	...	...	12.846	12.020	11.842	4900	3.05	+0.00	1.40	+1.43	0.46	
239284C6	18083226-2549034	272.134417	-25.817611	...	...	12.438	11.512	11.232	4300	2.00	-0.14	1.80	-9.48	0.43	
265795C7	18092018-25525283	272.334125	-25.924556	...	...	12.757	11.959	11.788	4600	2.50	-0.07	1.55	-12.45	0.03	
268360C7	18091379-2554357	272.308000	-25.909833	...	...	12.075	11.278	10.987	4750	3.15	-0.08	1.35	+3.63	0.71	
268493C7	18090837-2554327	272.284917	-25.909056	...	...	12.647	11.734	11.552	4500	2.30	-0.20	1.90	-1.86	0.11	
271021C7	18090661-2553404	272.277667	-25.894472	...	...	12.544	11.775	11.591	4750	2.50	-0.06	1.65	+0.22	0.06	
271400C7	18091320-2553328	272.305083	-25.892389	...	...	12.418	11.519	11.325	4525	2.50	-0.19	1.90	-4.03	0.22	
77182C3	18084966-2547388	272.206875	-25.794056	...	...	12.806	11.927	11.670	4700	2.50	-0.09	1.75	+3.44	0.17	
85597C3	18082369-2544268	272.098708	-25.740778	...	...	12.723	11.896	11.655	4400	2.25	-0.15	1.55	+0.24	0.17	
(l,b)=(0,-12)															
1156C2	18355601-3433364	278.983417	-34.560111	15.93	1.534	13.092	12.380	12.280	4300	1.80	-0.46	1.45	+72.84	0.01	
1407C3	18345053-3433226	278.710542	-34.556306	15.76	1.155	13.490	13.008	12.995	5125	2.40	-0.62	1.45	-141.73	0.09	
1491C7	18353352-3449238	278.889708	-34.823306	15.80	1.419	13.184	12.562	12.461	4700	2.25	-0.32	1.85	-31.46	0.62	
1554C7	18354037-3449160	278.918208	-34.821139	15.11	1.166	12.887	12.390	12.333	5050	2.20	-0.67	1.50	+7.77	0.18	
166C3	18344539-3436070	278.689125	-34.602000	15.90	1.267	13.466	12.945	12.873	4850	2.20	-0.83	1.30	+54.10	0.12	
1754C3	18344892-3432327	278.703833	-34.542417	15.43	1.301	12.955	12.409	12.298	4900	2.50	-0.25	1.65	+18.44	0.06	
1814C1	18361156-3432060	279.048250	-34.535000	15.85	1.427	13.229	12.567	12.421	4650	2.60	-0.30	1.50	+57.13	0.01	
1876C2	18354937-3431562	278.955750	-34.532250	15.86	1.106	13.679	13.187	13.147	5000	2.50	-1.03	1.10	+202.57	0.03	
1917C1	18361248-3431515	279.052083	-34.530972	16.22	1.426	13.562	12.975	12.850	4675	2.70	+0.18	1.50	-53.87	0.01	
1918C1	18360752-3431511	279.031375	-34.530833	15.83	1.248	13.428	12.875	12.791	4900	2.35	-0.44	1.60	+42.10	0.05	
201583C3	18345139-3431404	278.714125	-34.527889	15.79	1.258	13.411	12.848	12.813	4800	1.90	-1.11	0.90	+59.07	0.08	
2110C7	18353609-3447564	278.900417	-34.799056	15.59	1.405	13.013	12.367	12.338	4675	3.00	+0.02	1.30	-6.53	0.10	
2178C7	18354156-3447486	278.923167	-34.796889	15.77	1.371	13.195	12.619	12.505	4700	2.80	+0.00	1.80	-12.34	0.10	
2200C3	18345778-3431359	278.740708	-34.526639	16.15	1.315	13.588	13.073	13.014	4975	2.70	-0.10	1.80	-6.43	0.11	
2220C7	18353072-3447426	278.878000	-34.795194	15.62	1.233	13.230	12.739	12.685	5150	2.75	-0.17	1.60	-81.33	0.06	
222C3	18351488-3436002	278.812083	-34.600111	15.50	1.295	12.984	12.449	12.329	4950	2.60	-0.43	1.90	+90.22	0.53	
2335C2	18355884-3430461	278.995208	-34.512778	15.81	1.270	13.385	12.778	12.718	4750	2.05	-0.90	1.50	-119.07	0.12	
2407C2	18360198-3430369	279.008292	-34.510222	15.49	1.173	13.232	12.653	12.605	4975	2.30	-0.64	1.70	-145.30	0.15	
2422C7	18354805-3447154	278.950250	-34.787667	15.89	1.481	13.176	12.551	12.476	4400	2.15	+0.17	1.90	-21.36	0.07	
2470C3	18352151-3431018	278.839667	-34.517167	16.25	1.375	13.661	13.048	12.952	4800	3.10	+0.00	1.35	+89.04	0.18	
2502C3	18345442-3430566	278.726750	-34.515694	15.97	1.330	13.424	12.833	12.762	4750	2.25	-0.62	1.40	+255.23	0.44	
2532C6	18351318-3446482	278.804917	-34.780139	15.71	1.345	13.123	12.610	12.467	4750	2.50	-0.17	1.90	-42.27	0.16	
2580C6	18351524-3446412	278.813500	-34.778167	16.06	1.566	13.184	12.595	12.406	4575	2.85	+0.30	2.00	-16.54	0.24	
2769C3	18345752-3430213	278.739667	-34.505917	15.78	1.295	13.311	12.797	12.657	4900	3.15	+0.06	1.25	-51.43	0.48	
2772C7	18354807-3446257	278.950292	-34.773833	15.10	1.258	12.692	12.137	12.072	4900	2.75	-0.25	1.65	-79.69	0.09	
2812C8	18360927-3446233	279.038667	-34.773194	15.63	1.458	12.948	12.274	12.101	4475	2.00	-0.65	1.55	+90.18	0.36	
2947C3	18350059-3429557	278.752458	-34.498778	16.02	1.204	13.660	13.157	13.120	5150	2.60	-0.50	1.95	-98.82	0.15	
2948C7	18352452-3446010	278.852208	-34.767000	15.53	1.679	12.485	11.838	11.684	4275	2.00	+0.12	1.65	-22.63	0.13	
3018C3	18350358-3429453	278.764958	-34.495889	15.49	1.404	12.836	12.190	12.033	4650	2.40	-0.54	1.45	-64.70	0.13	
3035C7	18355135-3445453	278.964000	-34.762639	15.68	1.191	13.412	12.868	12.808	5050	2.50	-0.44	1.45	+8.23	0.07	
3091C8	18360886-3445437	279.036958	-34.762167	15.32	1.236	12.938	12.390	12.306	4900	3.00	-0.50	1.45	+76.91	0.13	
3101C7	18353713-3445344	278.904708	-34.759611	15.86	1.233	13.523	12.939	12.880	4950	2.65	-0.40	1.70	+67.03	0.02	

ID <sup>a</sup>	2MASS	RA (J2000) (degrees)	DEC (J2000) (degrees)	V (mag.)	V-I (mag.)	J (mag.)	H (mag.)	K <sub>S</sub> (mag.)	T <sub>eff</sub> (K)	log(g) (cgs)	[Fe/H]	vt (km s <sup>-1</sup> )	RV <sub>helio.</sub> (km s <sup>-1</sup> )	RV <sub>error</sub> <sup>b</sup> (km s <sup>-1</sup> )
3142C3	18350948–3429282	278.789500	–34.491139	15.95	1.287	13.481	12.949	12.831	4900	2.65	–0.22	1.75	–18.58	0.02
3161C3	18351942–3429266	278.830917	–34.490722	15.46	1.306	12.968	12.367	12.313	5100	3.20	–0.15	1.70	–29.96	0.08
3191C7	18355560–3445217	278.981708	–34.756083	15.40	1.243	13.051	12.479	12.431	4950	2.50	–0.37	1.60	+64.72	0.09
3201C6	18350301–3445053	278.762583	–34.751528	15.47	1.211	13.078	12.624	12.467	5200	3.50	+0.04	1.35	–71.88	0.11
3238C6	18351698–3444595	278.820792	–34.749889	15.73	1.322	13.174	12.632	12.523	4900	3.00	–0.22	1.35	–65.42	0.19
3267C3	18352206–3429112	278.841917	–34.486444	15.07	1.349	12.525	11.923	11.806	4700	2.65	+0.04	1.40	–119.57	0.22
3515C3	18345072–3428380	278.711000	–34.477200	...	...	12.658	12.099	11.965	4750	2.70	+0.01	1.80	–14.32	0.08
3558C6	18351293–3444170	278.803875	–34.738139	16.03	1.341	13.526	12.901	12.780	4800	2.75	–0.15	1.75	+21.61	0.25
3690C7	18352834–3444085	278.868125	–34.735750	14.97	1.208	12.606	12.088	12.009	4800	1.45	–1.46	1.50	+40.71	0.07
3711C7	18354105–3444059	278.921042	–34.735028	15.71	1.097	13.526	13.038	13.004	5350	3.70	–0.49	1.25	+3.48	0.21
3733C3	18351799–3428093	278.824958	–34.469250	15.10	1.423	12.436	11.795	11.722	4750	2.60	–0.18	1.70	–45.51	0.01
3796C6	18345825–3443440	278.742708	–34.728944	15.53	1.454	12.839	12.133	12.041	4500	1.85	–0.82	1.65	–38.50	0.21
3965C6	18345917–3443219	278.746583	–34.722806	15.46	1.663	12.442	11.705	11.570	4400	2.35	–0.08	1.70	–97.46	0.27
4085C3	18351357–3427240	278.806542	–34.456667	16.13	1.513	13.330	12.675	12.564	4550	1.90	–0.58	1.65	–7.91	0.12
4217C6	18345512–3442462	278.729667	–34.712861	15.78	1.461	13.065	12.390	12.213	4500	2.15	–0.57	1.70	–25.21	0.08
4263C6	18350180–3442404	278.757542	–34.711278	15.87	1.329	13.333	12.756	12.650	5000	3.05	–0.34	1.90	–90.50	0.07
431C2	18355359–3435209	278.973333	–34.589194	15.63	1.175	13.302	12.805	12.744	5100	3.85	–0.03	1.20	+32.21	0.07
4365C3	18352116–3426510	278.838208	–34.447500	16.08	1.148	13.854	13.339	13.339	4950	1.75	–0.80	1.65	+202.51	0.25
4478C8	18361669–3442257	279.069583	–34.707167	15.79	1.260	13.441	12.906	12.751	4900	2.25	–0.36	1.65	+61.90	0.17
455C1	18361784–3435209	279.074375	–34.589194	15.67	1.174	13.413	12.878	12.798	5000	2.70	–0.61	1.50	–168.72	0.05
4612C6	18350115–3441540	278.754792	–34.698361	16.02	1.264	13.580	12.968	12.908	4950	2.60	–0.78	1.30	+35.76	0.21
4740C8	18361928–3441470	279.080417	–34.696417	15.80	1.208	13.515	13.011	12.826	5000	2.30	–0.49	1.60	+181.98	0.17
4876C6	18351228–3441180	278.801208	–34.688361	16.08	1.303	13.583	12.978	12.887	4800	2.70	–0.59	1.35	+8.46	0.01
5319C6	18344324–3440187	278.680167	–34.671889	15.58	1.447	12.877	12.249	12.110	4600	2.45	–0.40	1.50	–280.09	0.22
5351C8	18360799–3440158	279.033333	–34.671111	15.83	1.382	13.355	12.641	12.494	4700	2.65	–0.08	1.55	–79.63	0.24
5400C8	18361236–3440076	279.051542	–34.668806	15.96	1.113	13.820	13.357	13.236	5050	3.75	+0.12	1.30	–29.93	0.10
5487C8	18361461–3439566	279.060958	–34.665750	16.16	1.339	13.645	13.067	12.971	4750	2.30	–0.47	1.75	+45.61	0.01
5543C6	18351584–3439495	278.816042	–34.663778	16.07	1.459	13.311	12.694	12.519	4400	1.60	–0.17	2.00	–6.45	0.04
5588C6	18350642–3439420	278.776750	–34.661694	15.87	1.282	13.371	12.812	12.718	4900	2.60	–0.20	1.60	+54.21	0.06
5664C6	18345260–3439317	278.719167	–34.658833	15.43	1.330	12.862	12.341	12.241	4800	2.75	+0.23	1.60	–82.41	0.01
5908C6	18344801–3438540	278.700000	–34.648333	15.66	1.151	13.444	12.982	12.844	5150	2.50	–0.67	1.60	–138.69	0.05
5977C6	18351222–3438453	278.800917	–34.645917	15.31	1.334	12.714	12.125	12.026	4650	2.45	+0.19	1.65	–7.78	0.16
5980C6	18344397–3438441	278.683250	–34.645611	15.93	1.242	13.459	12.912	12.849	4950	3.45	–0.17	1.25	–45.00	0.08
608C1	18361368–3434559	279.057042	–34.582194	15.13	1.133	12.938	12.450	12.348	5000	2.45	–1.74	1.00	+30.98	0.10
6090C6	18352004–3438289	278.833542	–34.641333	16.15	1.479	13.361	12.735	12.575	4500	2.25	–0.02	1.90	+42.30	0.16
6164C6	18345884–3438175	278.745167	–34.638194	15.25	1.265	12.830	12.234	12.183	4900	3.25	–0.13	0.95	–60.24	0.06
6230C5	18343398–3438536	278.641583	–34.648222	15.06	1.154	12.814	12.371	12.284	5050	3.60	+0.20	1.25	–36.65	0.10
6263C6	18351420–3438060	278.809208	–34.635000	16.01	1.648	12.949	12.313	12.147	4250	2.30	+0.48	1.95	–7.85	0.03
6391C8	18362357–3437379	279.098250	–34.627167	15.28	1.140	13.105	12.554	12.534	5000	2.20	–0.63	1.55	–92.33	0.09
6419C5	18343096–3438299	278.629000	–34.641667	15.40	1.390	12.821	12.183	12.082	4700	2.60	–0.24	1.55	–9.31	0.04
6426C8	18361008–3437330	279.042083	–34.625833	15.79	1.280	13.374	12.825	12.667	4950	2.95	–0.40	1.60	+30.84	0.28
6505C6	18351867–3437309	278.827833	–34.625222	16.04	1.232	13.778	13.038	12.999	5000	2.70	–0.38	1.50	–41.77	0.11
650C2	18355679–3434481	278.986667	–34.580083	15.29	1.530	12.462	11.745	11.632	4350	1.55	–0.67	1.60	+45.55	0.06
6549C6	18350342–3437243	278.764292	–34.623417	15.70	1.320	13.270	12.614	12.506	4900	3.35	+0.33	1.30	–44.42	0.03
6637C8	18360757–3437029	279.031583	–34.617472	16.07	1.296	13.599	13.056	12.978	4800	2.50	–0.26	1.60	–32.65	0.20
6717C6	18345238–3437018	278.718292	–34.617167	15.58	1.283	13.127	12.532	12.465	4900	3.30	–0.19	1.20	+132.37	0.03
6828C7	18355625–3436545	278.984375	–34.615111	16.09	1.360	13.467	12.896	12.808	4650	2.50	+0.10	1.70	+2.17	0.02
6913C7	18355267–3436435	278.969458	–34.612028	15.95	1.244	13.520	13.003	12.893	5000	2.75	–0.27	1.70	–4.76	0.07
867C3	18350909–3434346	278.787917	–34.576306	15.76	1.228	13.378	12.839	12.733	5000	2.60	–0.47	1.60	–136.48	0.25

<sup>a</sup> These are the OGLE identification values given in the image headers, and are also listed in Zoccali et al. (2008) and Gonzalez et al. (2011).<sup>b</sup> The radial velocity errors represent the 1 $\sigma$  values from individual exposures of each star over all filters.

TABLE 2  
 LINE LIST

Species	Wavelength (Å)	E.P. (eV)	$\log(\text{gf})^a$	$\log \epsilon(X)_\odot$	$\log \epsilon(X)_{Arc.}$	[X/Fe] or [Fe/H] <sub>Arc.</sub>
[O I]	6300.30	0.00	-9.750	8.69	8.63	+0.44
Na I	6154.23	2.10	-1.560	6.33	5.89	+0.06
Na I	6160.75	2.10	-1.210	6.33	5.89	+0.06
Mg I	6318.71	5.10	-2.010	7.58	7.38	+0.30
Mg I	6319.24	5.10	-2.250	7.58	7.38	+0.30
Mg I	6319.49	5.10	-2.730	7.58	7.38	+0.30
Al I	6696.02	3.14	-1.570	6.47	6.28	+0.31
Al I	6698.67	3.14	-1.890	6.47	6.28	+0.31
Si I	5645.61	4.93	-2.090	7.55	7.38	+0.33
Si I	5654.92	5.61	-1.714	7.55	7.38	+0.33
Si I	5665.56	4.92	-1.910	7.55	7.38	+0.33
Si I	5666.68	5.62	-1.805	7.55	7.38	+0.33
Si I	5690.43	4.93	-1.910	7.55	7.38	+0.33
Si I	5701.10	4.93	-2.080	7.55	7.38	+0.33
Si I	6142.48	5.62	-1.575	7.55	7.38	+0.33
Si I	6145.02	5.62	-1.460	7.55	7.38	+0.33
Si I	6155.13	5.62	-0.774	7.55	7.38	+0.33
Si I	6155.69	5.62	-2.352	7.55	7.38	+0.33
Si I	6195.43	5.87	-1.560	7.55	7.38	+0.33
Si I	6237.32	5.61	-1.115	7.55	7.38	+0.33
Si I	6244.47	5.62	-1.303	7.55	7.38	+0.33
Si I	6721.85	5.86	-1.016	7.55	7.38	+0.33
Ca I	5594.46	2.52	-0.370	6.36	6.07	+0.21
Ca I	5601.28	2.53	-0.463	6.36	6.07	+0.21
Ca I	5715.82	2.71	-3.386	6.36	6.07	+0.21
Ca I	6122.22	1.89	-0.466	6.36	6.07	+0.21
Ca I	6156.02	2.52	-2.637	6.36	6.07	+0.21
Ca I	6161.30	2.52	-1.246	6.36	6.07	+0.21
Ca I	6162.17	1.90	-0.210	6.36	6.07	+0.21
Ca I	6166.44	2.52	-1.262	6.36	6.07	+0.21
Ca I	6169.04	2.52	-0.837	6.36	6.07	+0.21
Ca I	6169.56	2.53	-0.628	6.36	6.07	+0.21
Cr I	5628.64	3.42	-0.832	5.67	5.09	-0.08
Cr I	5642.36	3.86	-0.840	5.67	5.09	-0.08
Cr I	5648.26	3.83	-0.980	5.67	5.09	-0.08
Cr I	5674.17	3.56	-1.507	5.67	5.09	-0.08
Cr I	5712.77	3.01	-1.107	5.67	5.09	-0.08
Cr I	5719.82	3.01	-1.660	5.67	5.09	-0.08
Cr I	5729.21	3.85	-1.038	5.67	5.09	-0.08
Cr I	5783.06	3.32	-0.510	5.67	5.09	-0.08
Cr I	5784.97	3.32	-0.440	5.67	5.09	-0.08
Cr I	5787.92	3.32	-0.183	5.67	5.09	-0.08
Cr I	5788.38	3.01	-1.524	5.67	5.09	-0.08
Cr I	5790.65	1.00	-4.033	5.67	5.09	-0.08
Cr I	6330.09	0.94	-3.000	5.67	5.09	-0.08
Cr I	6630.01	1.03	-3.560	5.67	5.09	-0.08
Cr I	6729.73	4.39	-0.753	5.67	5.09	-0.08
Fe I	5595.06	5.06	-1.490	7.52	7.02	-0.50
Fe I	5607.66	4.15	-2.260	7.52	7.02	-0.50
Fe I	5608.97	4.21	-2.240	7.52	7.02	-0.50
Fe I	5611.36	3.63	-3.010	7.52	7.02	-0.50
Fe I	5614.28	5.09	-1.298	7.52	7.02	-0.50
Fe I	5615.30	2.59	-2.268	7.52	7.02	-0.50
Fe I	5615.64	3.33	-0.170	7.52	7.02	-0.50
Fe I	5618.63	4.21	-1.456	7.52	7.02	-0.50
Fe I	5619.22	3.69	-3.170	7.52	7.02	-0.50
Fe I	5619.60	4.39	-1.420	7.52	7.02	-0.50
Fe I	5622.94	3.64	-2.986	7.52	7.02	-0.50
Fe I	5624.02	4.39	-1.230	7.52	7.02	-0.50
Fe I	5624.54	3.42	-0.440	7.52	7.02	-0.50
Fe I	5627.08	4.18	-2.920	7.52	7.02	-0.50
Fe I	5633.95	4.99	-0.310	7.52	7.02	-0.50
Fe I	5635.82	4.26	-1.640	7.52	7.02	-0.50
Fe I	5636.70	3.64	-2.630	7.52	7.02	-0.50
Fe I	5638.26	4.22	-0.820	7.52	7.02	-0.50
Fe I	5641.43	4.26	-0.890	7.52	7.02	-0.50
Fe I	5646.68	4.26	-2.440	7.52	7.02	-0.50
Fe I	5649.99	5.10	-0.770	7.52	7.02	-0.50
Fe I	5650.71	5.08	-0.810	7.52	7.02	-0.50
Fe I	5651.47	4.47	-1.850	7.52	7.02	-0.50
Fe I	5652.01	4.22	-3.010	7.52	7.02	-0.50
Fe I	5652.32	4.26	-1.870	7.52	7.02	-0.50
Fe I	5653.86	4.39	-1.480	7.52	7.02	-0.50
Fe I	5655.18	5.06	-0.600	7.52	7.02	-0.50

TABLE 2 — *Continued*

Species	Wavelength (Å)	E.P. (eV)	$\log(\text{gf})^a$	$\log \epsilon(X)_\odot$	$\log \epsilon(X)_{Arc.}$	[X/Fe] or [Fe/H] <sub>Arc.</sub>
Fe I	5661.35	4.28	-1.856	7.52	7.02	-0.50
Fe I	5661.97	4.26	-2.770	7.52	7.02	-0.50
Fe I	5662.52	4.18	-0.563	7.52	7.02	-0.50
Fe I	5677.68	4.10	-2.640	7.52	7.02	-0.50
Fe I	5678.60	2.42	-4.770	7.52	7.02	-0.50
Fe I	5679.02	4.65	-0.900	7.52	7.02	-0.50
Fe I	5680.24	4.19	-2.330	7.52	7.02	-0.50
Fe I	5686.53	4.55	-0.626	7.52	7.02	-0.50
Fe I	5691.50	4.30	-1.540	7.52	7.02	-0.50
Fe I	5698.02	3.64	-2.790	7.52	7.02	-0.50
Fe I	5699.41	4.96	-2.044	7.52	7.02	-0.50
Fe I	5701.54	2.56	-2.046	7.52	7.02	-0.50
Fe I	5704.73	5.03	-1.319	7.52	7.02	-0.50
Fe I	5705.46	4.30	-1.565	7.52	7.02	-0.50
Fe I	5707.70	4.10	-3.148	7.52	7.02	-0.50
Fe I	5714.55	5.09	-1.715	7.52	7.02	-0.50
Fe I	5715.47	4.15	-2.990	7.52	7.02	-0.50
Fe I	5717.83	4.28	-1.090	7.52	7.02	-0.50
Fe I	5720.89	4.55	-1.750	7.52	7.02	-0.50
Fe I	5723.67	4.47	-2.250	7.52	7.02	-0.50
Fe I	5724.45	4.28	-2.610	7.52	7.02	-0.50
Fe I	5731.76	4.26	-1.210	7.52	7.02	-0.50
Fe I	5732.30	4.99	-1.440	7.52	7.02	-0.50
Fe I	5734.56	4.96	-1.784	7.52	7.02	-0.50
Fe I	5738.23	4.22	-2.240	7.52	7.02	-0.50
Fe I	5741.85	4.26	-1.744	7.52	7.02	-0.50
Fe I	5750.03	5.01	-2.323	7.52	7.02	-0.50
Fe I	5752.03	4.55	-1.077	7.52	7.02	-0.50
Fe I	5759.26	4.65	-2.040	7.52	7.02	-0.50
Fe I	5759.54	4.30	-2.179	7.52	7.02	-0.50
Fe I	5760.34	3.64	-2.590	7.52	7.02	-0.50
Fe I	5762.99	4.21	-0.460	7.52	7.02	-0.50
Fe I	5767.97	4.29	-3.236	7.52	7.02	-0.50
Fe I	5773.45	3.57	-3.704	7.52	7.02	-0.50
Fe I	5775.08	4.22	-1.238	7.52	7.02	-0.50
Fe I	5778.45	2.59	-3.590	7.52	7.02	-0.50
Fe I	5784.66	3.40	-2.672	7.52	7.02	-0.50
Fe I	5793.91	4.22	-1.750	7.52	7.02	-0.50
Fe I	5809.22	3.88	-1.630	7.52	7.02	-0.50
Fe I	5811.91	4.14	-2.460	7.52	7.02	-0.50
Fe I	5814.81	4.28	-1.910	7.52	7.02	-0.50
Fe I	5816.37	4.55	-0.681	7.52	7.02	-0.50
Fe I	5821.89	4.99	-1.676	7.52	7.02	-0.50
Fe I	5827.88	3.28	-3.260	7.52	7.02	-0.50
Fe I	6120.25	0.92	-6.020	7.52	7.02	-0.50
Fe I	6127.91	4.14	-1.499	7.52	7.02	-0.50
Fe I	6136.61	2.45	-1.480	7.52	7.02	-0.50
Fe I	6136.99	2.20	-2.900	7.52	7.02	-0.50
Fe I	6137.69	2.59	-1.343	7.52	7.02	-0.50
Fe I	6145.41	3.37	-3.770	7.52	7.02	-0.50
Fe I	6151.62	2.18	-3.349	7.52	7.02	-0.50
Fe I	6157.73	4.08	-1.110	7.52	7.02	-0.50
Fe I	6159.37	4.61	-1.850	7.52	7.02	-0.50
Fe I	6165.36	4.14	-1.614	7.52	7.02	-0.50
Fe I	6171.01	4.73	-2.244	7.52	7.02	-0.50
Fe I	6173.33	2.22	-2.870	7.52	7.02	-0.50
Fe I	6180.20	2.73	-2.666	7.52	7.02	-0.50
Fe I	6187.40	2.83	-4.168	7.52	7.02	-0.50
Fe I	6187.99	3.94	-1.740	7.52	7.02	-0.50
Fe I	6191.56	2.43	-1.367	7.52	7.02	-0.50
Fe I	6200.31	2.61	-2.407	7.52	7.02	-0.50
Fe I	6213.43	2.22	-2.542	7.52	7.02	-0.50
Fe I	6219.28	2.20	-2.353	7.52	7.02	-0.50
Fe I	6226.73	3.88	-2.210	7.52	7.02	-0.50
Fe I	6229.23	2.85	-2.955	7.52	7.02	-0.50
Fe I	6232.64	3.65	-1.323	7.52	7.02	-0.50
Fe I	6240.65	2.22	-3.333	7.52	7.02	-0.50
Fe I	6246.32	3.60	-0.953	7.52	7.02	-0.50
Fe I	6252.56	2.40	-1.697	7.52	7.02	-0.50
Fe I	6270.22	2.86	-2.704	7.52	7.02	-0.50
Fe I	6322.69	2.59	-2.376	7.52	7.02	-0.50
Fe I	6330.85	4.73	-1.290	7.52	7.02	-0.50
Fe I	6335.33	2.20	-2.187	7.52	7.02	-0.50
Fe I	6336.82	3.69	-0.966	7.52	7.02	-0.50
Fe I	6380.74	4.19	-1.326	7.52	7.02	-0.50

TABLE 2 — *Continued*

Species	Wavelength (Å)	E.P. (eV)	$\log(gf)^a$	$\log \epsilon(X)_\odot$	$\log \epsilon(X)_{Arc.}$	[X/Fe] or [Fe/H] <sub>Arc.</sub>
Fe I	6392.54	2.28	-4.090	7.52	7.02	-0.50
Fe I	6393.60	2.43	-1.562	7.52	7.02	-0.50
Fe I	6608.02	2.28	-4.070	7.52	7.02	-0.50
Fe I	6609.11	2.56	-2.602	7.52	7.02	-0.50
Fe I	6609.68	0.99	-5.700	7.52	7.02	-0.50
Fe I	6648.08	1.01	-5.824	7.52	7.02	-0.50
Fe I	6699.14	4.59	-2.081	7.52	7.02	-0.50
Fe I	6705.10	4.61	-1.122	7.52	7.02	-0.50
Fe I	6710.32	1.49	-4.890	7.52	7.02	-0.50
Fe I	6713.74	4.79	-1.530	7.52	7.02	-0.50
Fe I	6726.67	4.61	-1.183	7.52	7.02	-0.50
Fe I	6733.15	4.64	-1.550	7.52	7.02	-0.50
Fe I	6737.27	3.27	-4.339	7.52	7.02	-0.50
Fe I	6750.15	2.42	-2.681	7.52	7.02	-0.50
Fe I	6806.84	2.73	-3.180	7.52	7.02	-0.50
Fe I	6810.26	4.61	-1.086	7.52	7.02	-0.50
Fe I	6820.37	4.64	-1.130	7.52	7.02	-0.50
Fe I	6842.69	4.64	-1.270	7.52	7.02	-0.50
Fe I	6843.65	4.55	-0.960	7.52	7.02	-0.50
Fe I	6857.25	4.08	-2.230	7.52	7.02	-0.50
Fe I	6864.31	4.56	-2.410	7.52	7.02	-0.50
Fe II	6149.26	3.89	-2.681	7.52	7.02	-0.50
Fe II	6247.56	3.89	-2.405	7.52	7.02	-0.50
Fe II	6369.46	2.89	-4.141	7.52	7.02	-0.50
Co I	5647.23	2.28	hfs	4.90	4.52	+0.12
Co I	6117.00	1.78	hfs	4.90	4.52	+0.12
Ni I	5593.73	3.90	-0.960	6.25	5.81	+0.06
Ni I	5614.77	4.15	-0.698	6.25	5.81	+0.06
Ni I	5625.31	4.09	-0.750	6.25	5.81	+0.06
Ni I	5628.34	4.09	-1.301	6.25	5.81	+0.06
Ni I	5638.74	3.90	-1.670	6.25	5.81	+0.06
Ni I	5641.88	4.11	-1.080	6.25	5.81	+0.06
Ni I	5643.07	4.17	-1.260	6.25	5.81	+0.06
Ni I	5682.20	4.11	-0.510	6.25	5.81	+0.06
Ni I	5694.98	4.09	-0.760	6.25	5.81	+0.06
Ni I	5748.35	1.68	-3.160	6.25	5.81	+0.06
Ni I	5760.83	4.11	-0.790	6.25	5.81	+0.06
Ni I	5796.08	1.95	-3.752	6.25	5.81	+0.06
Ni I	5805.21	4.17	-0.720	6.25	5.81	+0.06
Ni I	6128.96	1.68	-3.400	6.25	5.81	+0.06
Ni I	6130.13	4.27	-1.040	6.25	5.81	+0.06
Ni I	6175.36	4.09	-0.619	6.25	5.81	+0.06
Ni I	6176.81	4.09	-0.270	6.25	5.81	+0.06
Ni I	6177.24	1.83	-3.550	6.25	5.81	+0.06
Ni I	6186.71	4.11	-0.890	6.25	5.81	+0.06
Ni I	6191.17	1.68	-2.233	6.25	5.81	+0.06
Ni I	6223.98	4.11	-0.960	6.25	5.81	+0.06
Ni I	6322.16	4.15	-1.190	6.25	5.81	+0.06
Ni I	6635.12	4.42	-0.750	6.25	5.81	+0.06
Ni I	6767.77	1.83	-2.100	6.25	5.81	+0.06
Ni I	6772.31	3.66	-1.010	6.25	5.81	+0.06
Ni I	6813.60	5.34	-0.354	6.25	5.81	+0.06
Cu I	5782.11	1.64	hfs	4.04	3.71	+0.17

<sup>a</sup> The “hfs” designation indicates the abundance was calculated taking hyperfine structure into account. See text for details.

TABLE 3  
ABUNDANCE RATIOS

ID	[O/Fe] <sup>a</sup>	[Na/Fe]	[Mg/Fe]	[Al/Fe]	[Si/Fe]	[Ca/Fe]	[Cr/Fe]	[Fe I/H]	[Fe II/H]	[Co/Fe]	[Ni/Fe]	[Cu/Fe]
(l,b)=(+5.25,-3.02)												
119799C4	+0.63	+0.08	+0.29	+0.26	+0.38	+0.17	+0.07	-0.39	-0.38	+0.25	+0.21	+0.26
129499C4	...	+0.25	+0.22	+0.24	+0.04	+0.30	+0.26	+0.13	...	+0.32	+0.06	...
176772C5	+0.12	+0.19	+0.15	+0.08	-0.05	+0.16	+0.05	+0.07	+0.05	+0.07	+0.14	...
181349C5	-0.06	+0.58	+0.15	+0.20	+0.11	+0.08	+0.00	+0.30	+0.21	+0.25	+0.10	...
183783C5	...	+0.32	+0.12	+0.30	-0.11	+0.15	+0.15	+0.10	...	+0.32	+0.08	...
184088C5	+0.74	+0.03	+0.30	+0.37	+0.14	+0.37	+0.09	-0.45	-0.48	+0.37	+0.15	+0.37
184618C5	...	+0.00	+0.63	+0.28	+0.24	+0.31	+0.06	-0.58	-0.59	+0.14	+0.15	+0.28
185169C5	...	+0.22	+0.37	+0.42	+0.12	+0.53	+0.21	-0.32	...	+0.38	+0.07	+0.39
185357C5	-0.05	+0.24	+0.01	+0.06	-0.11	-0.04	-0.09	+0.29	+0.27	+0.04	+0.12	...
185541C5	-0.05	+0.21	-0.01	+0.01	+0.06	-0.06	+0.08	+0.34	+0.33	+0.18	+0.06	...
187067C5	...	-0.35	+0.30	-0.10	+0.19	+0.53	-0.03	-0.95	-0.94	+0.07	+0.07	-0.43
193190C5	...	+0.37	+0.03	+0.08	+0.04	+0.25	+0.16	+0.25	+0.22	+0.22	+0.06	...
197366C5	+0.01	+0.48	-0.08	+0.12	-0.05	+0.13	+0.12	+0.33	+0.31	+0.26	+0.19	...
215681C6	+0.18	+0.33	+0.09	+0.06	-0.02	+0.21	+0.07	+0.31	...	+0.20	+0.05	+0.51
216922C6	+0.43	+0.28	+0.29	+0.34	+0.24	+0.42	+0.25	-0.19	-0.20	+0.24	+0.08	...
218198C6	+0.50	+0.32	+0.31	+0.27	+0.30	+0.32	+0.16	-0.31	-0.33	+0.23	+0.16	...
219909C6	+0.52	-0.20	+0.38	+0.28	+0.25	+0.32	-0.02	-0.73	-0.73	+0.20	+0.04	...
221537C6	-0.35	+0.31	+0.01	+0.09	-0.20	+0.14	+0.12	+0.29	...	+0.08	+0.06	...
223113C6	+0.43	+0.01	+0.29	+0.12	+0.14	+0.25	+0.01	-0.14	-0.15	+0.15	+0.08	...
223343C6	+0.11	+0.00	-0.10	+0.10	+0.12	+0.16	-0.05	+0.15	+0.14	+0.15	+0.10	...
223621C6	...	-0.04	+0.02	+0.09	-0.12	+0.25	+0.07	+0.33	+0.28	+0.34	+0.07	...
223722C6	+0.40	-0.05	+0.44	+0.28	+0.33	+0.43	-0.05	-0.76	-0.74	-0.01	+0.02	...
224206C6	...	+0.10	-0.10	-0.05	-0.03	-0.24	+0.09	+0.46	+0.45	+0.21	+0.11	...
224866C6	+0.29	+0.17	+0.22	+0.31	+0.16	+0.25	-0.03	-0.22	-0.21	+0.17	+0.11	...
224951C6	+0.32	+0.22	+0.07	+0.05	+0.19	+0.14	+0.04	+0.17	...	+0.14	+0.05	...
225531C6	+0.66	+0.20	+0.46	+0.31	+0.35	+0.40	+0.02	-0.72	-0.73	+0.29	+0.10	+0.28
226450C6	-0.16	+0.06	+0.03	+0.03	+0.09	+0.07	-0.13	+0.27	...	+0.08	+0.05	...
226850C6	...	-0.25	+0.35	+0.18	+0.33	+0.35	+0.04	-0.85	-0.84	+0.15	+0.00	-0.18
227867C6	+0.51	-0.08	+0.12	+0.06	+0.11	+0.08	-0.05	+0.11	+0.07	+0.17	+0.14	+0.38
228466C6	+0.55	-0.22	+0.36	+0.34	+0.29	+0.32	+0.31	-0.96	-0.99	+0.18	+0.06	+0.03
229507C6	...	+0.19	+0.15	+0.20	+0.06	+0.26	-0.14	-0.30	-0.28	+0.00	+0.11	+0.15
230424C6	+0.57	-0.19	+0.38	+0.18	+0.28	+0.24	-0.02	-0.83	-0.85	+0.19	+0.13	+0.20
230483C6	+0.62	+0.13	+0.35	+0.42	+0.32	+0.31	+0.22	-0.63	-0.66	+0.33	+0.13	...
231379C6	+0.54	+0.15	+0.39	+0.28	+0.37	+0.32	+0.01	-0.30	-0.29	+0.32	+0.16	+0.45
231618C6	-0.35	-0.07	+0.09	+0.06	+0.12	+0.05	-0.03	+0.04	+0.04	+0.04	+0.11	+0.28
232493C6	+0.68	-0.26	+0.29	+0.14	+0.04	+0.45	-0.31	-1.14	-1.13	-0.03	-0.16	-0.55
233121C6	+0.63	+0.01	+0.31	+0.26	+0.33	+0.29	+0.04	-0.49	-0.50	+0.16	+0.07	...
233560C6	+0.44	-0.05	+0.30	+0.14	+0.34	+0.25	-0.13	-0.20	-0.22	+0.19	+0.16	+0.40
233708C6	-0.13	+0.15	+0.03	-0.01	+0.13	+0.14	-0.11	+0.12	+0.16	+0.09	+0.17	+0.15
240059C6	+0.64	-0.11	+0.45	+0.27	+0.29	+0.45	-0.03	-0.70	-0.68	+0.11	+0.02	...
240083C6	+0.38	-0.08	+0.35	+0.27	+0.24	+0.34	-0.02	-0.59	-0.56	+0.04	+0.00	...
259050C7	+0.44	-0.08	+0.40	+0.22	+0.35	+0.13	-0.04	-0.65	-0.65	+0.04	+0.12	...
259377C7	...	+0.09	-0.03	+0.03	+0.00	+0.08	+0.03	+0.29	...	+0.26	+0.08	+0.78
260308C7	+0.24	+0.69	+0.04	+0.22	+0.02	+0.20	-0.02	+0.15	+0.16	+0.19	+0.16	...
262018C7	+0.34	-0.02	+0.12	+0.00	+0.00	+0.01	-0.02	+0.08	+0.07	+0.15	-0.04	+0.46
266442C7	+0.56	+0.22	+0.17	+0.34	+0.29	+0.35	+0.02	-0.42	-0.42	+0.24	+0.15	+0.59
270316C7	...	+0.23	+0.19	+0.32	+0.34	+0.42	+0.01	-0.37	-0.37	+0.14	+0.19	+0.04
275181C7	+0.53	+0.12	+0.29	+0.39	+0.34	+0.53	+0.17	-0.59	-0.59	+0.21	+0.09	+0.36
277490C7	+0.45	-0.07	+0.31	+0.30	+0.33	+0.37	-0.05	-0.56	-0.55	+0.17	+0.12	+0.00
278419C7	-0.36	+0.18	+0.05	+0.14	+0.00	+0.28	-0.01	+0.20	...	+0.22	+0.08	...
282804C7	-0.21	+0.26	-0.03	+0.22	+0.07	+0.21	+0.04	+0.10	...	+0.11	+0.11	+0.25
286252C7	...	+0.10	-0.15	+0.01	+0.02	+0.07	-0.16	+0.42	+0.44	+0.18	+0.21	+0.77
45512C2	+0.64	-0.11	+0.21	+0.10	+0.36	+0.12	-0.21	-0.30	-0.23	+0.11	+0.20	+0.52
47188C2	+0.71	-0.08	+0.38	+0.17	+0.37	+0.33	-0.06	-0.52	...	+0.11	+0.10	...
77186C3	-0.07	+0.10	-0.03	-0.11	+0.07	-0.06	+0.07	+0.41	+0.41	+0.18	+0.13	+0.55



TABLE 3 — *Continued*

ID	[O/Fe] <sup>a</sup>	[Na/Fe]	[Mg/Fe]	[Al/Fe]	[Si/Fe]	[Ca/Fe]	[Cr/Fe]	[Fe I/H]	[Fe II/H]	[Co/Fe]	[Ni/Fe]	[Cu/Fe]
77707C3	-0.30	+0.00	-0.04	-0.03	-0.20	-0.02	+0.06	+0.44	+0.43	+0.23	+0.10	+0.48
80582C3	...	+0.06	+0.21	+0.03	+0.08	+0.11	+0.03	+0.07	+0.06	+0.28	+0.12	+0.79
81644C3	-0.08	+0.13	+0.03	+0.15	+0.09	+0.11	+0.10	+0.22	+0.20	+0.15	+0.09	+0.33
82227C3	-0.06	+0.05	+0.03	+0.09	+0.11	+0.03	-0.17	+0.25	...	+0.15	+0.21	+0.57
83531C3	-0.06	+0.04	+0.06	-0.20	+0.02	-0.04	-0.07	+0.45	+0.44	+0.25	+0.16	+0.77
84255C3	+0.36	-0.24	+0.34	+0.16	+0.20	+0.55	-0.03	-0.70	-0.66	-0.05	-0.01	-0.03
86757C3	...	+0.02	+0.04	+0.02	-0.05	+0.03	+0.01	-0.02	-0.02	+0.03	+0.09	+0.39
88522C3	...	+0.09	-0.02	-0.05	+0.06	+0.03	+0.02	+0.37	+0.40	+0.14	+0.09	+0.50
NGC 6553												
225847C6	...	-0.03	+0.10	+0.00	+0.26	+0.02	-0.18	-0.11	-0.10	-0.06	+0.10	...
227379C6	+0.24	+0.30	+0.23	+0.04	+0.36	+0.15	-0.08	-0.05	-0.06	+0.12	+0.07	...
228407C6	...	+0.45	+0.19	+0.28	+0.22	+0.28	+0.08	-0.21	-0.23	+0.11	+0.07	+0.38
230208C6	...	-0.26	+0.07	-0.02	+0.04	+0.04	-0.14	+0.01	-0.01	+0.00	-0.01	+0.31
239284C6	...	+0.17	+0.23	+0.27	+0.16	+0.35	+0.12	-0.14	...	+0.16	+0.14	...
265795C7	...	+0.17	+0.02	+0.21	+0.04	+0.40	+0.11	-0.07	...	+0.21	+0.04	+0.84
268360C7	...	+0.00	+0.11	+0.23	+0.10	+0.22	+0.04	-0.04	-0.12	+0.31	+0.16	+0.51
268493C7	...	+0.46	+0.24	+0.35	+0.27	+0.20	-0.05	-0.19	-0.20	+0.20	+0.05	+0.49
271021C7	...	+0.12	+0.09	+0.01	+0.11	+0.29	+0.19	-0.07	-0.05	+0.15	+0.09	+0.26
271400C7	...	+0.22	+0.24	+0.30	+0.16	+0.32	+0.14	-0.18	-0.20	+0.25	+0.06	+0.45
77182C3	...	+0.18	+0.21	+0.11	+0.07	+0.19	-0.01	-0.09	-0.09	+0.13	+0.14	...
85597C3	...	+0.13	+0.20	+0.22	+0.23	+0.18	-0.07	-0.15	...	+0.10	+0.10	+0.50
(l,b)=(0,-12)												
1156C2	+0.31	+0.06	+0.35	+0.24	+0.35	+0.27	-0.06	-0.45	-0.46	+0.16	+0.09	+0.22
1407C3	+0.55	-0.06	+0.26	+0.10	+0.23	+0.38	+0.09	-0.61	-0.62	+0.05	-0.07	-0.06
1491C7	+0.56	+0.19	+0.37	+0.32	+0.26	+0.38	+0.13	-0.32	...	+0.32	+0.09	+0.19
1554C7	+0.61	+0.05	+0.42	+0.37	+0.24	+0.44	+0.25	-0.67	...	+0.17	+0.01	-0.01
166C3	+0.56	-0.18	+0.42	+0.48	+0.20	+0.46	+0.04	-0.82	-0.83	+0.17	-0.09	-0.19
1754C3	...	+0.03	+0.29	+0.12	+0.26	+0.34	+0.00	-0.22	-0.28	+0.22	+0.06	+0.11
1814C1	+0.57	-0.05	+0.28	+0.20	+0.25	+0.27	-0.04	-0.30	-0.29	+0.25	+0.13	+0.37
1876C2	...	-0.18	+0.40	+0.17	+0.43	+0.44	-0.14	-1.02	-1.04	+0.02	-0.07	-0.41
1917C1	...	+0.20	-0.07	+0.02	-0.07	+0.09	+0.03	+0.20	+0.16	+0.13	+0.14	+0.37
1918C1	+0.49	-0.02	+0.35	+0.23	+0.28	+0.29	-0.04	-0.43	-0.44	+0.13	+0.10	-0.01
201583C3	...	-0.09	+0.38	+0.11	+0.15	+0.50	...	-1.11	-1.10	...	+0.10	-0.77
2110C7	+0.33	-0.05	+0.12	+0.15	+0.17	+0.18	-0.04	+0.01	+0.02	+0.15	+0.09	+0.52
2178C7	+0.20	-0.06	+0.17	+0.12	+0.17	-0.01	-0.19	+0.01	-0.01	+0.06	+0.09	+0.15
2200C3	...	-0.01	+0.26	+0.15	+0.20	+0.16	+0.08	-0.10	-0.10	+0.15	+0.11	+0.32
2220C7	+0.23	+0.24	+0.36	+0.39	+0.03	+0.53	+0.33	-0.17	...	+0.24	+0.02	+0.32
222C3	...	-0.01	+0.36	+0.32	+0.28	+0.23	+0.10	-0.42	-0.43	+0.22	+0.09	+0.19
2335C2	+0.47	-0.20	+0.34	+0.26	+0.29	+0.39	-0.03	-0.91	-0.89	+0.04	+0.03	-0.24
2407C2	+0.38	-0.13	+0.24	+0.23	+0.37	+0.40	-0.15	-0.64	-0.63	+0.01	+0.05	-0.14
2422C7	-0.18	+0.05	+0.05	-0.07	+0.20	-0.11	-0.16	+0.17	...	+0.00	+0.08	+0.15
2470C3	+0.14	+0.06	+0.27	+0.16	+0.09	+0.17	+0.04	+0.00	-0.01	+0.22	+0.10	+0.37
2502C3	+0.52	+0.05	+0.30	+0.21	+0.27	+0.38	+0.14	-0.63	-0.61	+0.10	+0.02	-0.10
2532C6	+0.59	+0.02	+0.36	+0.20	+0.23	+0.19	-0.05	-0.18	-0.16	+0.25	+0.08	+0.55
2580C6	+0.04	+0.23	+0.13	+0.05	+0.25	-0.05	+0.13	+0.30	+0.30	+0.24	+0.23	+0.47
2769C3	+0.03	+0.07	+0.17	+0.14	+0.06	+0.25	+0.07	+0.06	+0.06	+0.06	+0.09	+0.21
2772C7	+0.69	+0.11	+0.25	+0.30	+0.29	+0.23	-0.03	-0.25	-0.24	+0.25	+0.10	+0.37
2812C8	+0.45	-0.11	+0.30	+0.29	+0.33	+0.30	-0.02	-0.64	-0.65	+0.08	+0.08	+0.16
2947C3	+0.65	-0.08	+0.24	+0.26	+0.24	+0.25	+0.02	-0.49	-0.50	+0.24	+0.08	+0.24
2948C7	-0.38	+0.28	+0.03	+0.03	+0.04	+0.13	-0.01	+0.12	...	-0.04	+0.15	+0.05
3018C3	+0.52	-0.10	+0.28	+0.22	+0.26	+0.30	-0.06	-0.53	-0.55	+0.15	+0.05	+0.15
3035C7	+0.65	-0.24	+0.26	+0.09	+0.27	+0.34	-0.13	-0.44	-0.43	+0.06	+0.02	-0.07
3091C8	+0.53	+0.00	+0.38	+0.26	+0.25	+0.29	+0.00	-0.49	-0.50	+0.20	+0.13	+0.11
3101C7	+0.50	-0.07	+0.37	+0.21	+0.32	+0.22	-0.05	-0.39	-0.40	+0.22	+0.09	+0.07
3142C3	+0.51	-0.09	+0.27	+0.19	+0.25	+0.16	+0.00	-0.22	-0.21	+0.13	+0.09	+0.21
3161C3	...	+0.16	+0.29	+0.31	+0.08	+0.29	+0.15	-0.14	-0.16	+0.34	+0.07	+0.41
3191C7	+0.55	-0.06	+0.37	+0.21	+0.24	+0.29	-0.01	-0.36	-0.37	+0.13	+0.09	+0.09

TABLE 3 — *Continued*

ID	[O/Fe] <sup>a</sup>	[Na/Fe]	[Mg/Fe]	[Al/Fe]	[Si/Fe]	[Ca/Fe]	[Cr/Fe]	[Fe I/H]	[Fe II/H]	[Co/Fe]	[Ni/Fe]	[Cu/Fe]
3201C6	+0.01	+0.04	+0.12	+0.19	+0.03	+0.25	+0.14	+0.03	+0.04	+0.12	+0.04	+0.22
3238C6	...	-0.01	+0.19	+0.18	+0.20	+0.23	-0.03	-0.21	-0.22	+0.24	+0.11	+0.32
3267C3	-0.13	-0.15	+0.09	-0.02	+0.14	+0.05	-0.19	+0.04	+0.03	+0.01	+0.09	+0.18
3515C3	...	+0.27	+0.19	+0.15	+0.13	+0.26	+0.08	+0.01	+0.01	+0.11	+0.05	+0.30
3558C6	...	+0.01	+0.33	+0.20	+0.19	+0.16	-0.15	-0.15	-0.14	+0.22	+0.11	+0.57
3690C7	+0.47	-0.32	+0.28	+0.38	+0.30	+0.24	...	-1.48	-1.43	-0.20	+0.03	-0.75
3711C7	+0.56	+0.00	+0.27	+0.22	+0.09	+0.42	+0.23	-0.47	-0.50	+0.24	+0.06	+0.04
3733C3	+0.47	-0.01	+0.22	+0.14	+0.15	+0.22	-0.04	-0.18	-0.17	+0.16	+0.03	+0.35
3796C6	+0.75	-0.08	+0.37	+0.19	+0.27	+0.24	-0.04	-0.83	-0.81	+0.13	+0.09	+0.25
3965C6	+0.44	+0.18	+0.28	+0.18	+0.21	+0.28	+0.02	-0.08	-0.09	+0.24	+0.18	+0.59
4085C3	+0.48	-0.02	+0.44	+0.29	+0.32	+0.39	+0.10	-0.59	-0.57	+0.14	+0.06	+0.11
4217C6	+0.70	+0.08	+0.37	+0.37	+0.42	+0.36	+0.05	-0.57	-0.57	+0.27	+0.10	+0.44
4263C6	+0.57	+0.22	+0.32	+0.35	+0.24	+0.31	+0.12	-0.33	-0.34	+0.30	+0.09	+0.45
431C2	+0.16	+0.14	+0.28	+0.17	+0.09	+0.17	+0.02	-0.02	-0.04	+0.21	+0.13	+0.33
4365C3	...	-0.09	+0.10	+0.05	+0.18	+0.31	-0.24	-0.80	-0.79	-0.18	+0.00	-0.33
4478C8	+0.34	-0.07	+0.36	+0.25	+0.24	+0.32	+0.03	-0.35	-0.36	+0.11	+0.08	-0.01
455C1	+0.46	-0.05	+0.32	+0.20	+0.33	+0.42	-0.06	-0.62	-0.60	-0.03	+0.03	-0.17
4612C6	+0.48	-0.21	+0.25	+0.29	+0.33	+0.38	+0.11	-0.79	-0.76	-0.03	+0.06	-0.16
4740C8	+0.53	-0.08	+0.33	+0.23	+0.28	+0.37	-0.04	-0.49	-0.49	+0.21	+0.01	-0.10
4876C6	+0.53	+0.04	+0.34	+0.24	+0.30	+0.32	+0.00	-0.59	-0.59	+0.09	+0.09	+0.11
5319C6	+0.56	-0.15	+0.25	+0.17	+0.35	+0.33	-0.01	-0.40	-0.40	+0.13	+0.07	+0.07
5351C8	+0.48	-0.07	+0.22	+0.10	+0.20	+0.07	-0.08	-0.09	-0.08	+0.19	+0.08	+0.36
5400C8	...	+0.01	+0.06	-0.07	+0.11	+0.03	-0.07	+0.13	+0.10	+0.07	+0.14	+0.17
5487C8	...	-0.09	+0.22	+0.11	+0.14	+0.16	-0.09	-0.47	-0.47	+0.03	+0.03	+0.04
5543C6	-0.34	+0.03	+0.17	+0.09	+0.26	+0.19	+0.06	-0.17	-0.16	-0.18	+0.03	-0.36
5588C6	+0.44	-0.07	+0.33	+0.05	+0.20	+0.19	-0.03	-0.20	-0.19	+0.15	+0.04	+0.09
5664C6	-0.09	+0.27	+0.00	+0.12	+0.14	+0.29	+0.10	+0.23	...	+0.03	+0.08	+0.24
5908C6	+0.51	-0.07	+0.32	+0.22	+0.25	+0.27	-0.08	-0.67	-0.67	+0.10	+0.06	-0.01
5977C6	-0.16	+0.28	+0.15	+0.05	+0.26	+0.06	-0.12	+0.17	+0.20	+0.01	+0.13	+0.25
5980C6	...	-0.10	+0.30	+0.11	+0.18	+0.18	+0.06	-0.17	-0.16	+0.25	+0.17	+0.69
608C1	+0.68	-0.31	...	...	+0.31	+0.30	+0.06	-1.74	-1.74	...	-0.08	-0.84
6090C6	-0.34	-0.11	+0.04	+0.02	+0.20	+0.03	-0.05	-0.02	...	-0.17	+0.06	-0.15
6164C6	+0.20	-0.07	+0.21	+0.14	+0.09	+0.20	-0.11	-0.11	-0.14	+0.07	+0.10	+0.22
6230C5	...	-0.01	+0.01	-0.13	-0.01	-0.01	-0.06	+0.19	+0.21	-0.05	+0.02	+0.28
6263C6	...	+0.20	-0.08	-0.14	+0.13	+0.00	-0.22	+0.48	...	+0.07	+0.26	+0.29
6391C8	+0.48	-0.12	+0.24	+0.27	+0.25	+0.32	-0.10	-0.64	-0.61	+0.07	+0.06	-0.07
6419C5	+0.33	-0.01	+0.24	+0.24	+0.18	+0.23	+0.06	-0.24	-0.24	+0.25	+0.13	+0.51
6426C8	...	+0.04	+0.41	+0.21	+0.35	+0.35	+0.06	-0.39	-0.41	+0.06	+0.11	+0.21
6505C6	+0.76	-0.16	+0.32	+0.19	+0.22	+0.23	-0.07	-0.37	-0.38	+0.12	+0.06	+0.09
650C2	+0.40	+0.01	+0.39	+0.26	+0.29	+0.36	-0.04	-0.66	-0.67	+0.09	+0.04	+0.13
6549C6	+0.10	-0.01	-0.02	+0.06	-0.02	+0.04	-0.02	+0.34	+0.32	+0.09	+0.11	+0.33
6637C8	+0.55	+0.07	+0.26	+0.14	+0.28	+0.30	-0.04	-0.26	-0.26	+0.11	+0.14	+0.16
6717C6	+0.62	-0.02	+0.24	+0.18	+0.12	+0.12	-0.02	-0.18	-0.19	+0.08	+0.09	+0.25
6828C7	-0.38	-0.02	+0.05	-0.01	+0.11	+0.06	-0.12	+0.12	+0.08	-0.03	+0.07	+0.15
6913C7	+0.32	-0.07	+0.26	+0.18	+0.23	+0.22	-0.04	-0.28	-0.26	+0.18	+0.10	+0.20
867C3	+0.58	-0.07	+0.32	+0.19	+0.24	+0.26	-0.17	-0.47	-0.47	+0.12	+0.06	+0.12

<sup>a</sup> The [O/Fe] ratio is normalized to the [Fe II/H] abundance. For stars without a [Fe II/H] measurement, the [O/Fe] ratio was normalized to the [Fe I/H] abundance.

TABLE 4  
TOTAL ABUNDANCE UNCERTAINTY FOR  $\Delta T_{\text{eff}}+100$  K;  $\Delta \text{LOG}(g)+0.3$  CGS;  
 $\Delta [M/H]+0.15$  DEX;  $\Delta v_T+0.3$  KM S $^{-1}$

ID	$\Delta[\text{O}/\text{Fe}]$	$\Delta[\text{Na}/\text{Fe}]$	$\Delta[\text{Mg}/\text{Fe}]$	$\Delta[\text{Al}/\text{Fe}]$	$\Delta[\text{Si}/\text{Fe}]$	$\Delta[\text{Ca}/\text{Fe}]$	$\Delta[\text{Cr}/\text{Fe}]$	$\Delta[\text{Fe I}/\text{H}]$	$\Delta[\text{Fe II}/\text{H}]$	$\Delta[\text{Co}/\text{Fe}]$	$\Delta[\text{Ni}/\text{Fe}]$	$\Delta[\text{Cu}/\text{Fe}]$
	(l,b)=(+5.25,-3.02)											
119799C4	0.19	0.08	0.03	0.08	0.10	0.14	0.09	0.11	0.27	0.05	0.05	0.15
129499C4	...	0.06	0.04	0.05	0.09	0.09	0.05	0.10	...	0.05	0.04	...
176772C5	0.20	0.12	0.04	0.10	0.08	0.17	0.09	0.13	0.25	0.04	0.03	...
181349C5	0.14	0.10	0.03	0.07	0.08	0.12	0.07	0.11	0.21	0.05	0.04	...
183783C5	...	0.09	0.04	0.07	0.08	0.12	0.07	0.10	...	0.05	0.04	...
184088C5	0.17	0.09	0.03	0.07	0.09	0.14	0.09	0.10	0.27	0.05	0.05	0.15
184618C5	...	0.06	0.03	0.05	0.08	0.10	0.07	0.10	0.20	0.06	0.04	0.15
185169C5	...	0.05	0.03	0.05	0.09	0.11	0.06	0.10	...	0.04	0.04	0.16
185357C5	0.19	0.10	0.04	0.08	0.09	0.14	0.08	0.12	0.25	0.04	0.04	...
185541C5	0.16	0.10	0.03	0.07	0.08	0.14	0.08	0.10	0.23	0.05	0.04	...
187067C5	...	0.03	0.04	0.03	0.09	0.06	0.03	0.09	0.17	0.06	0.03	0.05
193190C5	...	0.10	0.04	0.07	0.09	0.13	0.07	0.11	0.22	0.03	0.04	...
197366C5	0.19	0.13	0.03	0.08	0.09	0.17	0.08	0.12	0.27	0.05	0.04	...
215681C6	0.15	0.07	0.04	0.06	0.09	0.11	0.06	0.11	...	0.04	0.04	0.16
216922C6	0.20	0.10	0.03	0.08	0.09	0.15	0.09	0.10	0.26	0.05	0.05	...
218198C6	0.22	0.13	0.04	0.10	0.09	0.18	0.11	0.12	0.29	0.04	0.04	...
219909C6	0.12	0.05	0.04	0.04	0.09	0.09	0.05	0.09	0.19	0.04	0.04	...
221537C6	0.14	0.08	0.04	0.06	0.09	0.12	0.07	0.12	...	0.05	0.04	...
223113C6	0.13	0.04	0.03	0.04	0.09	0.09	0.05	0.10	0.23	0.06	0.06	...
223343C6	0.18	0.09	0.04	0.07	0.09	0.14	0.08	0.12	0.24	0.04	0.04	...
223621C6	...	0.06	0.04	0.05	0.09	0.12	0.04	0.09	0.18	0.05	0.04	...
223722C6	0.13	0.05	0.04	0.04	0.10	0.07	0.05	0.11	0.20	0.05	0.03	...
224206C6	...	0.08	0.04	0.06	0.09	0.13	0.07	0.12	0.29	0.05	0.05	...
224866C6	0.20	0.11	0.03	0.09	0.09	0.16	0.10	0.12	0.26	0.05	0.05	...
224951C6	0.15	0.09	0.04	0.07	0.08	0.13	0.07	0.12	...	0.04	0.04	...
225531C6	0.16	0.07	0.03	0.06	0.09	0.11	0.07	0.09	0.20	0.05	0.04	0.15
226450C6	0.14	0.10	0.04	0.09	0.09	0.17	0.10	0.14	...	0.04	0.04	...
226850C6	...	0.03	0.03	0.03	0.08	0.05	0.03	0.09	0.16	0.06	0.05	0.05
227867C6	0.13	0.07	0.04	0.06	0.08	0.12	0.07	0.10	0.20	0.05	0.04	0.15
228466C6	0.10	0.03	0.04	0.03	0.09	0.05	0.03	0.10	0.17	0.05	0.04	0.07
229507C6	...	0.05	0.04	0.05	0.10	0.08	0.06	0.12	0.20	0.05	0.04	0.15
230424C6	0.17	0.08	0.03	0.07	0.09	0.13	0.08	0.09	0.23	0.04	0.04	0.14
230483C6	0.16	0.09	0.04	0.07	0.08	0.13	0.09	0.10	0.23	0.05	0.04	...
231379C6	0.16	0.09	0.03	0.08	0.09	0.14	0.09	0.10	0.22	0.05	0.04	0.16
231618C6	0.18	0.09	0.04	0.08	0.09	0.14	0.09	0.12	0.25	0.05	0.04	0.16
232493C6	0.12	0.03	0.03	0.03	0.09	0.07	0.05	0.09	0.21	0.05	0.04	0.05
233121C6	0.15	0.07	0.03	0.07	0.09	0.10	0.09	0.10	0.23	0.06	0.05	...
233560C6	0.19	0.11	0.04	0.09	0.09	0.16	0.10	0.11	0.26	0.04	0.04	0.16
233708C6	0.20	0.10	0.04	0.08	0.10	0.16	0.09	0.14	0.30	0.04	0.05	0.15
240059C6	0.15	0.07	0.05	0.06	0.11	0.11	0.07	0.10	0.22	0.04	0.04	...
240083C6	0.16	0.08	0.04	0.07	0.09	0.11	0.09	0.11	0.22	0.06	0.04	...
259050C7	0.18	0.10	0.04	0.09	0.10	0.14	0.10	0.11	0.26	0.04	0.04	...
259377C7	...	0.06	0.04	0.05	0.08	0.10	0.05	0.09	...	0.05	0.04	0.16
260308C7	0.18	0.11	0.04	0.09	0.09	0.15	0.08	0.13	0.30	0.04	0.04	...
262018C7	0.14	0.09	0.04	0.08	0.09	0.11	0.07	0.11	0.21	0.04	0.04	0.15
266442C7	0.20	0.10	0.04	0.09	0.09	0.16	0.10	0.12	0.29	0.04	0.04	0.18
270316C7	...	0.09	0.04	0.07	0.10	0.15	0.09	0.11	0.26	0.04	0.04	0.15
275181C7	0.17	0.09	0.04	0.07	0.09	0.13	0.08	0.10	0.21	0.04	0.04	0.16
277490C7	0.19	0.11	0.04	0.09	0.09	0.16	0.12	0.12	0.27	0.05	0.03	0.14
278419C7	0.15	0.08	0.04	0.06	0.08	0.12	0.07	0.11	...	0.05	0.04	...
282804C7	0.14	0.09	0.04	0.07	0.09	0.15	0.08	0.13	...	0.03	0.04	0.16
286252C7	...	0.10	0.04	0.07	0.08	0.16	0.07	0.11	0.24	0.05	0.04	0.14
45512C2	0.16	0.09	0.04	0.08	0.08	0.12	0.09	0.11	0.22	0.06	0.05	0.17
47188C2	0.15	0.09	0.04	0.08	0.09	0.13	0.08	0.10	...	0.04	0.04	...

TABLE 4 — *Continued*

ID	$\Delta[\text{O}/\text{Fe}]$	$\Delta[\text{Na}/\text{Fe}]$	$\Delta[\text{Mg}/\text{Fe}]$	$\Delta[\text{Al}/\text{Fe}]$	$\Delta[\text{Si}/\text{Fe}]$	$\Delta[\text{Ca}/\text{Fe}]$	$\Delta[\text{Cr}/\text{Fe}]$	$\Delta[\text{Fe I}/\text{H}]$	$\Delta[\text{Fe II}/\text{H}]$	$\Delta[\text{Co}/\text{Fe}]$	$\Delta[\text{Ni}/\text{Fe}]$	$\Delta[\text{Cu}/\text{Fe}]$
77186C3	0.16	0.09	0.03	0.07	0.08	0.13	0.07	0.10	0.21	0.05	0.04	0.16
77707C3	0.16	0.08	0.04	0.07	0.08	0.12	0.07	0.11	0.21	0.05	0.04	0.16
80582C3	...	0.06	0.03	0.05	0.08	0.11	0.05	0.09	0.22	0.05	0.04	0.15
81644C3	0.19	0.10	0.04	0.08	0.09	0.16	0.08	0.12	0.26	0.05	0.04	0.15
82227C3	0.15	0.07	0.04	0.06	0.09	0.12	0.06	0.10	...	0.05	0.04	0.15
83531C3	0.17	0.11	0.03	0.07	0.08	0.15	0.07	0.10	0.21	0.05	0.03	0.14
84255C3	0.17	0.08	0.05	0.07	0.10	0.13	0.09	0.12	0.27	0.04	0.04	0.14
86757C3	...	0.10	0.04	0.08	0.09	0.13	0.09	0.12	0.22	0.04	0.03	0.16
88522C3	...	0.09	0.03	0.07	0.09	0.15	0.08	0.12	0.29	0.05	0.04	0.15
NGC 6553												
225847C6	...	0.09	0.04	0.09	0.08	0.13	0.10	0.12	0.22	0.07	0.05	...
227379C6	0.19	0.12	0.04	0.09	0.09	0.16	0.09	0.13	0.24	0.04	0.03	...
228407C6	...	0.10	0.04	0.08	0.10	0.15	0.09	0.13	0.28	0.03	0.04	0.17
230208C6	...	0.06	0.04	0.05	0.09	0.11	0.06	0.10	0.24	0.04	0.04	0.15
239284C6	...	0.11	0.04	0.09	0.10	0.18	0.10	0.13	...	0.03	0.05	...
265795C7	...	0.09	0.04	0.08	0.09	0.15	0.09	0.12	...	0.05	0.05	0.17
268360C7	...	0.09	0.04	0.07	0.08	0.14	0.07	0.09	0.21	0.05	0.04	0.16
268493C7	...	0.10	0.03	0.09	0.08	0.14	0.10	0.11	0.23	0.06	0.03	0.15
271021C7	...	0.07	0.04	0.06	0.09	0.11	0.07	0.12	0.26	0.03	0.04	0.16
271400C7	...	0.10	0.04	0.09	0.08	0.16	0.09	0.11	0.29	0.04	0.04	0.16
77182C3	...	0.07	0.04	0.06	0.09	0.11	0.08	0.11	0.26	0.04	0.05	...
85597C3	...	0.11	0.04	0.09	0.09	0.16	0.09	0.12	...	0.04	0.04	0.17
(l,b)=(0,-12)												
1156C2	0.19	0.11	0.04	0.09	0.09	0.14	0.10	0.12	0.24	0.05	0.04	0.16
1407C3	0.10	0.03	0.04	0.03	0.08	0.04	0.03	0.09	0.18	0.05	0.04	0.05
1491C7	0.13	0.05	0.04	0.05	0.09	0.09	0.06	0.10	...	0.04	0.04	0.13
1554C7	0.14	0.03	0.04	0.03	0.06	0.06	0.02	0.10	...	0.04	0.02	0.07
166C3	0.10	0.03	0.04	0.03	0.07	0.06	0.04	0.09	0.16	0.06	0.04	0.06
1754C3	...	0.03	0.04	0.04	0.10	0.08	0.05	0.10	0.23	0.04	0.05	0.12
1814C1	0.16	0.07	0.03	0.06	0.09	0.12	0.07	0.10	0.22	0.06	0.05	0.16
1876C2	...	0.03	0.04	0.04	0.07	0.05	0.03	0.10	0.16	0.03	0.03	0.04
1917C1	...	0.09	0.04	0.07	0.08	0.12	0.07	0.11	0.21	0.05	0.04	0.17
1918C1	0.11	0.04	0.03	0.03	0.08	0.06	0.04	0.10	0.20	0.06	0.04	0.09
201583C3	...	0.03	0.04	0.03	0.08	0.04	...	0.10	0.17	...	0.04	0.07
2110C7	0.18	0.09	0.04	0.07	0.08	0.16	0.08	0.11	0.29	0.05	0.05	0.17
2178C7	0.15	0.08	0.04	0.07	0.09	0.12	0.07	0.11	0.22	0.04	0.04	0.12
2200C3	...	0.05	0.04	0.04	0.08	0.08	0.04	0.10	0.17	0.04	0.04	0.13
2220C7	0.12	0.04	0.04	0.03	0.08	0.08	0.02	0.09	...	0.04	0.03	0.13
222C3	...	0.03	0.03	0.03	0.08	0.06	0.03	0.09	0.18	0.05	0.04	0.10
2335C2	0.09	0.04	0.05	0.04	0.09	0.06	0.03	0.11	0.18	0.04	0.04	0.04
2407C2	0.09	0.02	0.03	0.03	0.07	0.05	0.03	0.09	0.17	0.06	0.04	0.06
2422C7	0.15	0.09	0.04	0.08	0.09	0.14	0.09	0.13	...	0.05	0.04	0.15
2470C3	0.14	0.08	0.04	0.06	0.09	0.13	0.07	0.11	0.23	0.04	0.04	0.15
2502C3	0.10	0.04	0.04	0.04	0.09	0.07	0.04	0.10	0.18	0.04	0.04	0.08
2532C6	0.14	0.06	0.04	0.05	0.10	0.10	0.06	0.11	0.25	0.04	0.05	0.17
2580C6	0.19	0.11	0.03	0.07	0.09	0.15	0.08	0.11	0.26	0.05	0.04	0.15
2769C3	0.14	0.07	0.04	0.06	0.08	0.11	0.06	0.10	0.21	0.05	0.04	0.14
2772C7	0.12	0.04	0.03	0.04	0.08	0.08	0.05	0.09	0.19	0.06	0.05	0.14
2812C8	0.16	0.07	0.04	0.07	0.09	0.12	0.09	0.10	0.26	0.05	0.05	0.15
2947C3	0.09	0.02	0.03	0.03	0.07	0.04	0.03	0.09	0.17	0.06	0.04	0.08
2948C7	0.14	0.12	0.04	0.09	0.10	0.18	0.10	0.16	...	0.04	0.04	0.15
3018C3	0.14	0.07	0.04	0.06	0.09	0.11	0.07	0.09	0.23	0.04	0.04	0.14
3035C7	0.10	0.03	0.04	0.03	0.08	0.05	0.03	0.10	0.19	0.05	0.04	0.07
3091C8	0.12	0.04	0.03	0.04	0.09	0.09	0.05	0.08	0.22	0.06	0.05	0.11
3101C7	0.10	0.04	0.03	0.04	0.07	0.07	0.04	0.10	0.18	0.06	0.03	0.09
3142C3	0.13	0.04	0.03	0.04	0.08	0.07	0.05	0.09	0.19	0.06	0.05	0.12
3161C3	...	0.04	0.04	0.04	0.08	0.08	0.03	0.09	0.17	0.05	0.04	0.12

TABLE 4 — *Continued*

ID	$\Delta[\text{O}/\text{Fe}]$	$\Delta[\text{Na}/\text{Fe}]$	$\Delta[\text{Mg}/\text{Fe}]$	$\Delta[\text{Al}/\text{Fe}]$	$\Delta[\text{Si}/\text{Fe}]$	$\Delta[\text{Ca}/\text{Fe}]$	$\Delta[\text{Cr}/\text{Fe}]$	$\Delta[\text{Fe I}/\text{H}]$	$\Delta[\text{Fe II}/\text{H}]$	$\Delta[\text{Co}/\text{Fe}]$	$\Delta[\text{Ni}/\text{Fe}]$	$\Delta[\text{Cu}/\text{Fe}]$
3191C7	0.11	0.03	0.03	0.03	0.09	0.06	0.04	0.10	0.22	0.05	0.05	0.11
3201C6	0.11	0.04	0.04	0.03	0.08	0.10	0.04	0.09	0.22	0.05	0.05	0.13
3238C6	...	0.05	0.04	0.05	0.09	0.10	0.06	0.10	0.24	0.06	0.05	0.14
3267C3	0.16	0.07	0.04	0.06	0.09	0.11	0.07	0.11	0.22	0.05	0.04	0.16
3515C3	...	0.09	0.04	0.07	0.08	0.11	0.07	0.10	0.19	0.04	0.04	0.14
3558C6	...	0.06	0.03	0.05	0.08	0.10	0.06	0.10	0.20	0.06	0.04	0.15
3690C7	0.08	0.03	0.05	0.04	0.06	0.03	...	0.10	0.15	0.06	0.02	0.06
3711C7	0.09	0.02	0.03	0.02	0.07	0.06	0.03	0.07	0.15	0.06	0.04	0.06
3733C3	0.13	0.06	0.03	0.05	0.09	0.10	0.07	0.10	0.21	0.06	0.05	0.15
3796C6	0.13	0.06	0.04	0.06	0.10	0.09	0.06	0.10	0.21	0.04	0.04	0.15
3965C6	0.19	0.11	0.04	0.09	0.09	0.17	0.09	0.12	0.26	0.04	0.04	0.17
4085C3	0.13	0.07	0.04	0.06	0.10	0.10	0.07	0.10	0.23	0.04	0.04	0.14
4217C6	0.13	0.07	0.04	0.06	0.10	0.11	0.07	0.10	0.20	0.03	0.04	0.16
4263C6	0.11	0.03	0.03	0.03	0.08	0.08	0.04	0.09	0.19	0.06	0.04	0.12
431C2	0.12	0.06	0.04	0.04	0.08	0.12	0.04	0.08	0.21	0.06	0.04	0.13
4365C3	...	0.03	0.04	0.03	0.06	0.04	0.03	0.10	0.16	0.05	0.03	0.05
4478C8	0.12	0.03	0.03	0.04	0.08	0.06	0.05	0.10	0.19	0.06	0.04	0.09
455C1	0.07	0.02	0.04	0.03	0.08	0.07	0.02	0.10	0.15	0.04	0.03	0.05
4612C6	0.10	0.03	0.03	0.03	0.08	0.06	0.03	0.09	0.17	0.05	0.04	0.06
4740C8	0.08	0.03	0.04	0.03	0.08	0.07	0.03	0.10	0.17	0.04	0.03	0.08
4876C6	0.10	0.04	0.04	0.04	0.09	0.09	0.04	0.09	0.17	0.05	0.04	0.11
5319C6	0.16	0.07	0.04	0.07	0.09	0.13	0.08	0.10	0.26	0.04	0.04	0.13
5351C8	0.14	0.07	0.04	0.07	0.09	0.10	0.07	0.10	0.21	0.05	0.04	0.16
5400C8	...	0.08	0.03	0.05	0.08	0.12	0.05	0.08	0.19	0.06	0.04	0.12
5487C8	...	0.05	0.04	0.04	0.09	0.08	0.05	0.10	0.19	0.04	0.03	0.11
5543C6	0.19	0.08	0.04	0.08	0.09	0.12	0.09	0.12	0.26	0.06	0.04	0.08
5588C6	0.13	0.04	0.03	0.04	0.09	0.08	0.05	0.10	0.21	0.06	0.04	0.11
5664C6	0.14	0.08	0.04	0.06	0.08	0.12	0.06	0.11	...	0.05	0.04	0.16
5908C6	0.09	0.03	0.04	0.03	0.07	0.04	0.03	0.09	0.19	0.05	0.02	0.04
5977C6	0.18	0.08	0.04	0.07	0.09	0.12	0.08	0.13	0.28	0.05	0.05	0.17
5980C6	...	0.05	0.03	0.05	0.09	0.12	0.06	0.09	0.22	0.07	0.06	0.14
608C1	0.06	0.04	...	...	0.07	0.03	0.02	0.09	0.13	...	0.02	0.02
6090C6	0.15	0.10	0.04	0.09	0.08	0.13	0.10	0.12	...	0.05	0.03	0.11
6164C6	0.14	0.06	0.03	0.06	0.08	0.11	0.07	0.10	0.20	0.07	0.04	0.13
6230C5	...	0.07	0.04	0.05	0.08	0.11	0.06	0.10	0.21	0.06	0.04	0.13
6263C6	...	0.13	0.04	0.08	0.08	0.18	0.09	0.14	...	0.05	0.03	0.15
6391C8	0.10	0.03	0.04	0.03	0.07	0.04	0.03	0.11	0.15	0.05	0.04	0.07
6419C5	0.13	0.07	0.04	0.06	0.09	0.11	0.07	0.10	0.21	0.03	0.04	0.18
6426C8	...	0.04	0.03	0.03	0.09	0.09	0.04	0.09	0.21	0.04	0.04	0.12
6505C6	0.09	0.03	0.03	0.03	0.07	0.05	0.04	0.10	0.15	0.06	0.04	0.10
650C2	0.18	0.09	0.04	0.08	0.10	0.12	0.10	0.11	0.26	0.06	0.05	0.16
6549C6	0.15	0.08	0.04	0.06	0.09	0.13	0.06	0.10	0.23	0.05	0.04	0.15
6637C8	0.13	0.04	0.03	0.05	0.10	0.09	0.06	0.10	0.24	0.04	0.05	0.13
6717C6	0.13	0.05	0.03	0.05	0.09	0.11	0.06	0.09	0.20	0.07	0.05	0.13
6828C7	0.18	0.08	0.04	0.07	0.10	0.13	0.08	0.12	0.28	0.04	0.04	0.16
6913C7	0.09	0.04	0.05	0.03	0.09	0.08	0.04	0.10	0.17	0.03	0.04	0.11
867C3	0.08	0.03	0.04	0.03	0.08	0.06	0.03	0.10	0.18	0.04	0.04	0.09

TABLE 5  
 $1\sigma$  LINE-TO-LINE ABUNDANCE DISPERSION

ID	$\sigma_{\text{O}}$	$\sigma_{\text{Na}}$	$\sigma_{\text{Mg}}$	$\sigma_{\text{Al}}$	$\sigma_{\text{Si}}$	$\sigma_{\text{Ca}}$	$\sigma_{\text{Cr}}$	$\sigma_{\text{FeI}}$	$\sigma_{\text{FeII}}$	$\sigma_{\text{Co}}$	$\sigma_{\text{Ni}}$	$\sigma_{\text{Cu}}$
	(l,b)=(+5.25,-3.02)											
119799C4	0.08	0.02	0.00	0.02	0.12	0.04	0.17	0.13	0.08	0.09	0.10	0.08
129499C4	...	0.04	0.07	0.11	0.17	0.12	0.10	0.14	...	0.04	0.18	...
176772C5	0.08	0.01	0.04	0.04	0.15	0.15	0.08	0.17	0.08	0.05	0.16	...
181349C5	0.08	0.25	0.07	0.08	0.21	0.08	0.18	0.15	0.08	0.07	0.16	...
183783C5	...	...	0.10	0.08	0.06	0.11	0.22	0.13	...	0.08	0.18	...
184088C5	0.08	0.00	0.07	0.00	0.11	0.09	0.16	0.13	0.00	0.04	0.12	0.08
184618C5	...	0.11	0.07	0.00	0.15	0.10	0.13	0.14	0.08	0.08	0.10	0.08
185169C5	...	0.07	0.07	0.00	0.08	0.05	0.16	0.14	...	0.08	0.10	0.08
185357C5	0.08	0.04	0.00	0.07	0.12	0.05	0.10	0.13	0.08	0.02	0.14	...
185541C5	0.08	0.07	0.02	0.07	0.21	0.09	0.13	0.15	0.01	0.08	0.13	...
187067C5	...	0.07	0.08	0.08	0.09	0.10	0.08	0.15	0.02	0.08	0.15	0.08
193190C5	...	0.07	0.04	0.08	0.17	0.19	0.09	0.12	0.08	0.14	0.09	...
197366C5	0.08	0.06	0.08	0.08	0.10	0.13	0.12	0.15	0.08	0.05	0.13	...
215681C6	0.08	0.01	0.00	0.04	0.12	0.11	0.12	0.13	...	0.05	0.15	0.08
216922C6	0.08	0.05	0.00	0.00	0.11	0.06	0.05	0.14	0.08	0.11	0.12	...
218198C6	0.08	0.01	0.00	0.04	0.05	0.09	0.04	0.14	0.08	0.08	0.16	...
219909C6	0.08	0.06	0.00	0.00	0.12	0.08	0.14	0.14	0.08	0.08	0.13	...
221537C6	0.08	0.00	0.00	0.08	0.15	0.09	0.13	0.13	...	0.00	0.15	...
223113C6	0.08	0.12	0.00	0.08	0.07	0.09	0.08	0.13	0.11	0.06	0.09	...
223343C6	0.08	0.00	0.08	0.00	0.11	0.15	0.14	0.13	0.05	0.11	0.12	...
223621C6	...	0.06	0.00	0.11	0.07	0.12	0.09	0.14	0.08	0.07	0.12	...
223722C6	0.08	0.08	0.04	0.04	0.10	0.08	0.06	0.14	0.11	0.09	0.14	...
224206C6	...	0.05	0.06	0.05	0.15	0.16	0.10	0.14	0.08	0.08	0.15	...
224866C6	0.08	0.07	0.11	0.01	0.11	0.06	0.10	0.14	0.08	0.04	0.12	...
224951C6	0.08	0.08	0.07	0.04	0.05	0.15	0.20	0.13	...	0.16	0.15	...
225531C6	0.08	0.04	0.08	...	0.12	0.08	0.07	0.13	0.09	0.08	0.11	0.08
226450C6	0.08	0.03	0.07	0.04	0.15	0.02	0.12	0.15	...	0.00	0.11	...
226850C6	...	0.07	0.00	0.04	0.13	0.11	0.07	0.12	0.10	0.04	0.10	0.08
227867C6	0.08	0.18	0.04	0.01	0.11	0.10	0.14	0.14	0.04	0.01	0.12	0.08
228466C6	0.08	0.11	0.00	0.04	0.09	0.10	0.19	0.15	0.18	0.04	0.14	0.08
229507C6	...	0.01	0.07	0.14	0.11	0.08	0.14	0.12	0.08	0.04	0.17	0.08
230424C6	0.08	0.01	0.00	0.14	0.06	0.12	0.11	0.12	0.06	0.09	0.13	0.08
230483C6	0.08	0.00	0.14	0.08	0.15	0.07	0.14	0.14	0.08	0.04	0.10	...
231379C6	0.08	0.07	0.02	0.11	0.11	0.09	0.13	0.14	0.04	0.08	0.08	0.08
231618C6	0.08	0.04	0.04	0.00	0.11	0.13	0.17	0.12	0.08	0.04	0.14	0.08
232493C6	0.08	0.07	...	0.07	0.10	0.12	0.11	0.14	0.04	0.08	0.16	0.08
233121C6	0.08	0.02	0.08	0.04	0.07	0.08	0.06	0.12	0.05	0.07	0.09	...
233560C6	0.08	0.07	0.00	0.05	0.05	0.09	0.12	0.12	0.06	0.04	0.11	0.08
233708C6	0.08	0.03	0.07	0.05	0.14	0.11	0.11	0.12	0.10	0.05	0.11	0.08
240059C6	0.08	0.01	0.07	0.04	0.11	0.09	0.10	0.11	0.08	0.02	0.07	...
240083C6	0.08	0.11	0.01	0.04	0.10	0.08	0.07	0.11	0.08	0.04	0.13	...
259050C7	0.08	0.16	0.08	0.04	0.17	0.03	0.18	0.15	0.08	0.08	0.16	...
259377C7	...	0.04	0.01	0.11	0.16	0.13	0.12	0.14	...	0.06	0.11	0.08
260308C7	0.08	0.01	0.08	0.02	0.15	0.12	0.07	0.14	0.08	0.09	0.15	...
262018C7	0.08	0.02	0.07	0.02	0.16	0.10	0.14	0.15	0.08	0.08	0.13	0.08
266442C7	0.08	0.04	0.08	0.02	0.10	0.11	0.12	0.13	0.08	0.00	0.12	0.08
270316C7	...	0.04	0.08	0.08	0.08	0.10	0.10	0.14	0.08	0.10	0.11	0.08
275181C7	0.08	0.11	0.08	0.00	0.13	0.13	0.08	0.14	0.11	0.07	0.12	0.08
277490C7	0.08	0.02	0.00	0.01	0.09	0.07	0.15	0.13	0.03	0.01	0.11	0.08
278419C7	0.08	0.04	0.00	0.13	0.13	0.14	0.08	0.13	...	0.08	0.15	...
282804C7	0.08	0.01	0.08	0.04	0.17	0.17	0.08	0.15	...	0.01	0.16	0.08
286252C7	...	0.03	0.08	0.08	0.15	0.11	0.06	0.12	0.02	0.13	0.16	0.08
45512C2	0.08	0.11	0.08	0.00	0.15	0.09	0.08	0.14	0.09	0.01	0.12	0.08
47188C2	0.08	0.14	0.08	0.08	0.11	0.08	0.19	0.15	...	0.08	0.12	...
77186C3	0.08	0.13	0.04	0.04	0.18	0.10	0.09	0.13	0.08	0.12	0.15	0.08

TABLE 5 — *Continued*

ID	$\sigma_{\text{O}}$	$\sigma_{\text{Na}}$	$\sigma_{\text{Mg}}$	$\sigma_{\text{Al}}$	$\sigma_{\text{Si}}$	$\sigma_{\text{Ca}}$	$\sigma_{\text{Cr}}$	$\sigma_{\text{FeI}}$	$\sigma_{\text{FeII}}$	$\sigma_{\text{Co}}$	$\sigma_{\text{Ni}}$	$\sigma_{\text{Cu}}$
77707C3	0.08	0.02	0.00	0.05	0.12	0.05	0.15	0.14	0.07	0.08	0.15	0.08
80582C3	...	0.06	0.04	0.08	0.11	0.05	0.11	0.13	0.08	0.01	0.13	0.08
81644C3	0.08	0.00	0.00	0.07	0.17	0.04	0.17	0.14	0.08	0.04	0.14	0.08
82227C3	0.08	0.21	0.04	0.13	0.15	0.12	0.01	0.12	...	0.01	0.16	0.08
83531C3	0.08	0.01	0.02	0.08	0.10	0.15	0.18	0.14	0.08	0.04	0.13	0.08
84255C3	0.08	0.01	0.02	0.06	0.05	0.12	0.17	0.10	0.04	0.08	0.15	0.08
86757C3	...	0.08	0.05	0.00	0.09	0.10	0.11	0.13	0.08	0.06	0.11	0.08
88522C3	...	0.16	0.04	0.11	0.12	0.17	0.08	0.13	0.08	0.01	0.13	0.08
NGC 6553												
225847C6	...	0.08	0.06	0.06	0.07	0.13	0.12	0.14	0.02	0.09	0.11	...
227379C6	0.08	0.03	0.04	0.06	0.10	0.13	0.13	0.12	0.12	0.00	0.15	...
228407C6	...	0.01	0.04	0.02	0.16	0.12	0.13	0.15	0.08	0.04	0.11	0.08
230208C6	...	0.00	0.09	0.01	0.12	0.10	0.14	0.13	0.04	0.08	0.07	0.08
239284C6	...	0.04	0.08	0.04	0.16	0.12	0.11	0.14	...	0.01	0.14	...
265795C7	...	0.08	0.08	0.06	0.18	0.03	0.16	0.16	...	0.05	0.14	0.08
268360C7	...	0.06	0.04	0.06	0.11	0.00	0.14	0.11	0.08	0.00	0.13	0.08
268493C7	...	0.08	0.07	0.09	0.16	0.04	0.18	0.16	0.13	0.06	0.10	0.08
271021C7	...	0.01	0.11	0.06	0.11	0.11	0.14	0.15	0.08	0.11	0.16	0.08
271400C7	...	0.02	0.06	0.02	0.09	0.09	0.11	0.14	0.08	0.08	0.15	0.08
77182C3	...	0.01	0.00	0.04	0.13	0.12	0.16	0.12	0.08	0.05	0.07	...
85597C3	...	0.04	0.07	0.02	0.12	0.11	0.10	0.13	...	0.14	0.15	0.08
(l,b)=(0,-12)												
1156C2	0.08	0.02	0.00	0.01	0.04	0.07	0.08	0.10	0.08	0.05	0.11	0.08
1407C3	0.08	0.02	0.07	0.03	0.10	0.14	0.22	0.12	0.11	0.08	0.11	0.08
1491C7	0.08	0.03	0.00	0.00	0.13	0.12	0.06	0.16	...	0.18	0.13	0.08
1554C7	0.08	0.04	0.07	0.00	0.13	0.05	0.09	0.14	...	0.11	0.12	0.08
166C3	0.08	0.14	0.08	0.08	0.08	0.05	0.13	0.14	0.08	0.18	0.15	0.08
1754C3	...	0.06	0.02	0.00	0.10	0.13	0.10	0.12	0.04	0.11	0.10	0.08
1814C1	0.08	0.07	0.04	0.08	0.10	0.11	0.11	0.12	0.01	0.04	0.09	0.08
1876C2	...	0.00	0.04	0.07	0.12	0.14	0.11	0.14	0.08	0.04	0.13	0.08
1917C1	...	0.08	0.11	0.11	0.15	0.14	0.16	0.13	0.08	0.11	0.15	0.08
1918C1	0.08	0.11	0.00	0.08	0.12	0.10	0.11	0.13	0.08	0.04	0.09	0.08
201583C3	...	0.14	0.08	0.08	0.13	0.16	...	0.16	0.08	...	0.09	0.08
2110C7	0.08	0.01	0.04	0.09	0.09	0.10	0.12	0.12	0.05	0.01	0.12	0.08
2178C7	0.08	0.04	0.04	0.04	0.08	0.05	0.05	0.12	0.08	0.00	0.10	0.08
2200C3	...	0.11	0.06	0.07	0.06	0.10	0.17	0.14	0.09	0.08	0.07	0.08
2220C7	0.08	0.03	0.05	0.02	0.12	0.10	0.09	0.14	...	0.07	0.13	0.08
222C3	...	0.04	0.02	0.07	0.09	0.02	0.03	0.12	0.03	0.00	0.08	0.08
2335C2	0.08	0.04	0.04	0.07	0.07	0.08	0.02	0.11	0.08	0.08	0.11	0.08
2407C2	0.08	0.05	0.07	0.06	0.08	0.06	0.14	0.11	0.12	0.08	0.08	0.08
2422C7	0.08	0.11	0.04	0.08	0.09	0.07	0.20	0.12	...	0.00	0.08	0.08
2470C3	0.08	0.04	0.00	0.06	0.05	0.08	0.16	0.12	0.12	0.00	0.08	0.08
2502C3	0.08	0.02	0.08	0.00	0.06	0.09	0.02	0.13	0.08	0.03	0.11	0.08
2532C6	0.08	0.05	0.11	0.04	0.15	0.07	0.16	0.13	0.08	0.07	0.12	0.08
2580C6	0.08	0.11	0.06	0.00	0.15	0.10	0.12	0.18	0.08	0.01	0.14	0.08
2769C3	0.08	0.11	0.04	0.07	0.07	0.07	0.11	0.13	0.08	0.08	0.13	0.08
2772C7	0.08	0.01	0.07	0.00	0.09	0.08	0.10	0.11	0.04	0.04	0.08	0.08
2812C8	0.08	0.01	0.01	0.08	0.07	0.12	0.07	0.11	0.00	0.04	0.11	0.08
2947C3	0.08	0.04	0.14	0.04	0.12	0.09	0.09	0.13	0.08	0.11	0.08	0.08
2948C7	0.08	0.00	0.07	0.04	0.09	0.06	0.21	0.13	...	0.05	0.18	0.08
3018C3	0.08	0.04	0.00	0.01	0.08	0.05	0.10	0.11	0.06	0.08	0.09	0.08
3035C7	0.08	0.04	0.04	0.00	0.11	0.07	0.12	0.13	0.14	0.07	0.08	0.08
3091C8	0.08	0.01	0.02	0.04	0.10	0.08	0.04	0.12	0.06	0.08	0.07	0.08
3101C7	0.08	0.05	0.04	0.02	0.10	0.05	0.08	0.13	0.03	0.06	0.09	0.08
3142C3	0.08	0.09	0.07	0.05	0.07	0.05	0.06	0.13	0.11	0.01	0.10	0.08
3161C3	...	0.02	0.00	0.05	0.11	0.07	0.12	0.12	0.12	0.04	0.10	0.08
3191C7	0.08	0.05	0.01	0.00	0.10	0.05	0.07	0.11	0.01	0.00	0.08	0.08

TABLE 5 — *Continued*

ID	$\sigma_{\text{O}}$	$\sigma_{\text{Na}}$	$\sigma_{\text{Mg}}$	$\sigma_{\text{Al}}$	$\sigma_{\text{Si}}$	$\sigma_{\text{Ca}}$	$\sigma_{\text{Cr}}$	$\sigma_{\text{FeI}}$	$\sigma_{\text{FeII}}$	$\sigma_{\text{Co}}$	$\sigma_{\text{Ni}}$	$\sigma_{\text{Cu}}$
3201C6	0.08	0.04	0.00	0.09	0.10	0.07	0.12	0.13	0.18	0.11	0.12	0.08
3238C6	...	0.04	0.04	0.09	0.13	0.04	0.10	0.12	0.00	0.01	0.10	0.08
3267C3	0.08	0.06	0.04	0.01	0.06	0.10	0.11	0.09	0.05	0.01	0.08	0.08
3515C3	...	0.03	0.00	0.05	0.12	0.09	0.09	0.12	0.08	0.01	0.09	0.08
3558C6	...	0.01	0.11	0.03	0.06	0.09	0.15	0.13	0.08	0.07	0.10	0.08
3690C7	0.08	0.08	0.00	0.08	0.11	0.09	...	0.12	0.06	0.08	0.13	0.08
3711C7	0.08	0.04	0.08	0.07	0.08	0.06	0.20	0.13	0.11	0.14	0.13	0.08
3733C3	0.08	0.01	0.02	0.01	0.10	0.08	0.13	0.11	0.05	0.01	0.10	0.08
3796C6	0.08	0.01	0.05	0.02	0.12	0.04	0.11	0.12	0.06	0.04	0.09	0.08
3965C6	0.08	0.03	0.00	0.00	0.03	0.12	0.09	0.12	0.08	0.01	0.11	0.08
4085C3	0.08	0.02	0.07	0.00	0.08	0.09	0.08	0.10	0.04	0.07	0.10	0.08
4217C6	0.08	0.01	0.08	0.08	0.12	0.08	0.02	0.15	0.02	0.04	0.14	0.08
4263C6	0.08	0.06	0.08	0.04	0.12	0.07	0.18	0.14	0.11	0.08	0.11	0.08
431C2	0.08	0.03	0.00	0.07	0.10	0.11	0.12	0.12	0.03	0.00	0.10	0.08
4365C3	...	0.20	0.08	0.07	0.12	0.17	0.19	0.14	0.17	0.08	0.16	0.08
4478C8	0.08	0.05	0.01	0.00	0.10	0.08	0.04	0.10	0.09	0.02	0.10	0.08
455C1	0.08	0.05	0.00	0.08	0.09	0.12	0.08	0.11	0.08	0.08	0.11	0.08
4612C6	0.08	0.08	0.06	0.08	0.14	0.11	0.12	0.13	0.08	0.05	0.06	0.08
4740C8	0.08	0.00	0.01	0.02	0.15	0.08	0.13	0.11	0.08	0.10	0.10	0.08
4876C6	0.08	0.08	0.00	0.00	0.08	0.09	0.06	0.11	0.05	0.08	0.13	0.08
5319C6	0.08	0.14	0.04	0.01	0.05	0.07	0.18	0.12	0.10	0.08	0.10	0.08
5351C8	0.08	0.06	0.04	0.05	0.07	0.07	0.14	0.11	0.06	0.04	0.10	0.08
5400C8	...	0.06	0.04	0.02	0.07	0.07	0.08	0.12	0.08	0.04	0.09	0.08
5487C8	...	0.01	0.04	0.02	0.11	0.06	0.16	0.14	0.15	0.08	0.10	0.08
5543C6	0.08	0.06	0.07	0.00	0.16	0.10	0.07	0.13	0.08	0.12	0.17	0.08
5588C6	0.08	0.09	0.04	0.00	0.04	0.05	0.11	0.11	0.06	0.03	0.10	0.08
5664C6	0.08	0.00	0.08	0.00	0.20	0.14	0.17	0.13	...	0.01	0.11	0.08
5908C6	0.08	0.12	0.00	0.07	0.07	0.11	0.12	0.11	0.10	0.08	0.08	0.08
5977C6	0.08	0.00	0.04	0.04	0.12	0.10	0.15	0.12	0.01	0.05	0.11	0.08
5980C6	...	0.09	0.04	0.06	0.08	0.04	0.06	0.11	0.08	0.04	0.12	0.08
608C1	0.08	0.08	...	...	0.16	0.15	0.13	0.14	0.06	...	0.12	0.08
6090C6	0.08	0.11	0.14	0.00	0.15	0.14	0.19	0.12	...	0.08	0.12	0.08
6164C6	0.08	0.01	0.00	0.08	0.11	0.10	0.12	0.11	0.11	0.05	0.09	0.08
6230C5	...	0.04	0.00	0.01	0.05	0.06	0.09	0.12	0.05	0.03	0.10	0.08
6263C6	...	0.11	0.07	0.02	0.08	0.19	0.16	0.14	...	0.11	0.16	0.08
6391C8	0.08	0.13	0.07	0.04	0.08	0.09	0.11	0.12	0.08	0.11	0.06	0.08
6419C5	0.08	0.12	0.00	0.02	0.07	0.05	0.09	0.13	0.18	0.01	0.14	0.08
6426C8	...	0.00	0.00	0.02	0.15	0.12	0.07	0.12	0.02	0.08	0.09	0.08
6505C6	0.08	0.04	0.00	0.05	0.05	0.07	0.08	0.11	0.14	0.04	0.07	0.08
650C2	0.08	0.00	0.04	0.08	0.07	0.06	0.06	0.08	0.06	0.02	0.07	0.08
6549C6	0.08	0.09	0.04	0.07	0.11	0.02	0.17	0.13	0.06	0.06	0.10	0.08
6637C8	0.08	0.01	0.00	0.08	0.11	0.04	0.12	0.11	0.08	0.00	0.12	0.08
6717C6	0.08	0.01	0.01	0.00	0.07	0.09	0.10	0.11	0.08	0.07	0.09	0.08
6828C7	0.08	0.01	0.00	0.05	0.11	0.10	0.15	0.10	0.04	0.04	0.11	0.08
6913C7	0.08	0.00	0.04	0.07	0.09	0.05	0.08	0.11	0.08	0.04	0.07	0.08
867C3	0.08	0.02	0.00	0.08	0.11	0.08	0.10	0.08	0.06	0.08	0.08	0.08

NOTE. — For cases where only one line was measured we have assigned a default value of 0.08. This is the average dispersion value for all species in which more than one line was measured.